

Orientational Texture of Lipid Bilayer and Monolayer Domains

PhD Thesis

Jes Dreier

Supervised by

Associate Professor Adam Cohen Simonsen



MEMPHYS

MEMPHYS – center for biomembrane physics
Department of Physics, Chemistry
and Pharmacy
University of Southern Denmark
November 2012



UNIVERSITY OF SOUTHERN DENMARK

Preface

This thesis covers the scientific work I have conducted during the last three year during my PhD education in biophysic at MEMPHYS – center for biomembrane physics, Institute of Physics, Chemistry and Pharmacy, University of Southern Denmark.

This work has been done under the qualified supervision of Associated Professor Adam Cohen Simonsen, and I am thankful for his help and advice during the last three years.

Research Assistant Professor Jonathan R. Brewer should be acknowledged for the valuable help regarding the 2-photon microscope, its use, and interpretation of the results.

I am very grateful to have had the opportunity to spend 6 month at University California Davis during my PhD. I owe many thanks to Professor Tonya Kuhl and Professor Margie Longo and their respectively research groups, for the help during my time there.

I would like to acknowledge all the people at MEMPHYS for the help, support, and for making MEMPHYS what it is. A special thanks goes to the Ph.D. students Morten Christensen, Thomas E. Rasmussen and Mathias P. Clausen, both the help with this thesis, but also for countless discussions, (and much need coffee breaks) during my time at MEMPHYS. Your help have been invaluable.

Most importantly a special thanks to my wife Signe, especially for the incredible support during the writing process of this thesis.

The work in this thesis has lead to the following papers and manuscripts:

- J. Dreier, J. Brewer, and A.C. Simonsen, *Texture Defects in Lipid Membrane Domains*, **Soft Matter**, 2012, 8, 4894
- J. Dreier, and A.C. Simonsen, *Variations in the Hydrophobic Mismatch affects the Orientational Texture in Phospholipid Bilayers*, (To be submitted)

Front Page: Artistic image of the texture of several L_{β} -domains in DOPC, DPPC bilayer. Finalist in the second Annual Biophysical Society Art of Science Image Contest, at the Biophysical Society 56th Annual Meeting 2012, San Diego, USA,

Abstract

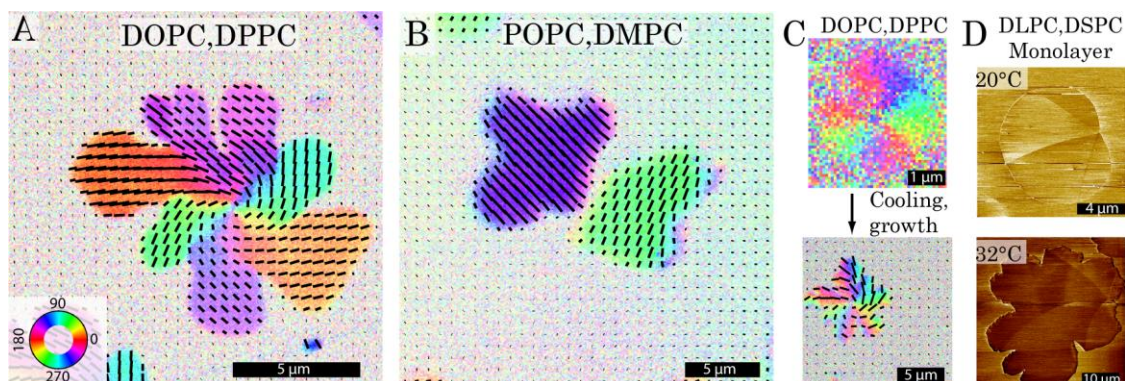
Lateral organization of the cellular plasma membrane is of great importance in many cell processes, and is an exciting field to study. However, the cellular plasma membrane is a very complex structure and consists of several thousands of unique components. By using supported lipid bilayers we are able to study phase separation, which is coupled to lateral organization, in a compositionally simpler model system that allow minute control of the variables.

We study $L_{\beta'}$ domains of phosphocholine lipids, which recently have been proven by polarized fluorescence microscopy and x-ray scattering to contain an internal orientational order of the lipid acyl chains. We measure this internal orientation order by polarized 2-photon fluorescence microscopy. The orientational texture, i.e. the description of the orientation and variation thereof across the entire domain, were found to be very complex.

Lipid membranes of DOPC,DPPC formed $L_{\beta'}$ domains that were divided into subdomains, each with a unique preferred orientation, Fig. (A). In the central region of the domains a vortex-like texture with a continuously change of orientation was observed, converging into two point defects ($m = 1/2$) in the center .

By changing the lipid acyl chains, we were able to investigate the effect of the hydrophobic mismatch, i.e. the height difference between the $L_{\beta'}$ and L_{α} phases, on the orientational texture. For low hydrophobic mismatch ($<1\text{nm}$, POPC,DMPC) the complex orientational texture disappeared. Instead a uniform orientation was observed, see Fig. (B). Furthermore, it was found that the orientational texture was already present in small domains, close to the nucleation temperature. This texture was conserved during the further growth of the domain, meaning that the structures of the small domains are present in the larger domains at a lower temperature, see Fig. (C).

AFM and polarized fluorescence microscopy were used to measure the orientational texture of LC-domains in monolayers of DLPC,DSPC. We proved that the change of temperature could affect the domain shape and orientational texture, Fig. (D). This was related to the non-isothermal growth of domains in the bilayer.



Sammenfatning

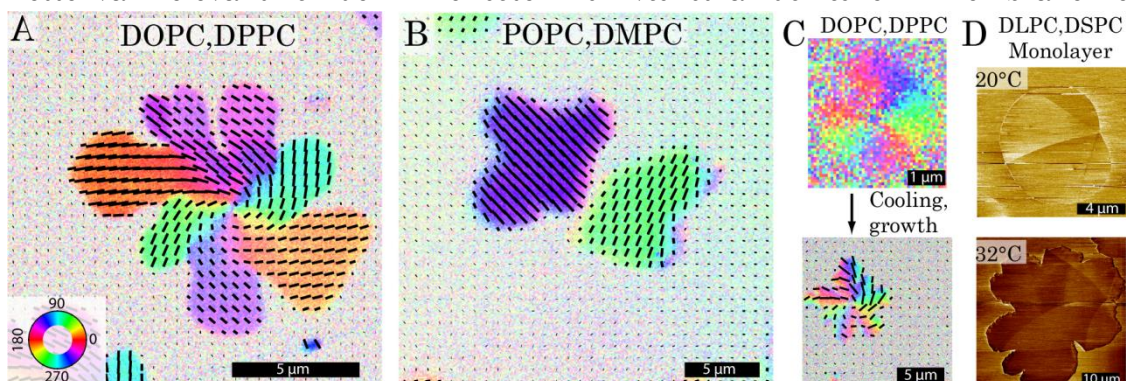
Den laterale organisation af den cellulære plasmamembran har stor betydning for mange af cellens processer. Dette gør den til et meget spændende forskningsområde. Den cellulære plasmamembran er dog yderst kompleks og består af flere tusinde forskellige komponenter. Vi bruger understøttede lipidmembraner, som er et simpelt model system for den cellulære plasmamembran til at undersøge fase separation, der er tæt koblet til den laterale organisering.

Vi studerer $L_{\beta'}$ domæner af fosfocholinlipider, som har vist sig at have en indre orienteringsorden af de lipide fedthaler. Dette er blevet vist med polariseret fluorescens mikroskopi og røntgen spredning. Vi måler denne indre orienteringsorden med polariseret 2-foton fluorescensmikroskopi. Den målte orienterings texturen, dvs. beskrivelsen af orienteringerne og hvordan de varierer i hele domænet, viste sig at være meget kompleks.

Lipidmembraner af DOPC, DPPC dannede $L_{\beta'}$ domæner, der var inddelt i subdomæner, hver med en unik foretrukket orientering, Fig. (A). I den centrale region af domænerne var der en kontinuerlig ændring af orienteringen. Den konvergerer ind til to punktdefekter ($m = 1/2$) i midten.

Ved at ændre fedthalerne på lipiderne var vi i stand til at undersøge effekten af højdeforskellen mellem $L_{\beta'}$ og L_{α} faserne på orienteringsteksturen. For en lille højde forskel ($<1\text{nm}$, POPC, DMPC) forsvandt den komplekse tekstur og blev erstattet af en uniform tekstur, Fig. (B). Den orienteringsmæssige tekstur var allerede til stede i små områder, tæt på nukleringstemperaturen. Under den videre dannelse af domænerne blev denne tekstur ikke ændret. Dette betyder, at tekturen af de små domæner er til stede i de større områder ved en lavere temperatur, se Fig. (C).

AFM og polariseret fluorescensmikroskopi blev anvendt til at måle den orienteringsmæssige tekstur af LC-domæner i monolag af DLPC, DSPC. Ændringen af temperaturen påvirkede domænernes form og orienteringstekstur, Fig. (D). Dette var relevant for den ikke-isotermisk vækst af domæner i membraner.



Abbreviations

2D = Two dimensions
3D = Three dimensions
 Π = Surface tension
AFM = atomic force microscopy
BAM = Brewster angle microscopy
DLA = Diffusion limited aggregation
DLPC = 1,2-dilauroyl-sn-glycero-3-phosphocholine
DMPC = 1,2-dimyristoyl-sn-glycero-3-phosphocholine
DOPC = 1,2-dioleoyl-sn-glycero-3-phosphocholine
DPPC = 1,2-dipalmitoyl-sn-glycero-3-phosphocholine
DSPC = 1,2-distearoyl-sn-glycero-3-phosphocholine
G = Gaseous (monolayers phase)
GIXD = grazing incidence x-ray diffraction
GUI = Guide user interface
GUV = giant unilamilar vesicles
HWP = Half wave plate
 L_{α} = Liquid crystalline/fluid/liquid disordered/ L_D (bilayer phase)
 L_{β} = gel/solid ordered/ S_0 (bilayer phase)
LBS = Langmuir Blodgett-Schaeffer
LE = Liquid expanded (monolayer phase)
LC = Liquid condensed (monolayer phase)
NA = numerical aperture
PALM = photo-activated light microscopy
PMT = photo multiplier tubes
PC = phosphatidylcholine
POPC = 1-palmitoyl-2-oleoyl-sn-glycero-3-phosphocholine
QWP = quarter wave plate
S = Solid (monolayer phase)
SM-C₁₈ = N-stearoyl-D-*erythro*-sphingosylphosphorylcholine
Sm-C = smectic- C (liquid crystal phase)
SPM = scanning probe microscopy
SPT = single particle tracking
STED = stimulated emission depletion
STORM = stochastic optical reconstructed microscopy
SUV = small unilamilar vesicles
 T_m = Transition temperature

Table of Content

Preface	I
Abstract	II
Sammenfatning	III
Abbreviations	IV
Table of Content	V
Chapter 1: Introduction	1
1.1 Lipids.....	1
1.2 Lateral Organization in the Cellular Membrane.....	4
1.3 Model System of a Plasma Membrane.....	6
1.4 Motivation.....	8
Chapter 2: Structural Order in 2 Dimensions	9
2.1 Phases and Phase Separation in Monolayers.....	10
2.2 Liquid Crystals.....	13
2.3 The Hexatic Phases in Monolayers.....	14
2.4 Phases and Phase Separation in Bilayers.....	23
Chapter 3: Fabrication and characterization	27
3.1 Fluorescence Microscopy.....	27
3.2 Laurdan.....	29
3.3 Atomic Force Microscopy.....	32
3.4 Brewster Angle Microscopy.....	34
3.5 Fabrication of supported lipid bilayers.....	35
3.6 Procedures, Equipment and Materials.....	37
Chapter 4: Orientational Texture and Defects in DOPC DPPC Bilayers	40
4.1 Experimental Setup.....	41
4.2 Measuring the Orientation.....	42
4.3 Internal Distribution of Orientations.....	46
4.4 Defect Structures.....	47
4.5 Central Point Defect.....	50
4.6 Effect of Substrate.....	53
4.7 Discussion.....	55

4.8	Conclusion	59
	Chapter 5: Influence of Lipid Composition on Texture in Lipid Bilayers	60
5.1	Experimental Preparations	61
5.2	Orientalional Texture.....	63
5.3	Distribution of Orientations within the Domains.....	64
5.4	Central Vortex Texture	67
5.5	Measuring the Hydrophobic Mismatch	68
5.6	Orientation at the Phase Boundary.....	69
5.7	Texture of Early Domain Growth	71
5.8	Domain Nucleation	73
5.9	The Intrinsic Tilt of the Lipids.....	74
5.10	Discussion	76
5.11	Conclusion.....	82
	Chapter 6: Orientalional Texture in Monolayers	83
6.1	Experimental Idea and Motivation.....	84
6.2	Brewster Angle Microscopy	86
6.3	Transfer of Monolayers to an Air-Solid Interface.	89
6.4	AFM Friction Reveals Orientalional Texture in Monolayers.....	92
6.5	Polarized 2-photon Fluorescence on Monolayers	96
6.6	Discussion.....	101
6.7	Conclusion	104
	Chapter 7: Conclusion	105
	Bibliography	107
	Appendix 1: Soft Matter, article	A1
	Appendix 2: Manuscript	A2

Chapter 1

Introduction

A requirement for life is the ability to form closed compartments and thereby discriminate an interior from an exterior. Furthermore, this confining barrier needs to be permeable, in order to control the uptake of food, and disposal of waste products. These tasks are carried out by the plasma cellular membrane and its associated membrane protein which forms an effective barrier towards the surrounding and allow transport, both passive and active, across it. In case of eukaryotic cells other membrane also compartmentalizes the interior organelles for example the mitochondria, nucleus, Golgi apparatus etc. Previously the plasma membrane was thought to be a passive 2 dimensional solvent in which the membrane proteins were imbedded. All the tasks associated with the membrane, e.g. transport, recognition, were credited to the membrane bound proteins. Today it is clear that the cellular membrane plays a more active role in these processes.[1] An understanding of the roles of the cellular plasma membrane is crucial in respect to understand the cell, its function, and interplay with the surroundings, or in another word: Life.

The cellular membrane is an amazing object to study for a biophysicist. It have been around for millions of years, and through that time it have been refined by evolution to meet the requirements of the cell.[1] For instance the cellular membrane is extremely thin compared to the cell it surrounds. It is only about 5-6 nm thick corresponding to exactly two molecules thick, this makes it an extraordinary efficient container. This is just one example of how specialized it is and a study of its physical properties are bound to be insightful. The building blocks for the cellular membrane are lipids, which will be the topic of the following section.

1.1 Lipids

The cellular membrane consists of two major components namely lipids and membrane proteins. This section will focus on giving an introduction into the lipids of the cellular membrane, and explain the interplay between lipids and membrane bound proteins.

A lipid molecule can be divided into two regions a hydrophilic head and a hydrophobic tail region. This amphipathic nature of lipids leads to a self assembling in water, where the lipids will aggregate in order to shield the hydrophobic tails from the water. Depending on the geometry of the lipid, i.e. the

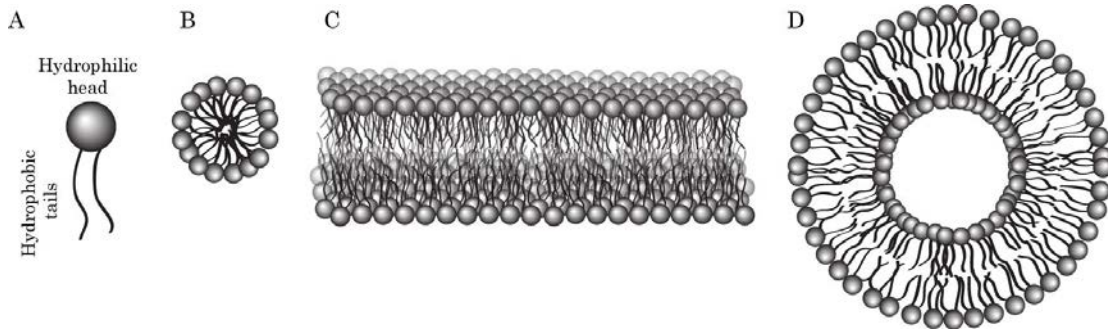


Figure 1.1 Lipids can be divided into a hydrophilic head and one or more hydrophobic tail (A), in the presence of water, they will self assemble into larger structures like micelles (B), lamellar bilayers (C), vesicles (D).

size of the head and the tail, they will self assemble into different structures, e.g. micelles, lamellar bilayers, liposome, which are illustrated in Figure 1.1.

One of the most important types of lipids is glycerophospholipids. Their chemical structure consists of a glycerol backbone onto which two fatty acids are bound by ester bonds, those fatty acids are the hydrophobic tails. Furthermore, an alcohol is also bound to the glycerol through a phosphate bond, which constitutes the hydrophilic head. Examples of alcohol used in the head regions are ethanolamine, choline, and serine. The diversity among the fatty acids is large, and is caused by different chain lengths and degrees of unsaturation (double bonds). Examples of the different head groups and fatty acids are shown in Figure 1.2. When referring to glycerophospholipids it is common to use a 4 lettered abbreviation. The first two letters refer to the fatty acids, e.g. di-palmitoyl is DP, palmitoyl-oleoyl is PO, and the last two letters refer to the headgroup, e.g. phosphocholine is PC, phospho-ethanolamine is PE. Thus 1,2-dipalmitoyl-sn-glycero-3-phosphoethanolamine would be DPPE, and can be seen in Figure 1.2A.

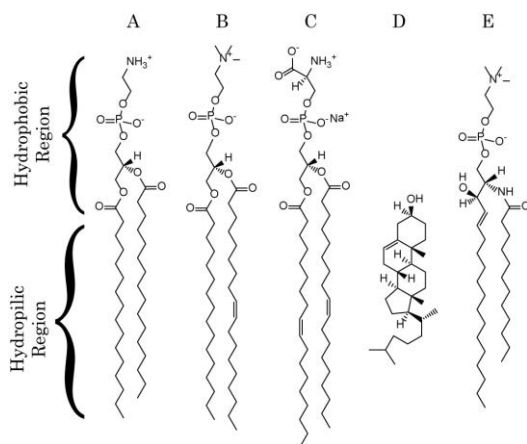


Figure 1.2 Examples of different lipids. A-C are glycerophospholipids with different head group and chain length. A) 1,2-dipalmitoyl-sn-glycero-3-phosphoethanolamine (DPPE). B) 1-palmitoyl-2-oleoyl-sn-glycero-3-phosphocholine (POPC). C) 1,2-dioleoyl-sn-glycero-3-phospho-L-serine (DOPS). D) Cholesterol. E) Sphingomyelin.

Another important group of lipids are sterols. The mammalian sterol is cholesterol, and its molecular structure is shown in Figure 1.2D. As any sterol it has a small head group and a very rigid and broad hydrophobic tail region. The impact of cholesterol on the dynamics of the entire cellular membrane is enormous. A simple system of one glycerophospholipid, without sterols, can basically be in one of two different phases dependent whether the temperature is below or above the melting temperature (T_m) of the given lipid.

1. Below T_m : The lipid will form a solid-ordered phase, where the headgroups and tail are ordered and any movement is slow.
2. Above T_m : The lipid will form a liquid-disordered phase where no order is present in the head group or tails, and movement of both head and tail is fast.

Cholesterol can participate in both of those phases, and induce disorder in the solid-ordered phase and order in the liquid-disordered phase. Furthermore, in more complex systems it will lead to a unique new phase called the liquid-ordered phase, first described by Ipsen et al.[2]. Cholesterol induces order in the tail region by stretching them, while keeping disorder of the head group and thereby maintains a high lateral mobility.[1] Sterols have had a significant impact in the evolutionary path of the eukaryote cells, and is one of the key divergences between prokaryotes and eukaryotes.[1]

Sterols and glycerophospholipids account for about 85-90% of the total lipids in the cellular membrane, with sphingolipids accounts for majority of the remains. An example of a sphingolipid, namely sphingomyeline, is shown in Figure 1.2. The lipids can thus effectively be classified into those three groups: Glycerophospholipids, sterols, and sphingolipids. The cellular plasma membrane consists of a myriad of different unique lipids each with an individual headgroup coupled to a specific set of fatty acid tails.[3]

The cellular plasma membrane is not just lipids, in fact a large part consists of proteins, as much as 50% by weight and 20% by area in case of mammalian cells.[1] The membrane associated proteins can be classified by their interface with the membrane, most interesting are the trans membrane protein that traverse the entire plasma membrane, but other types includes partially imbedded proteins, and lipid anchored proteins. The transmembrane proteins need to be adapted to fit the hydrophilic and hydrophobic characters of the different levels of the plasma membrane; they need a hydrophobic part that spans the membrane, and two hydrophilic parts that are exposed to each side of the membrane. The length of the hydrophobic region is however not identical for different transmembrane proteins, which means the plasma membrane have to adopt its thickness to accommodate the transmembrane protein. This implies that transmembrane proteins with a hydrophobic region thicker than the plasma membrane will locally increase the thickness of the membrane. This can be done either a ordering of the lipid tails, or a local increased concentration of lipids with a long fatty acid tail; of course the opposite is the case for transmembrane proteins with a thinner

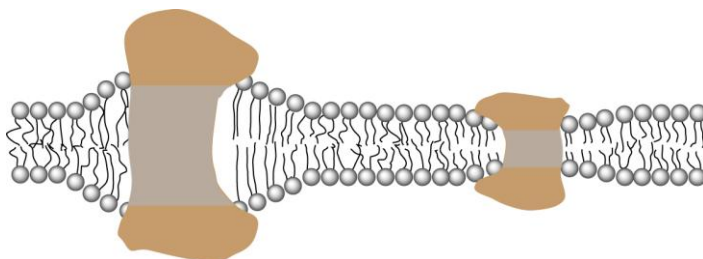


Figure 1.3 Schematization of hydrophobic matching, in which the membrane will either swell or compress in order to fit the hydrophobic region of the protein (gray part).

hydrophobic region.[4, 5] This hydrophobic matching is schematized in Figure 1.3.

From just this simple phenomenon it is obvious that the lipids in cellular plasma membranes are not just a passive 2 dimensional solvent in which the membrane proteins are dissolved, as were first suggested by Singer and Nicolson in 1972.[6] They came up with a membrane model called the “fluid-mosaic” model, that should explain the behavior and role of the plasma membrane, as understood by their time. For several reasons this model is imprecise in describing current knowledge about the plasma membrane, e.g. neither the lipid diversity nor the observation about the hydrophobic matching as seen in Figure 1.3 can be explain by the fluid-mosaic model. The fluid-mosaic model have been continuously update, for instance by Jacob Israelachvili in 1977 who refined the model to include the hydrophobic matching.[7] And up to current time it is still highly debated what the best membrane model is, and what it should include.

1.2 Lateral Organization in the Cellular Membrane

The cellular plasma membrane is not a uniform fluid with a random distribution of the individual lipids and membrane imbedded proteins, as was proposed by Singer and Nicolsen.[6] In fact several physical (and biological) mechanisms lead to lateral organization of the cellular membrane. Three of particular interest will be mentioned here.

The hydrophobic matching described previously, and illustrated in Figure 1.3, will make it attractive for transmembrane proteins of same hydrophobic length to cluster together, as is illustrated by Mouritsen and Bloom in the *Mattress* model.[4]

1. Spatial segregation in the plasma membrane will result in a sorting of the different lipid compounds, depending on their phase preference, which will also affect the proteins in the membrane. This is partially the foundation of the raft hypothesis, initially suggested by Simons and Ikonen in 1997.[8]
2. Membrane associated proteins that are anchored to the cytoskeleton can act to compartmentalize the plasma membrane and thereby act as fences or corrals, which was promoted by Kusumi in 2005.[9]

Those three principles are illustrated in Figure 1.4. All of those three mechanisms have been derived from experimental observations and theoretical consideration. Of particular interest for the work in this thesis is the second mechanism which involves phase separation in the membrane.

The initial raft hypothesis was based on detergent resistant membrane fraction. These were collected after a non-ionic disruption of cells at 4°C followed by a separation by sucrose gradient centrifugation. This left insoluble lipid-protein complex that was enriched in certain lipids and protein, these were named raft molecules. Those lipids and protein where thought to form domains *in vivo*. This caused the raft hypothesis to be heavily criticized, since detergent and cooling

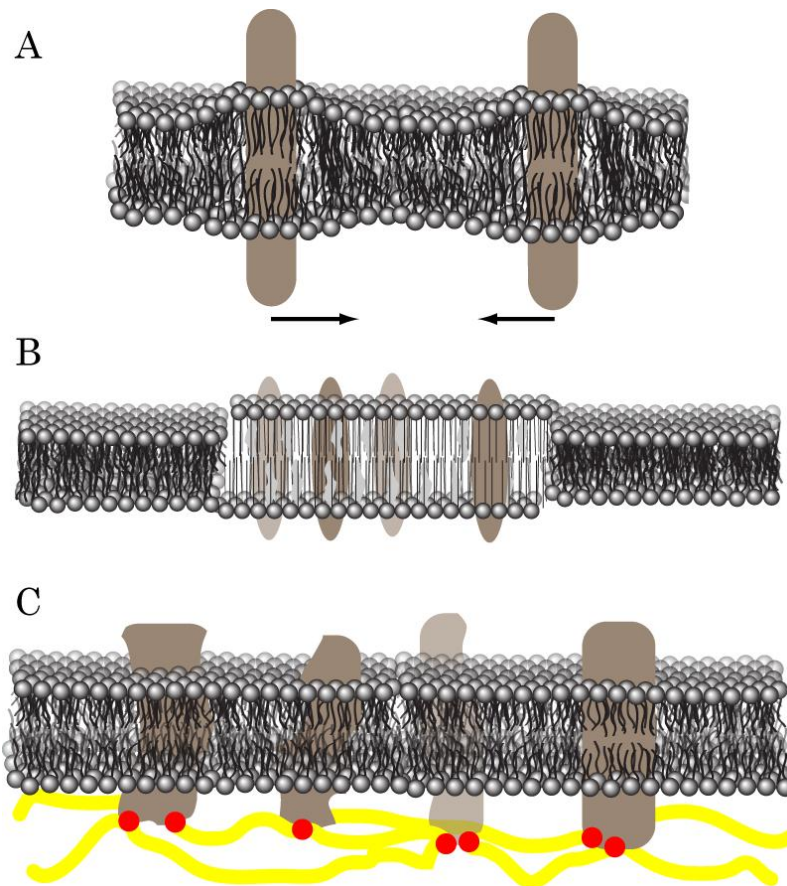


Figure 1.4 Three ways inhomogeneity is thought to be induced in a cellular plasma membrane. A) The hydrophobic matching pulls proteins of similar hydrophobic region together. B) Rafts in liquid ordered phase leads to concentration of certain membrane proteins. C) Transmembrane proteins bound to the cytoskeleton build a fence that compartmentalizes the membrane.

induce changes in the membrane, and therefore those insoluble complexes might not be present *in vivo*. Rightfully this detergent definition have been abandoned.[10] Lipid rafts were suggested to be the liquid-ordered phase, as seen in model system enriched in cholesterol and sphingomyelin.[11] However studies on model membrane made from extract from cellular plasma membrane, in the form of giant unilamellar vesicles (GUV), showed phase separation upon cooling to 12°C. This phase was found to differ from the liquid-ordered phase, and was denoted raft-phase.[12] It is quite amazing that a mixture of, at least, several 100 different compounds are able to segregate into coexisting phases that are visible using a fluorescence.

One of the problems about the idea of rafts in the cellular plasma membrane is the lack of direct visual evidence in the form of microscopy image. Which have lead to the conclusion that raft domains are smaller than the resolution limit of conventional microscopy. The actual size and life time depends heavily on the technique applied to measure them with. But in general they are thought to be small (<200 nm) and short lived.[11] The search for lateral organization has expanded into the era of super resolution and advance new techniques, e.g.

stimulated emission depletion (STED), photo-activated light microscopy (PALM), stochastic optical reconstructed microscopy STORM, and single particle tracking (SPT). Whether those techniques will prove the existence of rafts, or simply push the size and time scale further remains an open question.

Although the concept of rafts is still highly debated, some form of lateral organization in the cellular plasma membrane is recognized as a requirement for its function. In order to understand this organization knowledge about the thermodynamics of the plasma membrane is needed. However the cellular plasma membrane is a very complex structure. Not only does it consist of numerous different lipids and proteins, but their intermolecular interactions are also not completely understood. There are several approaches towards solving these questions. Our approach is the use of model systems that mimic the cellular plasma membrane, which will be the topic of the next section.

1.3 Model System of a Plasma Membrane

A model system is a setup that allows one to study a particular phenomenon, in a system where it is isolated from other factors. Model membranes are a very popular model system in respect of the cellular plasma membrane[13] and for good reason. As we described above the cellular plasma membrane is a very complex size that makes direct visualization of mechanisms troublesome. Model membranes allow a minute control of the system and with the diversity of different techniques available to fabricate and characterize them, their widespread use is no surprise.

There are two different approaches towards working with model membranes namely supported lipid bilayers and free standing lipid bilayers, both of which are illustrated in Figure 1.5. As the name implies supported lipid bilayers utilize a solid support underneath the lipid bilayer, e.g. mica, silicon wafers, glass. This gives the advantage of a planar bilayer that is easy to visualize by fluorescence microscopy. Furthermore the solid support allows the use of scanning probe microscopy (SPM), since the membrane is somewhat resistant to the force induced by the probe. However this does not come without certain disadvantages, firstly it is important to consider the forces between the substrate and the membrane. Those forces can be minimized by using the right substrate and aqueous buffer which can shield the membrane from the substrate.[14] In some

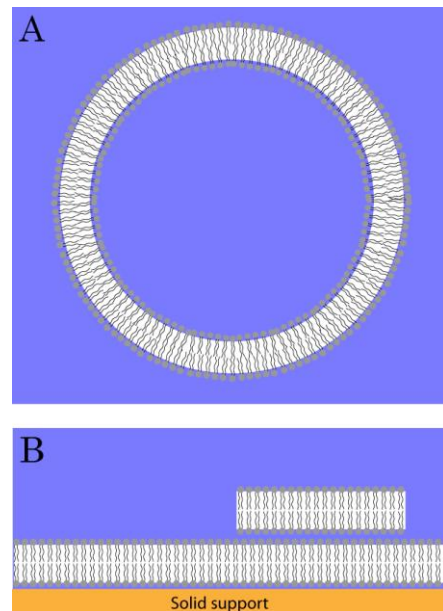


Figure 1.5 Two different ways of using lipid bilayers as models for the cellular plasma membrane. A) Vesicles, often in the form of GUV and B) supported lipid bilayers, the 1st layer has stronger interactions with the substrate than the 2nd layer.

cases the second level of bilayer can be used for the investigation, since it is more decoupled from the substrate than the first level, this can also be seen in Figure 1.5. Research has also been carried out to investigate the use of a soft cushion between the solid substrate and the model membrane. The use of GUV offers a different model system for biological membranes. The advantage and disadvantage are complementary compared to the solid supported membranes. The planar area ideal for microscopy and the ability to use SPM are lost, but there are no problem regarding interaction between the substrate and the membrane. They are still very popular as model system for e.g. fluorescence microscopy, despite the absence of the planar surface.[15] It offers some problem regarding the shape, distortion etc. but they are manageable. The use of a spherical sample also enables the possibility to study curvature in the membrane.

A great advantage of working with model membranes is the ability to control the content, and thereby the complexity, of the membrane. Applications of model membranes span the entire spectra from simple mono component system of ordinary glycerophospholipids, to complex cell extract that includes protein. This diversity allows one to design the model membrane to the specific study. When designing the model system it is important to consider the limitations, and most lipid model membranes, in contrast to the cellular membrane, are isolated systems that are allowed to equilibrate during the experiments. In the cellular membrane there is a constant flux of both lipids and proteins, and it is in all respects a dynamic system. Does this mean a static isolated model membrane cannot tell you anything about the cellular plasma membrane? No, but that does not mean results are directly transferable to a cellular plasma membrane either. In general when working with a model system any results need to be interpreted in respect to that model, and subsequently a comparison between the results from the model system and the 'real' system can be made. The model membranes are no different.

1.4 Motivation

Lipid membranes give rise to complex and interesting phase behavior, but the importance of these for life is far from being understood. For instance the recent discovery of a complex internal orientational order in domains of gel/ $L_{\beta'}$ phase in supported lipid bilayers of DOPC and DPPC made by Bernchou et al.[16] introduced a previously unaccounted dimension to the $L_{\beta'}$ phase.

Much of the work regarding phases in lipid membrane has been focused on either the liquid-ordered phase or different parameters regarding rafts, and the $L_{\beta'}$ phase is normally not a phase associated with life, instead. The $L_{\beta'}$ phase is however also relevant for life, since it is present in skin[17, 18] and in cells undergoing apoptosis.[19] Furthermore, the study of domains in the $L_{\beta'}$ phase can be used to investigate important parameters regarding phase separation.

We used supported lipid bilayers made from a binary mixture of glycerophospholipids. The two components were chosen so they had different T_m and therefore can segregate into two co-existence phases, namely the fluid L_{α} and the $L_{\beta'}$. This allow precise and detailed studies of phase separation, phase co-existence, and formation of domains.

We wanted to make a systematic investigation of the orientational texture of domains in the $L_{\beta'}$ phase. The orientational texture is a description of the orientations and the variation thereof across the entire domain.

Chapter 2

Structural Order in 2 Dimensions

In this chapter an introduction into structural order in two dimensions (2D) will be given. This should not be thought of as a complete and comprehensive review regard phase behavior in 2D, instead the aim is to give an introduction about certain structural ordering, which are relevant for understanding the results in the following chapters.

The phases and phase separation in monolayers will be the starting point, in which the basic behavior of a surfactant on an air-water interface will be described, followed by a brief introduction into the field of liquid crystals. This will lead to a thorough theoretical description of the orientational texture exhibited by surfactant monolayers in a hexatic phase, carried out with inspiration from Fischer et al. article about the subject.[20] Which was an expansion on existing theory about hexatic phases in liquid crystal systems of symmetric molecules, which surfactants are not. The orientational texture is a description of the variations of the orientation inside a domain.

Lastly phases and phase separation for lipid bilayers will be dealt with. This is of great importance for the experimental results in this thesis, since most experiments have been carried out on lipid bilayers. This will include an introduction to the different phases encountered in this thesis, as well as explanations about phase behavior of a lipid bilayer as the temperature is changed.

2.1 Phases and Phase Separation in Monolayers

The surface between two immiscible compounds is associated with an energy cost given by the surface tension, which unit is energy per area. A surfactant, i.e. a surface active agent, is able to lower this energy. This interface is a very interesting system to study, since it is effectively a 2 dimensional (2D) model system, in which the surfactant are only able to move, and order itself in 2D. For a biophysicist student the study of an air-water interface with lipids as the surfactant is of special interest since it resembles half a cell membrane.

The surface tension of a liquid (γ_0) will be reduced in the presence of a monomolecular film of surfactants covering the surface.

$$\Pi = \gamma_0 - \gamma \quad \text{Eq. 2.1}$$

Where the resulting surface tension of the film covered surface is γ . The surface pressure, Π , is therefore the resulting reduction in the surface tension compared to the pure liquid.[21] For water $\gamma_0 = 72,8 \text{ mN/m}$. When doing monolayer experiments the surface tension is one of the measurable parameter.

A typical monolayer experiment will start by the spreading of the surfactant, e.g. DPPC, which is dissolved in an appropriated solvent, e.g. chloroform, onto the water surface in a trough with moveable barrier, and a surface tensiometer. At the start of the experiment the area per molecule will be large, and thus interactions between the surfactants are small. This is called the gaseous phase (G), as seen in Figure 2.1. It bears many resemblances to the 3 dimensional (3D) phase of the same name.

After the spreading of the surfactants and the evaporation of the solvent, the area of the surface will be reduced by the moving barriers. This forces the surfactants closer together and increases their interactions. At first the surface pressure rises very slowly, until the gaseous (G) to liquid expanded (LE) phase transition, which is normally not observed in the isotherm. After this phase transition the surface pressure will increase while in the LE phase, as marked in Figure 2.1. At a certain surface pressure the liquid expanded to liquid condensed phase (LC) transition will take place, as marked in Figure 2.1. This is a first order phase transition and theoretically this will happen at constant pressure, thereby forming a horizontal line in the isotherm as seen in Figure 2.1. In the real world it might not be completely horizontal, and there can be several reasons for this, impurity could be an explanation.[21] After the phase transition the surface pressure will begin to increase again as the area is reduced, this time at a much steeper slope, due to a low compressibility of the LC phase, i.e. the molecules are already tightly packed. If the area is further reduced the surfactants will undergo a phase transition to a solid (S) phase, until a certain surface pressure where the monolayer film of surfactants will collapse. The collapse can be several different

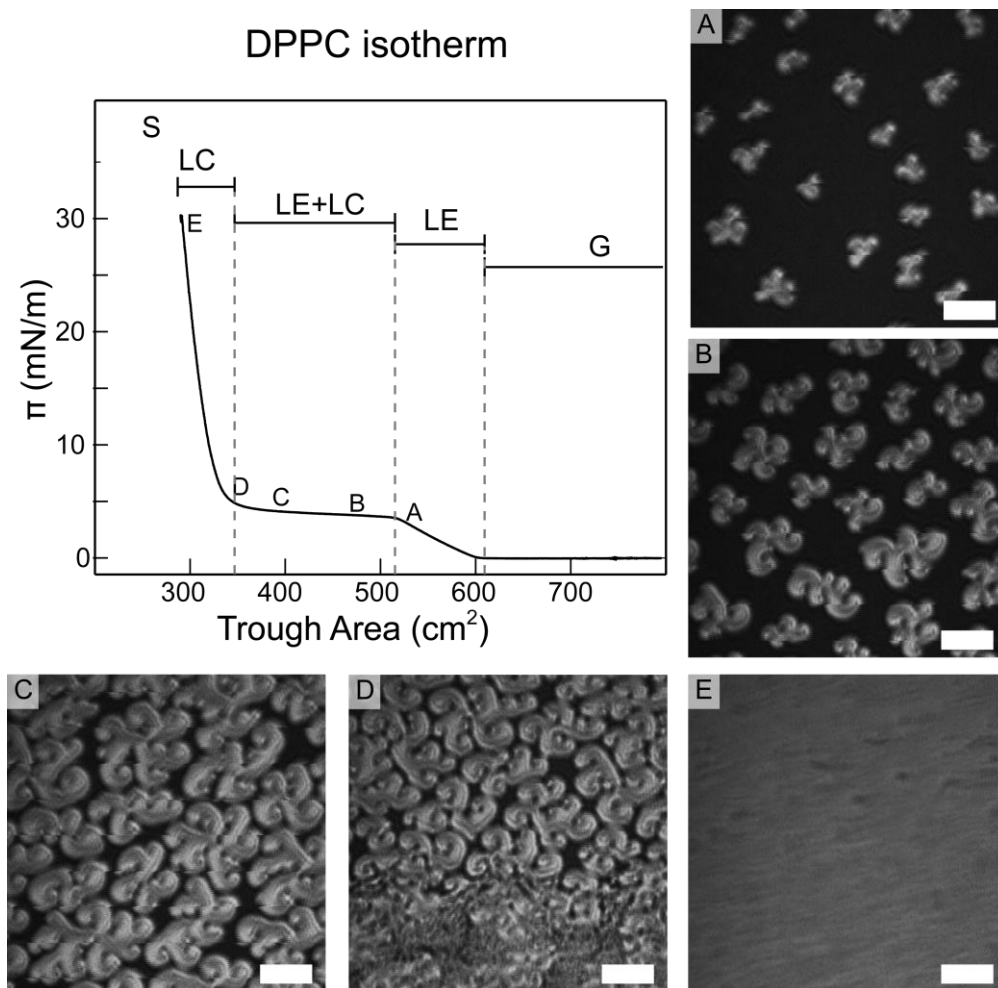


Figure 2.1 Isotherm of DPPC recorded at 20°C. A-E show BAM images have been recorded at different surface pressures corresponding to the letters in the graph. The scale bar is 50 μm .

(and competing) mechanisms, most of which is either a 3D structure, or vesicle/micelle formation in the water¹. [22]

In Figure 2.1A-E Brewster angle microscopy (BAM) images are shown of the LE-LC phase transition for a DPPC monolayer recorded at 20°C. The BAM technique will be explained in detail later in chapter 3, but for now it is an optical technique that allows the identification and distinguishing of different phases in a monolayer film. As soon as the DPPC film enters the phase transition region, identified as the start of the horizontal region, LC-domains starts to become visible as bright spots in the BAM image (Figure 2.1A). As the area is further reduced, and we move along the almost horizontal line in the isotherm, those domains grow in size as can be seen in Figure 2.1B+C. As the phase co-existing regions is exited, Figure 2.1D, the monolayer again begins to become uniform. At an elevated surface pressure, Figure 2.1E, the traces of the domains are completely gone, since the

¹ Most often it is encountered as a leaking of the trough, in which the surfactant molecules escape the confined area

entire monolayer is now in the LC-phase. The domain shape in Figure 2.1B-D can clearly be observed to have tendency towards a counter-clockwise rotation. This is due to the chiral nature of DPPC and if the other enantiomer were chosen the domain shape would be mirrored.[23]

It should be noted from the isotherm in Figure 2.1 that the area presented is the total trough area (A), normally the area will be presented as the area per surfactant (a), in $\text{\AA}^2/\text{molecule}$, since it is a more interesting property that contains information about the system instead of the instrumental setup. However those two of course have a linear dependency, as described below, where c is the molar concentration, v is the volume and N_a is Avogadro's number.

$$a = \frac{A}{N_a c v} \quad \text{Eq. 2.2}$$

In the G and LE phases the tail of the lipids are very dis-ordered and can take many conformations, due to the large area per surfactant. However, as the area is decreased the tail will become more ordered and the surfactant will attain a cylindrical shape. In most cases as the tails get ordered they will be tilted compared to the surface normal, which in many cases will correspond to the LC phase. As the surface pressure increases the tails will be increasingly vertical orientated, which in many cases will correspond to the S phase. The LC and the S-phase, however does not correspond to a single phase. The LC phases are divided into, at least, the L_2, L_2^*, L_1' , and L_2'' depending on different order parameters of the phase, the solid phase can be divided into the, 'super liquid' (LS), 'closed packed solid' (CS) and the solid (S) phases, again depending on the different order parameters.[24, 25] Which of the LC and S phase a particular system expresses depends on the surfactant, but also the surface pressure and temperature.

The cylindrical shape and the diversity of condensed phases, makes the coupling between surfactant monolayers and liquid crystals obvious.

2.2 Liquid Crystals

The fields of liquid crystals consist of the science of the mesophases that lies between the crystalline solids and the isotropic fluid phases, see Figure 2.2. They are classified as having high anisotropic properties, e.g. orientation, while exhibit a certain degree of fluidity. An essential requirement is for the molecule to have an anisotropic geometric shape, often in the form of a rod or a disc. The quantity of different mesophases that liquid crystals can exhibit is quite numerous; however they all fall within three categories, nematic, smectic and cholesteric, the two first are illustrated in Figure 2.2. The nematic is categorized by a long range orientational order, but no long range positional order, thus the individual molecules can diffuse freely between each other, but will keep the orientation. The smectic phase has a layered structure, where the layers are able to slide over on another, therefore the fluid like properties are preserved, however it is much more viscous than the nematic phase. The cholesteric phase is very close to the nematic phase but consist of optical active molecules, this induce a spontaneous twist about an axis perpendicular to the preferred molecular orientation.[26]

The smectic phase has many similarities with monolayers and bilayers of lipids or surfactants, due to the layered nature of this phase. Especially the fields of monolayers and liquid crystals have been closely coupled. An excellent example for this is the hexatic phase, which was introduced as a 2D phase intervening 2D fluids and liquids. The hexatic phase is characterized by a long range positional bond order and a short range positional order. [27-30] At first it was more of a theoretical phase with only few known examples of it. However in the early 90 the investigation of Langmuir monolayers was intensified due to advances in microscope and x-ray characterization techniques. This led to the discovery of several high density phases, for surfactant molecules, intervening the S- and LE-phase, of which at least four, the $LS, L'_1, L_2,$ and L_2^* have been classified as hexatic.[24]

Recently Kuhl et al. have produced results that show the hexatic phase might be present in lipid bilayers. They measure a short range positional order and the evidence of orientational texture through gracing incidence x-ray diffraction (GIXD).[31] We have produced similar results which show a long range orientational order measured by fluorescence microscopy.[16]

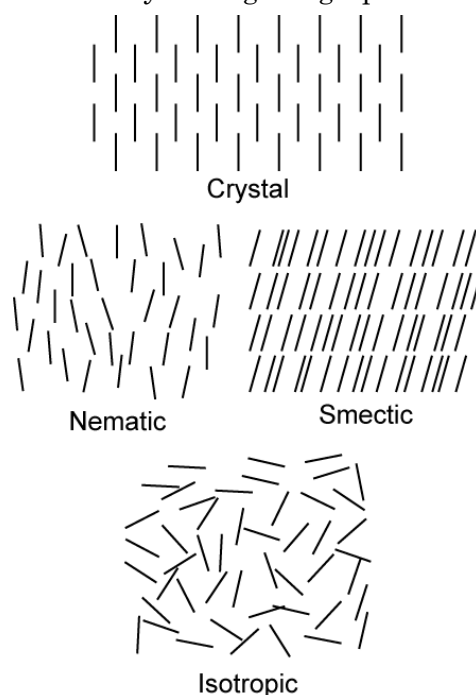


Figure 2.2 The two liquid crystal phases, nematic and smectic, intervenes the crystal and liquid phases. The nematic phase have a high degree of orientational order. The smectic phase is further ordered into layers.

2.3 The Hexatic Phases in Monolayers

Phase transitions have always been a popular topic for theoretical physicist, and Langmuir monolayers provide an excellent platform for studying 2D phase transition. As mentioned in the section above, at least four Langmuir monolayer phases have been identified to be hexatic. All of them were at area densities where the surfactants have a rod like conformation, so the discovery of mesophases should not be a surprise. Fischer et al. used the existing theory designed for the hexatic phase of symmetric liquid crystals developed by Nelson et al.[32, 33] to design a theory that were able to explain results emerging from monolayer studies.[20] They utilized existing observations of the orientational texture in monolayers as a control, since they wanted their theory to match up with existing experimental evidence. The

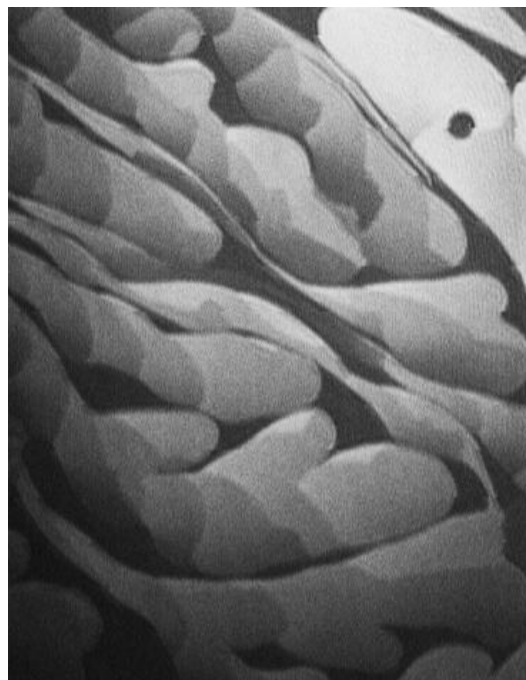


Figure 2.3 BAM image of a DMPE monolayer at 6 mN/m at 20°C. The different gray levels correspond to different orientations of the lipids, while the darkest areas correspond to the LE-phase. The width of the image is 370 μm

orientational texture was often visualized through techniques such as BAM in which the orientation of the surfactant is measurable in a probe free setup, as shown in Figure 2.3.

In this section the very basic of this theory is explained. It has been written with inspiration from Fischer et al.[20]. In order to evaluate the different orientational textures observed in monolayers we need a theoretical model that describes the energy of the texture in question.

Several features constitute the basic of a hexatic structure; these are also highlighted in Figure 2.4.

1. The hexatic grid that consist of the center of mass for the different lipids, also called the bond angle field. The angle θ is associated with this grid, which have 6 equivalent angles within the 2π range.
2. The projection of the lipid into the plane of the monolayer is called the c-director, which is a vector, and is linked with the angle φ .
3. The difference between the two angles (φ, θ) is dependent on the phase, which will be explained below.

The Landau free energy per area unit for a tilted hexatic surfactant monolayer is given by[20]:

$$f = \frac{1}{2}K_6(\nabla\theta)^2 + \frac{1}{2}K_1(\nabla\cdot\vec{c})^2 + \frac{1}{2}K_3(\nabla\times\vec{c})^2 + V[6(\theta-\varphi)] - \lambda_s \cos[6(\theta-\varphi)]\nabla\cdot\vec{c} - \lambda_b \sin[6(\theta-\varphi)]\vec{z}\cdot(\nabla\times\vec{c}) \quad \text{Eq. 2.3}$$

It consists of several different terms which we will describe in turns. The first term describes the energy cost of deforming the bond angle field described by the hexatic rigidity (K_6). The second and third term describes the deformation energy in regards to the c-director field. There are two

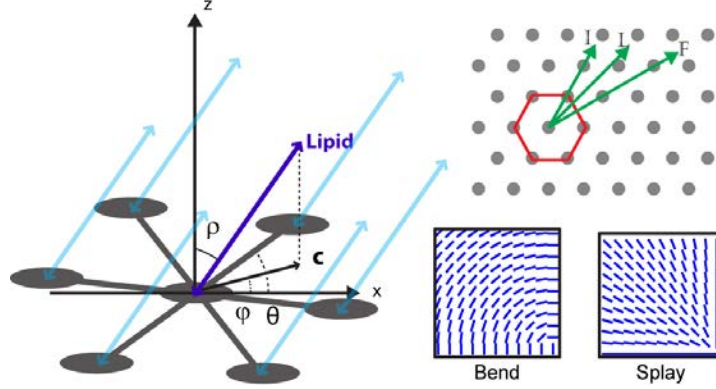


Figure 2.4 Identities for the hexatic grid

different deformation types, both shown in Figure 2.4:

1. Splay deformation described with the splay rigidity (K_1)
2. Bend deformation described with the bend rigidity (K_3)

All the rigidity constants (K_1, K_3, K_6) have the dimension of energy. The fourth term is a function (V) that describes the coupling between the bond angle field and the c-director field, described by the two angles φ and θ respectively. This function has to have a periodicity of $\frac{2\pi}{6}$ due to the symmetry of the hexatic phase. This function can be expanded as a Fourier series where the first two terms are shown below

$$V[6(\varphi - \theta)] \approx -h_6 \cos(6(\theta - \varphi)) - h_{12} \cos(12(\theta - \varphi)) \quad \text{Eq. 2.4}$$

This function controls the orientation of the c-director in regards to the bond angle field. The function can be minimized in three different cases, dependent on the magnitude and size of the two parameters (h_6, h_{12}) [20]. This result in three different hexatic phases, which is shown in Figure 2.4:

1. For $h_6 > 0$ and $h_6 > -4h_{12}$

$$\theta - \varphi = \frac{m(2\pi)}{6} \text{ for } m = 0, 1, 2 \dots 5 \quad \text{Eq. 2.5}$$

$$V \approx -h_6 - h_{12} \quad \text{Eq. 2.6}$$

This corresponds to the c-director pointing towards the nearest neighbor in the bond angle field. The liquid crystal phase associated with this is the smectic-I phase, in monolayer it is called the L_2 phase. In this thesis it will be called the I-phase.

2. For $H_6 < 0$ and $h_6 < 4h_{12}$

$$\theta - \varphi = \frac{\pi}{6} + \frac{m(2\pi)}{6} \text{ for } m = 0, 1, 2 \dots 5 \quad \text{Eq. 2.7}$$

$$V \approx h_6 - h_{12} \quad \text{Eq. 2.8}$$

This corresponds to the c-director pointing towards the next-nearest neighbor in the bond angle field. The liquid crystal phase is the smectic-F phase, in monolayer it is called the L_2^* phase. In this thesis it will be called the F-phase.

3. For $h_{12} < 0$ and $-4h_{12} > h_6 > 4h_{12}$

$$\theta - \varphi = \pm\alpha + \frac{m(2\pi)}{6} \text{ for } m = 0,1,2 \dots 5 \quad \text{Eq. 2.9}$$

$$V \approx -h_6 \cos(6\alpha) - h_{12} \cos(12\alpha) \quad \text{Eq. 2.10}$$

This corresponds to the c-director pointing toward an intermediate point between the nearest and next nearest neighbor. The liquid crystal phase is the smectic-L phase, in surfactant monolayers it is called the L_1' phase. In this thesis it will be called the L-phase, which is a chiral phase. The sign in front of the alpha determines whether it is a left or right handed chirality. Notice that the chirality here goes for the phase and not the surfactant in questing.

The last two terms in Eq. 2.3 are special for monolayers, and are required because of the asymmetry of the two interfaces (air/water) and the head-tail asymmetry.

$$-\lambda_s \cos[6(\theta - \varphi)] \nabla \cdot \vec{c} - \lambda_b \sin[6(\theta - \varphi)] \vec{z} \cdot (\nabla \times \vec{c}) \quad \text{Eq. 2.11}$$

Important to notice is that the second term in above equation is nonzero only for the F-phase. Therefore it can be used to create a chirality order parameter defined below:

$$X \equiv \langle \sin(6(\varphi - \theta)) \rangle \quad \text{Eq. 2.12}$$

Next we want to look at the energy at the interface between the LC domain and LE surroundings. This is of course dependent on the angle between the c-director and the normal vector at the boundary of the domain, and therefore on the dot product of those. This has been expanded in a Fourier series below[20].

$$f_i = \oint ds \{ \gamma - \Gamma_1 \vec{c} \cdot \vec{n} - \Gamma_2 [2(\vec{c} \cdot \vec{n})^2 - 1] - \dots \} \quad \text{Eq. 2.13}$$

Where γ represent the isotropic line tension. The two boundary constants Γ_1 and Γ_2 determine the preferred orientation of the c-director in regard to the normal boundary. The specific angle can be found by minimizing this equation, and the result is shown in Figure 2.5. Γ_1 describes the head-tail asymmetry since it, and it alone, distinguish parallel and anti-parallel orientation. An interesting result is that parallel boundary conditions is only allowed for $\Gamma_1 = 0$, which would imply that the lipids have a head-tail symmetry, and therefore explain the rarity of

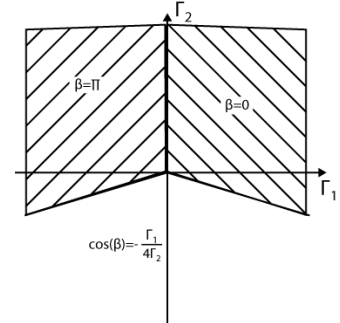


Figure 2.5 The angle between the c-director and the boundary normal dependence on the two boundary constants.

observations of monolayers with parallel boundary conditions. The above equation strictly holds true only for the I-and F-phase. The L-phase gives a similar result, but with a deviation proportional to the chiral order parameter. It is important to notice that most of the texture observed in monolayers exhibit normal boundary conditions; therefore we can assume that $\Gamma_1 \gg \Gamma_2$ to ensure the normal boundary condition. However it is important to notice that $|\Gamma_1|$ needs to be smaller than the isotropic line tension, otherwise a situation could arise where the interfacial energy would be negative, which is forbidden.

With Eq. 2.3 and Eq. 2.13 we are able to estimate the energy of different textures for monolayer system. Firstly we will start in a system where the c-director is locked to the hexatic grid. This simplifies the equations above to the following two, for the area and boundary respectively.

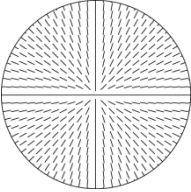
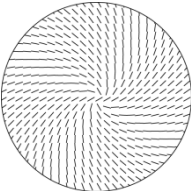
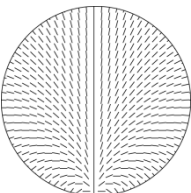
$$F_b = \int \left\{ \frac{1}{2} (K_1 + K_6) (\nabla \cdot \vec{c})^2 + \frac{1}{2} (K_3 + K_6) (\nabla \times \vec{c})^2 \right\} dydx \quad \text{Eq. 2.14}$$

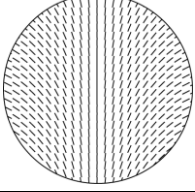
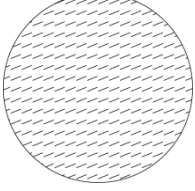
$$F_s \approx \gamma \oint ds - \bar{\Gamma}_1 \oint (\vec{c} \cdot \vec{n}) ds - \bar{\lambda}_b \oint (\vec{z} \cdot \vec{c} \times \vec{n}) ds - \Gamma_2 \oint (2(\vec{c} \cdot \vec{n})) ds$$

$$\bar{\Gamma}_1 = \Gamma_1 + \lambda_s \cos(6(\theta - \varphi)) \quad \text{Eq. 2.15}$$

$$\bar{\lambda}_b = \lambda_b \sin(6(\theta - \varphi))$$

The above equation can then be used to calculate the energy for different texture, this have been done in the table below where images of the corresponding texture is shown as well.[20] In these equations the disclination core energy are introduced ($E_c(m=1)$, $E_c(\text{boojum})$) which describes the energy of the point disclination in the orientational texture on the size order of a_0 where the theory described above is invalid.

Director field	C-director	$F_{name} = F_b + F_s$
	$\vec{c} = \begin{pmatrix} \cos(\varphi) \\ \sin(\varphi) \end{pmatrix}$	$F_{splay} = 2\pi \ln(R/a_0) [K_1 + K_6] \dots$ $+ 2\pi R (\gamma - \bar{\Gamma}_1 - \Gamma_2) + E_c(m=1)$ Eq. 2.16
	$\vec{c} = \begin{pmatrix} \cos(\theta + \varphi_0) \\ \sin(\theta + \varphi_0) \end{pmatrix}$ where $\varphi = \theta + \varphi_0$	$F_{mix} = 2\pi \ln\left(\frac{R}{a_0}\right) [K_6 + K_1 \cos^2(\varphi_0) + K_3 \sin^2(\varphi_0)] \dots$ $+ 2\pi R [\gamma - \bar{\Gamma}_1 \cos(\varphi_0) - \Gamma_2 \cos(2\varphi_0) - \bar{\lambda}_b \sin(\varphi_0)] \dots$ $+ E_c(m=1)$ Eq. 2.17
	$\vec{c} = \begin{pmatrix} \cos(2\varphi) \\ \sin(2\varphi) \end{pmatrix}$	$F_{boojum} = 2\pi \ln\left(\frac{2R}{a_0}\right) \left[K_6 + \frac{1}{2} (K_1 + K_3) \right] \dots$ $- 0.2(K_1 + K_6) - 0.9(K_3 + K_6) \dots$ $+ 2\pi R (\gamma - \bar{\Gamma}_1 - \Gamma_2) + E_c(\text{boojum})$ Eq. 2.18

	$\begin{aligned} \varphi(x, y) &= \varphi_0 + ax + b + cxy \\ &+ d(x^2 + y^2) \dots \\ K_1 &= K_3 \end{aligned}$	$F_{\text{Virtual Boojum}} = \frac{1}{2}\pi R^2(K_6 + K)(a^2 + b^2) \dots + 2\pi R\gamma + \frac{1}{2}\Gamma_1 bR^2 \quad \text{Eq. 2.19}$
		$F_{\text{uniform}} = 2\pi R\gamma \quad \text{Eq. 2.20}$
		$F_{\text{nearly uniform}} = 2\pi R\gamma - \frac{\Gamma_1^2 R^2}{8\pi(K_6 + K)} \quad \text{Eq. 2.21}$

Those are of course rather extended equations, for textures that are relatively simple. A thorough analysis of those results is beyond the scope of this thesis. However a few comments on the last few are needed. The uniform texture would seem like a low energy texture, and indeed in three dimensional system of liquid crystals it is the ground state. [20] However in order for the uniform texture to be lowest in energy the radius need to be small.

$$F_{\text{uniform}} < F_{\text{splay}} \quad \text{Eq. 2.22}$$

$$R < \frac{E_c(m=1)}{|\bar{\Gamma}_1|} \wedge R < \frac{(K_1 + K_6)}{|\bar{\Gamma}_1|} \quad \text{Eq. 2.23}$$

Therefore the uniform texture is only allowed for small domains. However the energy for the nearly uniform texture in Eq. 2.21, which is a special case for the virtual boojum, where the center is very far from the domain, will always have a lower energy than the uniform texture.

It is however interesting to think that these complex patterns are the result of ordering the lipid tails at the domain interface, which is done by a continuously change of the hexatic grid. Another way to achieve this would be to keep the orientation constant in subdomains that are bound by defect lines, in which the c-director undergoes a rapid jump from one equilibrium value to another equilibrium value. The reason for introducing defect lines are the relative high energy cost of the disclination center for those texture described above, due to the continuously change of orientation.

In the following section the discussion will be limited to the I- and F-phase, and thus the chiral

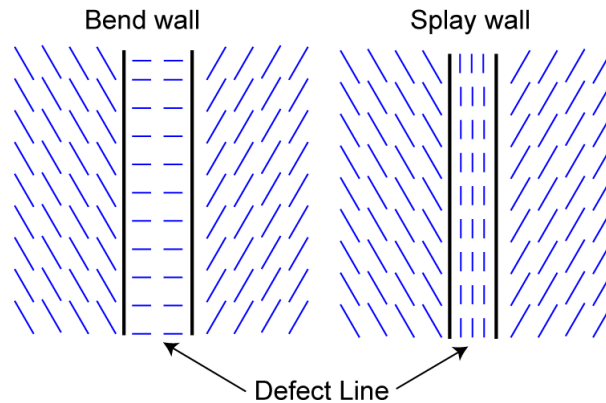


Figure 2.6 The two basic type of defect wall that the I- and F- phase exhibit. The bend wall with a $\psi = \pi/2$, and the splay wall with $\psi = 0$

L-phase will be left out. In the end of this section a short summary for the result for the L-phase will be presented. As mentioned earlier in this section, the c-director has 6 equivalent orientations towards the hexatic grid. Therefore it would make sense to divide the domain into six subdomains each with a separate orientation. These subdomains would then be separated by 6 defect lines. The average orientation within the defect line is given by the equation below.

$$\bar{c} = \frac{1}{2}(\vec{c}_1 + \vec{c}_2) \quad \text{Eq. 2.24}$$

Where \vec{c}_1 and \vec{c}_2 are the orientations for two neighboring subdomains with a difference of $\pi/3$ between them. Let ψ be the angle between \bar{c} and the tangent to the defect line. For $\psi = 0, \pi$ it is a pure splay wall, while $\psi = \frac{\pi}{2}, \frac{3\pi}{2}$ is a pure bend wall as illustrated in Figure 2.6. The task is then to find the line tension for the defect line, since it will be related to the energy cost of the defect line. The line tension as a function of ψ will clearly have a 2π periodicity; therefore it is again possible to make a Fourier series that describes it.

$$\epsilon(\psi) = \sum_{n=0}^{\infty} A_n \cos(n\psi) \quad \text{Eq. 2.25}$$

Where the three first coefficients are[20]:

$$A_0 = \epsilon_0 \equiv \frac{1}{2}(\epsilon_{splay} + \epsilon_{bend}) \quad \text{Eq. 2.26}$$

$$A_1 = \pm \left[\frac{(\gamma_b + \gamma_s)}{5} + \frac{\gamma_b - \gamma_s}{7} \right] \quad \text{Eq. 2.27}$$

$$A_2 = \epsilon_0 \left[\frac{K_1 - K_3}{K_1 + K_3} \right] \quad \text{Eq. 2.28}$$

It turns out that the two most important parameters are A_0 and A_2 , therefore the line tension can be described as:

$$\epsilon(\psi) = \epsilon_0 \left(1 + \left[\frac{K_1 - K_3}{K_1 + K_3} \right] \cos(2\psi) \right) \quad \text{Eq. 2.29}$$

An interesting note from the equation above is that whichever is greatest of K_1 and K_3 determines which of the two defect types from Figure 2.6, which have the lowest line tension. For $K_1 > K_3$ the lowest line tension will be when $\psi = \frac{\pi}{2}$, meaning a bend wall have a lower energy than the splay wall, if $K_1 < K_3$ the opposite is true.

Using this we can now calculate the energy of a defect line using Eq. 2.29, again neglecting the $n=1$ term, here done for a straight defect line with length L and $\psi = 0$

$$\Delta E_{defect\ line} \approx \oint_0^L \epsilon_0 \left(1 + \left[\frac{K_1 - K_3}{K_1 + K_3} \right] \cos(2\psi) \right) ds = \epsilon_0 L \left(\frac{2K_1}{K_1 + K_3} \right) \quad \text{Eq. 2.30}$$

This allows the calculation of the energy for a hexagonal domain divided into 6 subdomains separated by a defect line, the domain is illustrated in Figure 2.7A.

$$F_{defect\ lines} = 6R_h\epsilon_0\left(\frac{2K_1}{K_1 + K_3}\right) + 6R_h(\gamma - |\bar{\Gamma}_1| - \Gamma_2) + E_c(defect\ lines) \quad \text{Eq. 2.31}$$

Where R_h describes the radius of corresponding circle that would surround the hexagon, and therefore also the length of the six sides. The first term describe the energy of the 6 defect lines from Eq. 2.30, the second term describes the energy associated with the domain interface from Eq. 2.15, and the last term represent the energy from the point defect in the center, which differ from the one in the equations in the table above. It is interesting to compare the energy with the energy of a domain of same size and shape, but with a uniform texture with no defect lines, see Eq. 2.20.

$$F_{uniform} = 6R_h\gamma \quad \text{Eq. 2.32}$$

In order for the texture with defect lines to have a lower energy it follows that:

$$F_{defect\ lines} < F_{uniform} \quad \text{Eq. 2.33}$$

$$R_h > \frac{\frac{1}{6}E_c(defect\ lines)}{(|\bar{\Gamma}_1| + \Gamma_2) - \epsilon_0\left(\frac{2K_1}{K_1 + K_3}\right)} \quad \text{Eq. 2.34}$$

This equation again confirms that the uniform texture is only allowed for sufficient small domains. A similar comparison can be made between the domain with a continuously splay texture, Eq. 2.16, and the one with defect lines. That comparison result in a large equation, which basically involves all the parameters used to calculate the energy, therefore it is not shown. [20] It should be noted that sometimes the defect line is not straight but instead have kinked structure, as seen in Figure 2.7B. Whether the lines are kinked or straight depend on the relation between K_1 and K_3 .

An interesting parameter is the healing length; it describes how rapid the angle between the hexatic grid and the c-director will re-approach the equilibrium value, in other word the thickness of the defect lines. It is given by the equations below for a splay defect and a bend defect respectively.

$$\xi_{splay} = \left(K_1/h_6\right)^{\frac{1}{2}} \quad \text{Eq. 2.35}$$

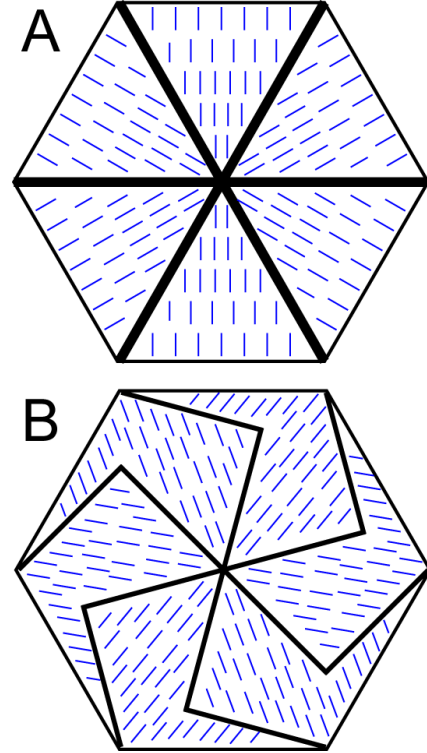


Figure 2.7 Two different defect lines for the I- and F-phase, with either straight (A) or kinked (B) defect lines

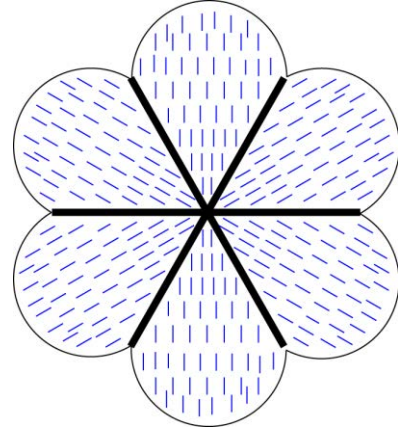


Figure 2.8 The rosette shape, seen for some monolayers domains, with a high line tension for the defect lines.

$$\xi_{bend} = \left(K_3 / h_6 \right)^{\frac{1}{2}} \quad \text{Eq. 2.36}$$

What makes these parameters especially interesting is the fact that they, as mentioned before, are observable as the thickness of the defect line. Hénon et al. measured this width using Brewster angle microscopy (BAM) for monolayers of fatty-acids and found it to be around 3 μm . [34]

The last thing to consider is the shape of the domains. It is controlled by three parameters:

4. The line tension, γ , which works to minimize the circumference of the domain.
5. The energy gain by having normal boundary condition, controlled by Γ_1 .
6. The energy of the defect lines, controlled by the isotropic line tension of the defect lines, ϵ_0

If $\gamma \gg \Gamma_1$ the domain will be round in order to minimize the circumference, if $\gamma \approx \Gamma_1$ we will have a hexagonal shape, since it maintains a short circumference while keeping normal boundary conditions. Lastly if ϵ_0 is large the domain will attempt to minimize those, which can be done by creating rosette shape domain as depicted in Figure 2.8.

The last subject to be discussed is the defect lines in the chiral L-phase. As can be seen in Eq. 2.9 there are 12 minima in the function that controls angle between the c-director and the hexatic grid. It means there can be 12 defect lines, however they are split into two groups, type-I and type-II walls. [20] The type-I wall will have a change in orientation of 2α while the type-II wall have a change of $\frac{\pi}{3} - 2\alpha$. As a reminder the sign in front of α in Eq. 2.9 determines whether it was left- or right-handed chirality, which means that going across a type-I wall the chirality of the texture will switch.

Type-I and -II walls can either repel or attract each other. [20] If they repel each other the domain will have 12 distinct defect lines and sub domains where the defect lines are alternating type-I and -II. Half the subdomains are right-handed chiral and the other half left-handed. This result in a net achiral domain with straight defect lines, and the shape is a rounded dodecagon. However if they attract each other they will combine to a $\frac{\pi}{3}$ defect wall, and the handedness of the chirality will persist. This will affect the shape of the defect lines, which can be described as the parabola below:

$$y'' = k \frac{\sqrt{3}(K_3 - K_1)}{2K_3 + K_1} \quad \text{Eq. 2.37}$$

Where k is the “vorticity” which is proportional to the chiral order parameter X as defined in Eq. 2.12. An illustration for such a domain with parabolic defect lines can be seen in Figure 2.9. This parabola representation of the defect line has the advantage of being measureable in techniques that allows you to measure the defect line, e.g. BAM, AFM etc.

The purpose of the section above was to give an introduction to theoretical work that has been done in order to explain the observed textures exhibited by monolayer systems. Several examples have been shown in which certain parameters are accessible experimentally. The theory described above is not directly applicable to all the result in this thesis, mainly because the major experimental systems are based on bilayers, which is not easily explained using the theory above. However through this thesis the theory explained above will be taken into consideration when interpreting the results from the bilayer system. Similarities and differences between the two systems will be highlighted.

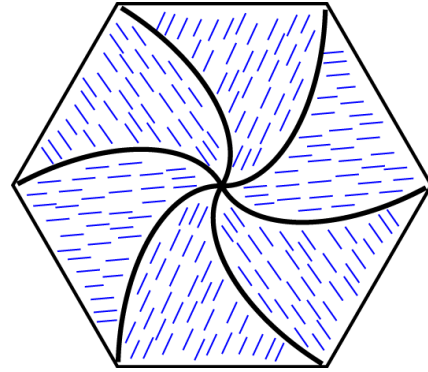


Figure 2.9 The resulting texture for the L-phase, when the type-I and -II wall attract and combines.

2.4 Phases and Phase Separation in Bilayers

Most of the experiments described in this thesis are done on lipid bilayers. Therefore the last section of this chapter will explain phase behavior in lipid bilayer systems

A self assembled lipid bilayer may undergo a thermotropic phase transition (induced by temperature). If the bilayer consists of a single species of phospholipids the phase transitions will be very well defined and confined to a narrow temperature range. At reduced temperature the lipid head-groups will be well ordered, their tails will be stretched and the movement of the lipids will be very slow, this phase is called the solid ordered phase, the gel phase, or $L_{\beta'}/L_{\beta}$, where the mark atop the beta sign designate that the lipid tails are tilted in respect to the normal of the bilayer. As the bilayer is heated the order will vanish, the tail will become more randomly formed and the diffusion of the lipids will increase drastically. This phase is called the fluid phase, liquid disordered or L_{α} . In this thesis the L_{α} and $L_{\beta'}$ phase will be used as the notation. The temperature at which this transition takes place is called the transition temperature (T_m). As a bilayer undergoes the transition from $L_{\beta'} \rightarrow L_{\alpha}$ the area per lipid is increased, and the thickness of the bilayer decreases. This is a natural consequence of the melting of the chains.

Even for simple lipid model system the phase behavior is not as straight forward as described above. The bilayers can form other phases that need to be taken into account, for instance the $L_{\beta'}$ phase is not the most ordered phase, and hydrated saturated phosphocholine lipids, e.g. DPPC, can undergo a phase transition when cooled from the $L_{\beta'}$. This phase is called the sub-gel phase or L_c phase, and is characterized by an even closer packing of the lipids.[35] The L_c phase is however not a concern for the work in this thesis, due to the $L_c \rightarrow L_{\beta'}$ phase transition happening at a temperature well below the ones used in this thesis. More troublesome is the ripple phase ($P_{\beta'}$), which lies in between the L_{α} and $L_{\beta'}$ phase. It is a phase characterized by periodic corrugation in the lipid bilayer. The $P_{\beta'}$ phase is somewhat oppressed in supported lipid bilayers, and is therefore not observed in the bilayer closest to the support, however bilayers further from the support can exhibit this phase.[36, 37]

The most of the work in this thesis have been done on binary mixtures of lipids. In binary mixtures the possibility for phase coexistence exists, therefore it is very insightful to study phase diagram for binary mixtures. The phase diagram can look differently depending on the miscibility of the two components for the difference phases. Two different examples, relevant for the results presented later in this thesis, will be presented here[38].

1. Isomorphous, in which the two lipids are completely miscible in both the L_{α} and $L_{\beta'}$ phase.
2. Eutectic in which the two lipids is immiscible in the gel phase.

First the basic properties of a phase diagram will be described, using the POPC,DMPC phase diagram seen in Figure 2.10 as an example, it has been redrawn from[39], this is very close to an isomorphous mixture, in which the lipids are miscible in both phases. The phase diagram is divided into

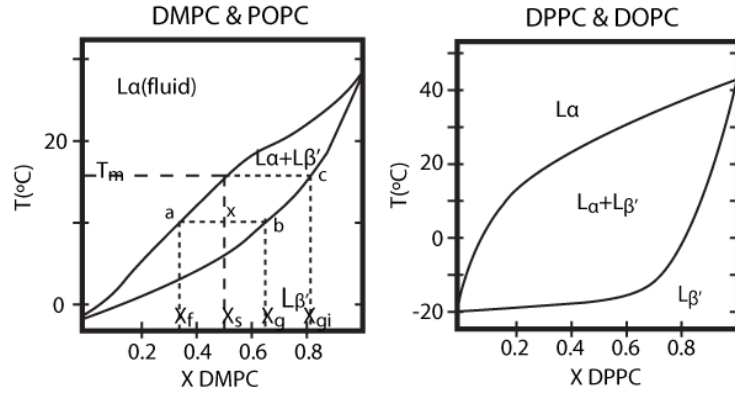


Figure 2.10 The phase diagram for POPC,DMPC and DPPC,DOPC. The letters in the first one is used to explain the basic properties of a phase diagram. The phase diagrams are redrawn from the references.

three regions, the L_α region in the top, the $L_{\beta'}$ region in the bottom, and the coexisting region in between. If a mixture with a X_S molar fraction of DMPC (e.g. 0.5, see Figure 2.10) is cooled from the fluid region into the coexistences region, then at temperature T_M the bilayer will begin to divided into the two phases. The $L_{\beta'}$ phase will begin to solidify, the molar fraction of that can be found by using the tie line, which is horizontal in a binary phase diagram. The molar fraction of $L_{\beta'}$ can be seen in the figure at point c, and it correspond to X_{GI} (≈ 0.8), the molar fraction of the L_α remains X_S (≈ 0.5). As the sample is cooled further to about 10°C more of $L_{\beta'}$ will solidify. The sample will now be divided in two phases each with a distinct molar fraction. Again the molar fraction can be found using a tie line, for the $L_{\beta'}$ it is now X_G (≈ 0.65), while the L_α is X_F (≈ 0.35). Another important parameter that can be extracted from the phase diagram is the relative proportions of the different phases. They can be calculated using the lever rule, and are defined as below. The letter refers to Figure 2.10.

$$f_{L\alpha} = \frac{b - x}{b - a}, f_{L\beta} = \frac{x - a}{b - a} \tag{Eq. 2.38}$$

Where $f_{L\alpha}, f_{L\beta}$ represent the fraction of the L_α and $L_{\beta'}$ phase respectively. It is important to remember that $f_{L\alpha}$ and $f_{L\beta}$ are molar fraction and not area fraction, since the area for each lipid is smaller in the later phase. Therefore they cannot be directly compared to area fractions obtained from fluorescence images for instance. It is important to notice that the fraction of the $L_{\beta'}$ is dependent on the temperature, and therefore as a sample is cooled down, the fraction of $L_{\beta'}$ will increase and thus domains are formed non-isothermally. This is shown in a series of fluorescence images of a DOPC, DPPC (1:1) bilayer at different temperatures in Figure 2.11, using the fluorescence probe DiI the L_α becomes bright while the $L_{\beta'}$ is dark. Another thing to notice from the phase diagram is that the composition of both phases change with temperature, for the POPC,DMPC phase diagram both

phases become enriched in POPC, as the temperature is lowered. This implies that as the temperatures is lowered; POPC should diffuse into the already formed domains. Therefore if a sample is cooled very rapidly a compositional in-equilibrium can occur.[38]

A generic, and theoretical, example of a eutectic phase diagram is shown in Figure 2.12. The difference from the isomorphous phase diagram is that the two L_{β} -phases are completely immiscible, therefore as the sample is cooled only one of the components can solidify, until the temperature is below T_E at which the other lipid will solidify as well. The point where

the two curves meet is called the eutectic point (marked with an 'e' in Figure 2.12). The phase diagram of two lipids, with immiscible L_{β} phase can differ from the one presented in Figure 2.12. Firstly the two lipids are rarely completely immiscible. Secondly the eutectic point may lie very close to the pure composition, in which case it can be very difficult to detect experimentally.[38] An example for these deviations are the DOPC,DPPC phase diagram shown in Figure 2.10, it has been redrawn from[40]. The miscibility can be seen by the fact that the right line between the coexisting region and L_{β} region is not completely vertical. Secondly there is no evidence of the eutectic point. The same argumentation about domain growth, lever rule and tie lines holds true for this phase diagram.

There are other phases than the two mentioned above, however the L_{α} and L_{β} phases are the most important phases for understanding the work described in this thesis. However one phase needs mentioning due to its importance within the work of model membrane: the sterol, e.g. cholesterol, enriched liquid-ordered phase (L_o). It is a phase intervening between the solid-ordered (S_o) and the liquid-disordered (L_D) phases, here using L_D and S_o to stay within that terminology. It was introduced by Ipsen et al. in 1987, to explain the effect of cholesterol on the membrane[2]. The L_o

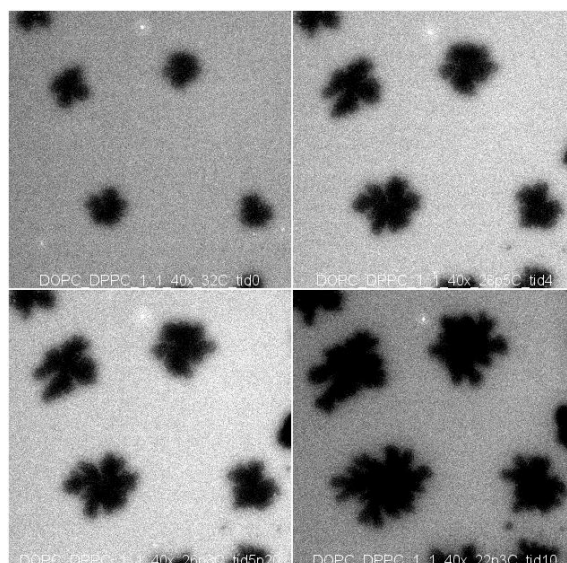


Figure 2.11 Images of a DOPC,DPPC (1:1) bilayer at 4 different temperatures(going top-left, to bottom-right):32°C, 28.5°C, 26.3°C and 22.3°C. Showing that the L_{β} domains (dark) grow non-isothermally. The widths of the images are 64 μ m

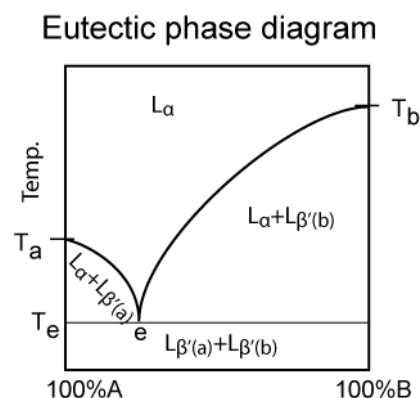


Figure 2.12 An example of an Eutectic phase diagram, for two compounds A,B with immiscible gel phases.

phase is characterized by having ordered tails, as the S_0 phase, but the high mobility/diffusion from the L_D phase, and therefore no positional order. It has great importance for life sciences due to the high concentration of cholesterol in eukaryotic cell membranes, where 30-50% of all lipids are cholesterol.[1]

Chapter 3

Fabrication and characterization

This chapter will describe the different techniques used for characterization and fabrication of lipid bilayers will be described. This includes fluorescence microscopy, Atomic force microscopy (AFM), BAM, and fabrication of supported lipid bilayers, as well as a closer inspection of the fluorescence probe Laurdan. In the end of this chapter a description of the different procedures, equipment and materials will be listed.

3.1 Fluorescence Microscopy

Fluorescence is the ability of an atom, molecule, or material to emit light after an absorption of energy for instance in the form of light. This is easiest explained by using a generic Jablonski diagram as presented in Figure 3.1A. A fluorophore, i.e. a molecule capable of emitting fluorescence light, is initially in a stable ground state, if the fluorophore absorbs a photon its energy will rise to an excited state, the energy of this excitation light is given by the wavelength λ_{ex} . Shortly after the excitation the fluorophore will relax back to its ground state, and in the process emit light at wavelength λ_{em} . The energy of the emitted light will be

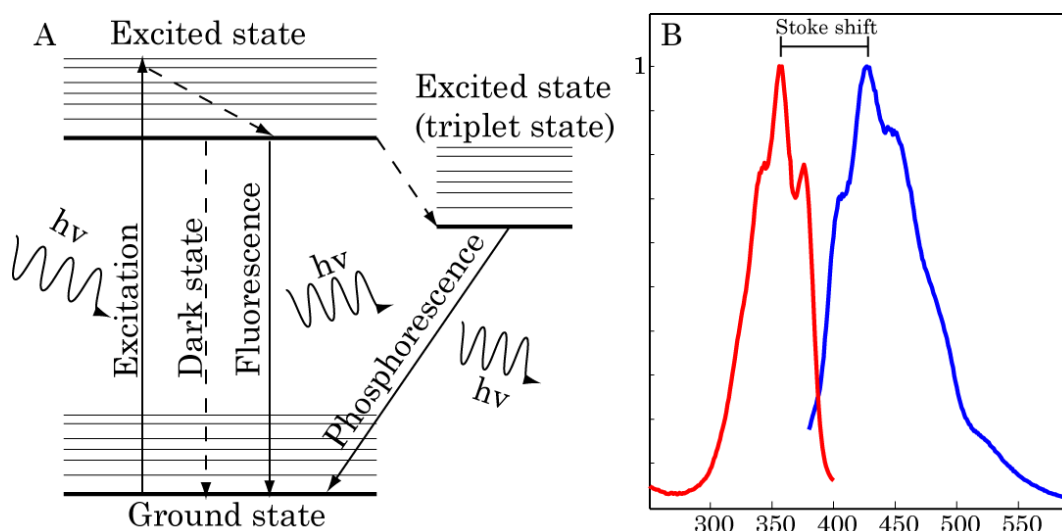


Figure 3.1 A) Jablonski diagram, showing the absorption of a photon (excitation), followed by emission of a photon (fluorescence or phosphorescence) or loss of energy through a dark state. B) Generic fluorescence spectrum, the absorption spectra (red) are at lower wavelength than the emission spectra (blue). The difference between the two maxima is called the Stokes shift.

lower than the energy of the excitation light, due to some energy loss in the process. There are alternated ways for the fluorophore to reach the ground state. These includes an internal conversion in which no emission of light occur (dark state), and through a “forbidden” conversion to a metastable triplet state. Conversion from the triplet state to the ground state, which is equally “forbidden”, is slow, resulting in emitting decay ranging from several seconds to hours, this conversion is called phosphorescence. The loss of energy from absorption of light to emission can be observed in fluorescence spectrum as a shift of the emission spectra to a higher wavelength, a generic spectra is shown in Figure 3.1B. The difference between the two peaks position, i.e. the absorption/excitation and emission, is called the stokes shift.[41]

The use of fluorescence molecules is a powerful tool in microscopy. It allows for a precise mapping of the individual fluorophores in a sample. The essential parts of a fluorescence microscope are schematized in Figure 3.2. The sample is illuminated by an appropriated light source focused on the sample by the microscope objective. This light excite the fluorophore, which is followed by an emission of light at a higher wavelength. Some of the emitted light is collected by the microscope objective, and is subsequently recorded by the camera. Notice it is the same objective used to focus the light on the sample and collect the emitted light, thus fluorescence microscopy does not need a separate condenser. This is made possible by the filter cube that contains an excitation filter, a dichroic mirror and an emission filter. The light source is normally a broad spectrum of wavelengths, the excitation filter (low pass) removes the light with a wavelength above a certain value, the dichroic mirror works as a mirror for the excitation light, while Stokes shifted emission light is allowed to pass through it. The emission filter is a high pass filter that only allows light above a certain wavelength to pass it. One of the purposes of the filter cube is to avoid scattered light from the light source to reach the camera, since the intensity of scattered light will be much greater than the intensity of the fluorescence light.[41]

It is possible to excite a fluorophore using more than one photon, as is utilized in 2-photon/multi-photon laser scanning microscopy. In this method the fluorophore adsorbs 2 or more photons simultaneously bringing it to the same excited state as 1-photon excitation. The simultaneously absorption only occurs at very high light intensities, and therefore a high powered pulsing laser is used

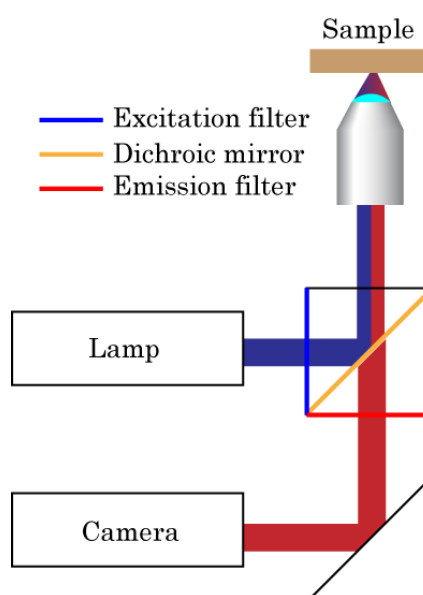


Figure 3.2 Schematization of a fluorescence microscope. The filter cube contains a excitation filter (blue), a dichroic mirror (orange) and the emission filter (red), it ensure only the emission light (maroon) reaches the camera.

together with a high NA objective to focus the light onto a very small spot in the sample.[41] The emission spectrum for a fluorophore is identical for 1- or 2- photon excitations, since the emission spectrum only depends on the energy levels of the fluorophore. In principle the absorption of 2 photons should occur at twice the wavelength of 1-photon, however differences in the two absorption spectra do occur[42]. The usage of 2-photon fluorescence microscopy offers many advantages, like a small focal area resulting in low background fluorescence, excitation in the infrared region as opposed to ultraviolet etc. In this thesis the fluorescence microscopy has been done by polarized 2-photon fluorescence microscopy, but none of the reasons above are really applicable to the work on model membranes. The reason 2-photon excitation was chosen, was related to the fluorophore Laurdan which will be described in the next section.

3.2 Laurdan

One of the main tasks in this thesis was to measure the orientational texture of $L_{\beta'}$ domains in lipid bilayers. In order to achieve this, a fluorescence probe that fulfills a number of criteria was needed. It should be:

- partitioning in the $L_{\beta'}$ phase
- able to distinguish between the different phases of the membrane
- sensitive towards the orientation of the lipids

Laurdan, which molecular structure can be seen in Figure 3.3A, fulfills all those criteria. It partitions in both the L_{α} and $L_{\beta'}$ phases, but it has a phase depended emission shift that allows us to distinguish the different phases. The fluorescence spectrum for laurdan was recorded and can be seen in Figure 3.3B. Those spectra were recorded from small unilamilar vesicles (SUV) of DPPC, with 0.5% molar of Laurdan, both above (55°C) and below (20°C) the phase transition. From the spectra in Figure 3.3B it can clearly be seen that the L_{α} phases (green line, 55°C) causes a red shift compared to the $L_{\beta'}$ phase (blue line, 20°C). The positions of the two peaks are 475nm and 440nm respectively. As a control SUV of POPC, with Laurdan, were also recorded at before mentioned two temperatures, to test whether the red shift was caused by the temperature or the phase difference between the two samples. POPC is in the L_{α} phase at both those temperatures. The POPC SUV gave identical emission spectra for both temperatures, confirming that the differences in the spectra are caused by the phase difference. Those measurements match well with the literature concerning Laurdan.[43]

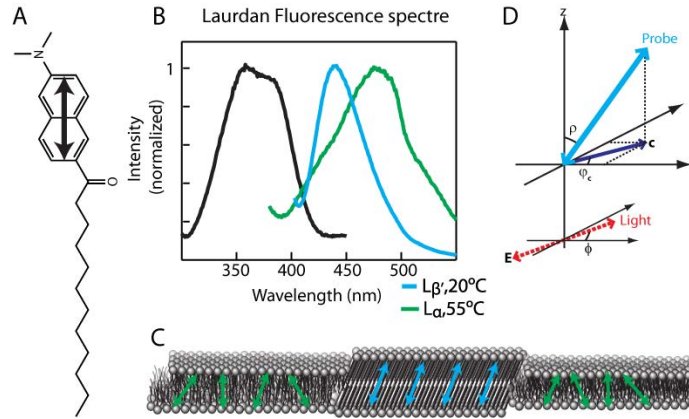


Figure 3.3 The fluorescence probe Laurdan (A) partitions both in the L_α and $L_{\beta'}$ phase, in the first it is randomly orientated, while it is ordered as the lipids acyl tails in the latter (B). The emission spectra is phase dependent (C) and will be red-shifted for the L_α -phase (green), compared to the $L_{\beta'}$ phase (blue). Due to the dipolar moment of Laurdan (shown in A by the arrow), it is sensitive to polarization of the light, and if the polarization is perpendicular the probe, it will remain dark. The projection of the probe into the plane of the bilayer is called the c-director (D).

This phase dependent emission shift of Laurdan is utilized in the 2-photon fluorescence microscope setup. The emission light is split into two channels by a dichroic mirror at 475 nm and collected in two separate channels each with a band pass filter: $438 \pm 12 \text{ nm}$ corresponds to the $L_{\beta'}$ phase and $494 \pm 10 \text{ nm}$ to the L_α phase. The relationship between those channels, defined as the generalized polarization (GP) function, can reveal information about the phase state of the membrane.[44, 45] For the work in this thesis the $438 \pm 12 \text{ nm}$ channel contains the important information.

Laurdan has a fluorescent dipolar moment, as marked by the arrow in Figure 3.3A, and is therefore sensitive towards polarized light. The Laurdan that partitions in the L_α phase will have a random orientation due to the disorder associated with this phase, and hence the orientations of Laurdan is isotropic. In the $L_{\beta'}$ phase the Laurdan molecules will assume the same order as the lipids. This is illustrated in Figure 3.3C where the green and blue arrows correspond to Laurdan in the different phases.

An illustration of the geometry between Laurdan and the excitation light is shown in Figure 3.3D. The projection of the probe in the plane of the bilayers is called the c-director, ϕ represents the orientation of the polarized light, φ_c is the angle of the c-director and ρ is the angle between the lipid and the normal of the bilayer. The normal of the bilayer and the direction of propagation for the excitation light are parallel. The intensity of the emitted light depends on the angle between the polarization of the excitation light and the probe molecule. For two-photon excitation it can be described by the relationship below[46].

$$I \propto \sin^4(\rho) \cos^4(\varphi_c - \phi) \quad \text{Eq. 3.1}$$

Careful measurements of fluorescence intensities as a function of linear polarization angles can therefore be used to gain information about the absolute orientation of the probe molecule and thereby the lipids. In the L_α phase the intensity will be indifferent to the orientation of the polarized light, due to the isotropic orientations of Laurdan in this phase, whereas the L_β' phase will have an ordered orientation that can be measured.

There are two reasons why it is an advantage using 2-photon excitation with Laurdan. Firstly the \cos^4 dependency in Eq. 3.1 decreases to a \cos^2 for 1-photon excitation, and secondly the bleaching of Laurdan is more easily controlled in 2-photon excitation.

3.3 Atomic Force Microscopy

Atomic force microscopy (AFM) is a powerful technique for characterizing small structures and objects. It belongs to the class of scanning probe microscopy techniques. The principle is to bring a probe in contact with the sample at a point, thereby determining the height of the sample at the giving point. When the tip is moved across the sample, in a raster scanning fashion, the topographic map of the area is recorded. The AFM offers very good resolution that enables detection and characterization of features that are invisible to light based methods. For a typical AFM the vertical resolution is normally below 1 Å and the lateral resolution in the range of about 1 nm[47].

The setup of a typical AFM is schematized in Figure 3.4. Basically it consists of four components, a piezo crystal, a cantilever, a laser, and a photodiode. The piezo crystal undergoes a size change when an electric field is applied to it, and therefore allows Å precise control of the position cantilever. The contact with the sample will result in a bend of the cantilever. A laser beam reflects of the back of the cantilever, this reflection reaches a photodiode that is divided into four fields. This enables the detection of bends and/or twists of the cantilever, as seen in Figure 3.4. When the cantilever is at rest the laser will hit the center of the diode. Any bend (B) or twist (L) in the cantilever can be measured in a difference between the two halves of the photodiode, specifically given by:

$$B \propto (I_1 + I_4) - (I_2 + I_3) \quad \text{Eq. 3.2}$$

$$L \propto (I_1 + I_2) - (I_3 + I_4) \quad \text{Eq. 3.3}$$

Due to the geometry of the setup the signal, arising from the change of the cantilever position, is magnified greatly when it hits the photodiode, this enables the detection of height differences smaller than 1 Å. [48]

When using AFM there are, at least, two different ways to acquire the topographic image, contact mode and intermediate contact mode (tapping mode). In contact mode the cantilever is kept in contact with the sample during the image scan, i.e. it is dragged across the sample. The AFM will try to maintain a constant force between the sample and the cantilever. Contact mode is a very good for high resolution imaging, but it inflicts a high lateral force on the sample. In intermediate contact mode the cantilever will be oscillated by a second piezo crystal, and any interaction with the sample can be measured as a loss in the amplitude of

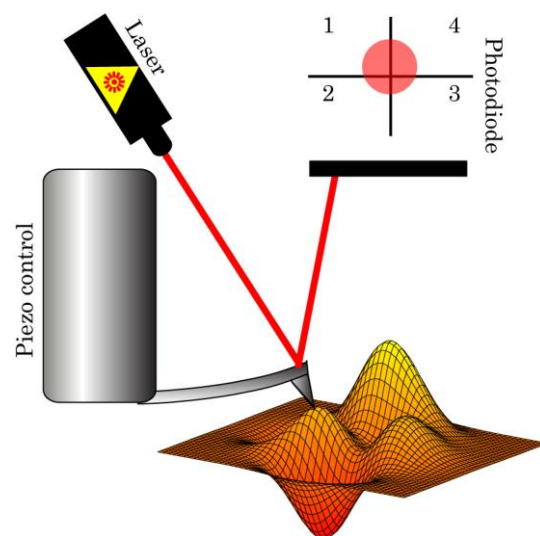


Figure 3.4 The principle in an AFM

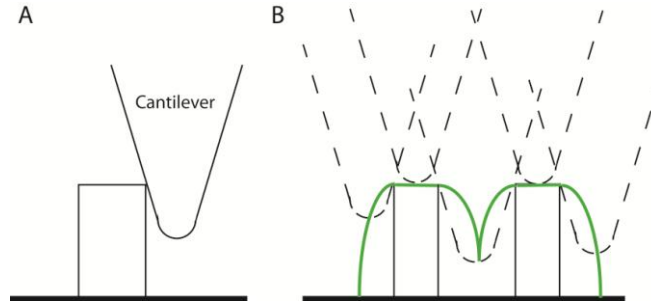


Figure 3.5 A schematic representation of some limitation resulting from the finite size of the cantilever.

the cantilevers oscillation. Intermediate contact mode is less destructive to the sample than the contact mode, and it tends to give better images of tall and narrow objects. However since the entire cantilever holder is vibrating, to induce the oscillation of the cantilever, it can sometime add vibration to soft surfaces in liquid solution.

During an AFM scan other data related to the interaction between the sample and the cantilever is recorded. In contact mode the lateral deflection, i.e. the twist of the cantilever, can be recorded, which contains information about the friction between the sample and the cantilever. In intermediated contact mode a ‘phase image’ can be recorded, which measures the phase difference between the inducing piezo crystal and the oscillating cantilever. This image contains information about the mechanical response of the sample, but can be hard to interpret.

The tip of an AFM cantilever is not infinitely sharp; they typically have a diameter of about 10 nm. If the sample does not have any features sharper than the tip, an AFM image will be an accurate representation of the sample. However if this is not the case, then the tip will not be able to get into contact at every point of the sample, as illustrated in Figure 3.5A. In general an AFM will result in an image with broader features than the sample. However it is not that simple, but depends on the structures that are being scanned. If the features in the sample are the sharper than the cantilever tip the AFM image will be a representation of the tip. The spacing in the sample is also a factor. If the structures are far apart from each other, the height measurement will be accurate, but the AFM images will be broadened.[48] However if they are close to each other the height will also be inaccurate, see Figure 3.5B. There are mathematically ways of subtracting the shape of the cantilever from the image, and thus enhancing the resolution, but it is important to remember that information from places where the tip of the cantilever has not touched the sample cannot be acquired. It is therefore very important to take the expected features of the sample into consideration when interpreting an AFM image.

3.4 Brewster Angle Microscopy

The Brewster angle (θ_b) is defined as the angle at which p-polarized light is transmitted through an interface without any reflection. P-polarized light has an electric field in the plane with the normal to the surface and the incident light, whereas s-polarized light is perpendicular to this plane. The Brewster angle is given by the equation below, where n_1 and n_2 is the refractive index of the incident media and the other media respectively[49], see Figure 3.6.

$$\theta_b = \tan^{-1}\left(\frac{n_2}{n_1}\right) \quad \text{Eq. 3.4}$$

The refractive index of pure water at room temperature is around 1.33, while for air it is 1. Therefore the Brewster angle for an air-water interface is about $\theta_b = 53^\circ$. If the incident light is un-polarized the reflected light will be s-polarized, whereas if the incident light is p-polarized the intensity of the reflected light will be zero.

This however only holds true for a clean air-water interface, if something is on the surface that affects the refractive index at the interface, e.g. a surfactant monolayer, then reflection of p-polarized light might be nonzero. This is utilized in a Brewster angle microscope (BAM). P-polarized light intersects an air-water interface at the Brewster angle, the reflected light is collected and sent through an analyzer (a linear polarizer) and then collected by a camera, as seen in Figure 3.6. If the water surface is clean then no light should be reflected, however in the presence of a surfactant monolayer the reflection is non-zero, and the signal gives an image of the surfactant monolayer. BAM is very sensitive towards inhomogeneity of the monolayer, which for instance has been used to detect the orientation of surfactants on the air-water interface.[50-52]

In BAM the signal arises from a presence of “impurities” on the interface, this means that in theory any compound can be imaged using BAM, and there is no need to add a dye or marker to your sample. Thus BAM is a probe free measurement technique

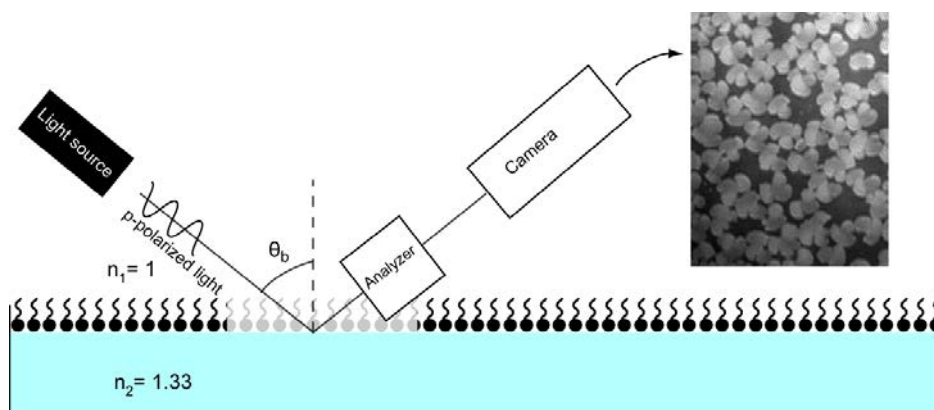


Figure 3.6 Illustration of a BAM setup, p-polarized light reaches the interface at the Brewster angle, in this case 53° . The reflected light is sent through an analyzer and is detected with a camera. The image example is of a monolayer of DOPC, DPPC (1:1) at 20°C at 35 mN/m .

3.5 Fabrication of supported lipid bilayers

There are several methods to create supported lipid bilayer. The three most commonly used are:

1. Transfer of monolayers from an air-water interface either by a Langmuir-Blodgett or Langmuir-Schaefer method.
2. Vesicle fusion
3. Spin coating

The Langmuir-Blodgett and Langmuir-Schaefer method both involve moving the substrate through a monolayer film of the desired lipid spread out on an air-water interface in a Langmuir trough.[21] This offers the advantages of controlling the monolayer composition and packing, individually for each leaflet of the bilayer. Therein lies also its disadvantages, since the two leaflets are decoupled, and the surface pressure of the monolayer will affect the properties of the supported bilayer. GIXD measurement have showed difference, regarding packing and behavior, between bilayer made from Langmuir deposition and vesicle fusion.[31] The Langmuir-Blodgett and Langmuir-Schaefer method will be compared in chapter 6, where the transfer of monolayers to a solid substrate is needed.

Vesicle fusion utilizes the fusion of SUV to the substrate that subsequently spreads out to form the lipid bilayer. This procedure starts by the formation of the SUV, normally through tip sonication, followed by exposing the substrate to the vesicle solution, and finally a thorough rinsing, to avoid excess vesicles attached to the bilayer. There are some limitations to what lipids and substrate can be used, since an attractive force between them is needed. A great advantage of vesicle fusion is the use of SUV containing membrane protein. This allows the formation of support bilayers with imbedded membrane protein.[53, 54]

The method used in this thesis to prepare supported lipid bilayers is spin coating. Spin coating is a technique mostly used for deposition of resist film onto silicon wafers in different types of microfabrication. In this technique a rotational force is used to spread out a film of uniform thickness. It is basically a three step process as outlined in Figure 3.7. Firstly the resist in solution is added to the substrate, after which the substrate starts to rotate. Excess resist is spun off the

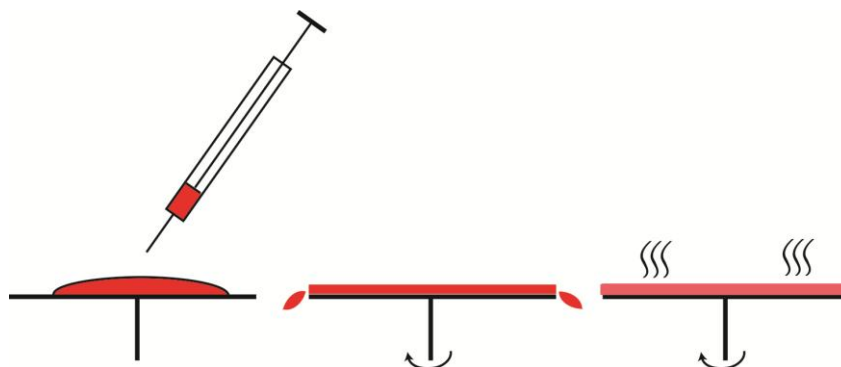


Figure 3.7 The three steps in spin coating. 1. Adding of the solution. 2. Spun off of excess material. 3. Evaporation of solvent.

substrate and the film will become uniformly spread out over the substrate balancing the centripetal and adhesive forces. During the process the solvent will evaporate due to the rotation. In the initial phase of the process the spun off effect will be dominating, while in the last phase only evaporation will occur.[55]

This technique is not limited to resist films. Simonsen et al. and Mennick et al. have demonstrated how spin coating can be used to create supported lipid films of excellent quality.[14, 56] The principles are identical. The desired mixture of lipids is dissolved in an organic solvent, the solution is added to the substrate and followed by the rotation. There are few requirements to the solvent: firstly the desired lipids need to be soluble in it, and secondly the solvent needs to wet the substrate properly. The use of a mixture of hexane and methanol (97:3 by volume) or a mixture of isopropanole, hexane and mQ-water (3:1:1 by volume) works good for most types of lipids and substrate such as mica, silica wafers, glass etc.

After the deposition the sample is stored in vacuum to ensure complete evaporation of the organic solvent. The resulting sample is a stack of bilayers that terminate with a monolayer with the tails exposed to the air. Thereafter the samples can be hydrated in a suitable buffer, and through a careful rinsing process excess bilayer stacks can be removed leaving a single supported lipid bilayer on the substrate. This process is illustrated in Figure 3.8.

Spin coating offers the advantage of easily fabricated support bilayers of a very high quality.[57] Furthermore, there are almost no limitations regarding substrate and it has proven to work for even hydrophobic substrates.[58]

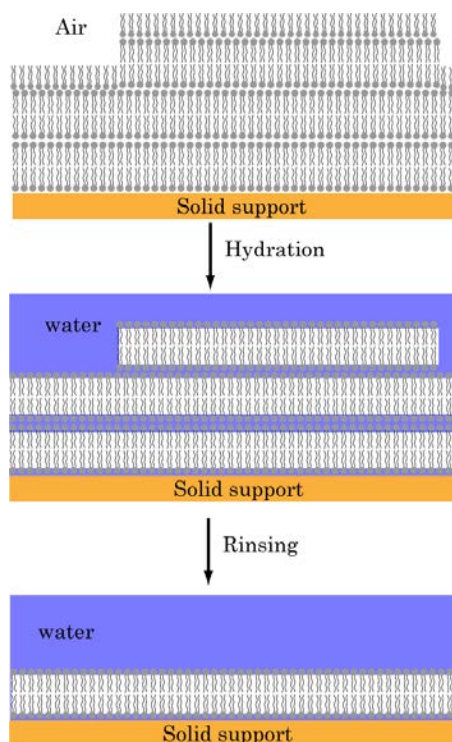


Figure 3.8 A multilayered stack of lipids obtained from spin coating, the top layer exposes the tail to the air. After hydration and rinsing a single bilayer is left at the solid support.

3.6 Procedures, Equipment and Materials

In this section the specific procedures, equipment and materials used in this thesis will be listed.

3.6.1 Supported lipid bilayers by spin coating

Dry spin-coated lipid films on mica were prepared using a stock solution of 10 mM lipid in either isopropanol, hexane, water (3:1:1 volume ratio) or hexane and methanol (97:3 volume ratio), in case of a sample used for fluorescence Laurdan was added 0.5-1% (molar). 30 μ L of the lipid stock was applied to freshly cleaved mica and spun on a Chemat Technology, KW-4A spin-coater at 3000 rpm for 40 s. The sample was placed under vacuum to ensure evaporation of solvents. The spin coated film was hydrated in a commercial fluid cell for microscopy (BioCell, JPK Instruments AG, Berlin, Germany). HEPES buffer (pH=7, c(NaCl)=150mM) was added and the immersed sample was heated to 55°C for 1 h. The sample was subsequently flushed with 80°C buffer using a pipette. Afterwards, the liquid volume was gently exchanged 5–10 times to remove membranes in solution. The sample was then cooled, normally, to 20°C at a rate of 1 °C/min during which domain nucleation and growth takes place. After this the sample is left for 30 min to ensure thermal equilibrium with the microscope. For polarized two-photon microscopy, the sample was placed with the membrane facing the objective to avoid transmission through the birefringent mica substrate.

3.6.2 Atomic Force Microscopy

Atomic force microscopy was performed using a JPK Nanowizard AFM system (JPK Instruments AG, Germany). Contact mode was used for all experiments in this thesis. Used cantilevers:

1. Height measurements of bilayers (chapter 5): triangular typed cantilever (MSCT-AUHW, D-lever, Veeco), with a nominal spring constant of 0.03 N/m and a resonance frequency of 15 kHz.
2. Texture measurement on monolayers (chapter 6): Lateral force cantilever (PPP-LFMR, Nanosensors, Switzerland)

During scanning, the sample was located in the fluid cell described below. The AFM was mounted on top of a fluorescence microscope (Nikon TE2000, inverted) that allowed simultaneous imaging by both techniques, for a full description of this setup see for instance.[59] AFM images were processed and analyzed using the program SPIP (Image Metrology, Denmark).

3.6.3 Polarized 2-photon fluorescence microscopy

Two-photon excitation fluorescence microscopy measurements were done using a custom built microscope, constructed around an Olympus IX70 microscope. The objective used was a 60X water immersion objective with NA=1.2 for all experiments except the measurements on the DOPC,DMPC mixture (chapter 5, Figure 5.3(I)) and the growth experiments (chapter 5, Figure 5.10). The excitation source was a femtosecond Ti:Sa laser (Broadband Mai Tai XF W25 with a 10 W Millennia pump laser, tunable excitation range 710–980 nm, Spectra Physics, Mountain View, CA) and the excitation wavelength used was 780 nm. A half-wave plate was used to control the polarization, where a rotation of 5° of the half-wave plate results in a 10° rotation of the electric field. The emission wavelength of Laurdan is dependent on the membrane phase state and hence the emitted light was collected in two channels using a bandpass filters of 438±12 nm (gel phase) and 494±10 nm (fluid phase) and a dichroic mirror splitting at 475 nm. Detection was done with photo multiplier tubes (PMT) (Hamamatsu H7422P-40).

3.6.4 Monolayer equipments

The monolayers were all fabricated on a NIMA trough with a area of about 800 cm² (KVS-NIMA, Finland), which was fitted with two Teflon barriers, a surface pressure sensor (Wilhelmy plate) and a deposition unit (Langmuir-Blodgett). A custom made clamp was made for the ‘Scooping up’ deposition. The surfactants were spread from a stock solution of 4 mM, the solvent used was chloroform and methanol (4:1 by volume). Substrates used for transfer to solid-air interface were always freshly cleaved mica.

The BAM images were recorded using a EP³-SE Imaging Ellipsometer (Accurion, Germany) set at Brewster conditions. The light source was a solid state laser, 50 mW, $\lambda = 535 \text{ nm}$.

3.6.5 Materials

All chemicals were used as received without further purification. All lipids were ordered from Avanti Polar Lipids, the fluorescence dye Laurdan was ordered from Molecular probes/Invitrogen, and all other chemicals and solvents were from Sigma-Aldrich and of a HPLC grade quality. All water used in this work was ultrapure mQ-water (18.3 M Ω · cm).

Lipids:

- 1,2-dilauroyl-sn-glycero-3-phosphocholine (DLPC)
- 1,2-dimyristoyl-sn-glycero-3-phosphocholine (DMPC)
- 1,2-dipalmitoyl-sn-glycero-3-phosphocholine (DPPC)
- 1,2-distearoyl-sn-glycero-3-phosphocholine (DSPC)
- 1,2-dioleoyl-sn-glycero-3-phosphocholine (DOPC)

- 1-palmitoyl-2-oleoyl-sn-glycero-3-phosphocholine (POPC)
- N-stearoyl-D-*erythro*-sphingosylphosphorylcholine (SM-C₁₈)

Fluorescence Probes:

- 6-Dodecanoyl-2-Dimethylaminonaphthalene (Laurdan)
- 1,1'-dioctadecyl-3,3,3',3'-tetramethylindocarbocyanine (DiI)

Buffer: The HEPES buffer, pH =7, ionic strength 150 mM, was made by adding the appropriate mixture of the acidic, basic component and NaCl. The pH was subsequently checked, and if necessary adjusted.

Chapter 4

Orientalional Texture and Defects in DOPC DPPC Bilayers

Model membrane studies are typically focused on the membrane phase state, domain sizes, and lipid composition. Only recently has it become clear that certain condensed membrane phases are not homogeneous, but may have orientational texture.[60] Such texture arises if the lipid acyl chains are tilted with respect to the bilayer normal. This tilt can of course not be random due to the order of the phase it is associated with, and therefore in the $L_{\beta'}$ membrane phase there may exist a hexatic, long-range positional orientational order which couples to the lipid tilt orientation. This enables the system to sustain texture patterns with long-range order in the orientation angle visible in optical microscopy. Bernchou et al. measured that despite the internal anisotropic structures of the $L_{\beta'}$ domains their thermodynamic phase state was shown, by Laurdan GP measurements, to be uniform.[16]

Langmuir monolayers have long been known to display texture and topological defects, and hence the existence of texture in lipid bilayers should not be surprising. These are in many aspects similar to textures initially found in liquid crystals.[61, 62] Thin films of smectic- C (Sm-C) liquid crystals can be drawn over an opening in a microscope slide and may display orientational textures when observed using depolarized reflected light microscopy.[63-65] This system of stacked layers can in some aspects be compared to lipid bilayers and, therefore similar texture patterns should be possible in a lipid bilayer system. Topological defects observed in Sm-C systems include integer and fractional vortices as well as string defects and combinations thereof. An important difference from monolayer and bilayer domain texture is that domains in these systems are formed through nucleation and growth and have a finite size and a boundary to a surrounding isotropic phase. This means that boundary conditions and details of the nucleation and growth may influence the final texture.

Microscopy of coexisting LE and LC domains in Langmuir monolayers has been performed for decades. The early studies of texture in Langmuir monolayer LC domains were primarily done using BAM[34, 51, 66-69] and polarized fluorescence microscopy.[70-74] Combined with X-ray diffraction data and compression isotherms, a detailed picture of domains and domain textures has been established in monolayers.[22, 24, 25] As shown in chapter 2.4 the texture can

be modeled by Landau-type free energy models[20] which allow classification of textures and defects.

X-ray diffraction applied to Langmuir monolayers was initiated by Kjaer et al.[75] demonstrating that some LC phases had hexatic order. Many LC phases have since been shown to be hexatic[25] while some phases are 2D crystals. The hexatic phase has been described previously in chapter 2.3-4. Results using GIXD on bilayer samples have established a link between hexatic order and texture in gel phase membranes and further proved that texture can be influenced by biomolecular binding events.[31, 76, 77]

In this chapter we present a complementary technique to detect the long-range orientational order in lipid bilayers using polarized two-photon microscopy. The orientational texture will be recorded for $L_{\beta'}$ domains in a DOPC,DPPC (1:1) bilayer. This chapter will describe the different measurements and calculation in details. It will start by a brief summary of the experimental setup (Section 4.1). In Section 4.2 we will describe how the orientational texture was recorded and to present it to allow investigate of the texture. This will be followed by analyses of the variations of orientations within the domains (Section 4.3). Defect structures can be revealed by calculating the gradient of the orientation (Section 4.4), which include a set of central point defects (Section 4.5) Lastly the possible effect of the support will be investigated (Section 4.6). In the discussion (Section 4.7) the different results will be compared.

4.1 Experimental Setup

The experimental setup was described in chapter 3, but to avoid any misunderstanding regarding the content of the sample, and its preparation, this section will give a very short summary of the sample preparation.

The supported lipid bilayers were fabricated using spin coating, onto a mica substrate. After the spin coating the dry lipid film was submerged in HEPES buffer (pH=7) in a fluid cell that allowed control of the temperature. The sample was heated to about 50°C for 1 hour, followed by a rinsing in hot (80°C) HEPES buffer. The rinsing removes excess bilayers leaving only the bilayer on top of the mica. Afterwards the sample is cooled down to 20°C at about 1°C/min. During the

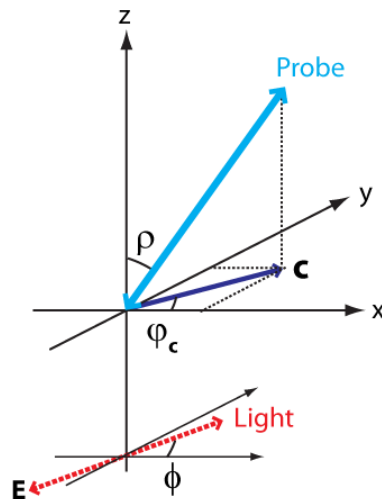


Figure 4.1 Schematic explanation of the experiment in an xyz frame of reference. Top view shows the tilted Laurdan probe which is embedded in the bilayer and bottom shows the E-field of the polarized excitation light. The projection of the probe into the plane of the bilayer is called the c-director (D).

cooling process domains in the L_{β} phase will be formed. After the cooling the sample was turned up-side-down, to avoid having mica in the optical pathway of the microscope. After those steps the sample was ready to be measured in the polarized 2-photon microscope.

As mentioned in Chapter 3.2, the fluorescence probe Laurdan is sensitive towards the polarization of the light. A few notations regarding Laurdan, the bilayers and the polarized light is shown in Figure 3.3. The projection of the probe into the plane of the bilayer is called the c-director, which is what we measure with the polarized light. The c-director will be referred to as the orientation of the lipids, and the orientational texture is the variation of the c-director across the entire domain. ϕ represents the orientation of the polarized light, ϕ_c is the angle of the c-director and ρ is the angle between the lipid and the normal of the bilayer. The normal of the bilayer and the direction of propagation for the excitation light are parallel.

4.2 Measuring the Orientation

The L_{β} domains of the DOPC,DPPC mixture are imaged by recording a scan of different polarization angles of the same area. A polarization scan typically consists of a stack of 36 fluorescence images covering a 2π rotation. Two of those images are shown in Figure 4.2AB, where the polarization is marked by a white arrow. As the polarization is rotated different subparts of the domain light up, while others go dark. Three regions have been marked in Figure 4.2C where the intensity, as a function of the polarization, is plotted in Figure 4.2D. The intensity has a periodic dependence on the polarization, and the three different areas have a different peak position, corresponding to different angles of orientation within each area. To analyze the fluorescence images we implemented a series of Matlab GUI's. The intensity of a single pixel in row m and column n is given by I_k^{mn} , where k gives the angle increment.

$$I_k^{mn} = I^{mn}(\phi_k) = I^{mn}(\phi_{offset} + rot \cdot k \cdot \Delta\phi) \quad \text{Eq. 4.1}$$

The three parameters ϕ_{offset} , rot , and $\Delta\phi$ are instrumental constants defined by the microscope setup. They represent: the orientation of the polarization in the first image, the direction of the polarized lights rotation (-1 clockwise,+1 counter clockwise) and the (numeric) angle difference between each image respectively. The values for these parameters were determined experimentally and found to be: 15° , -1 and 10° respectively.

One problem regarding working with polarized light is the possibility for the optical components to have non-ideal properties. This can result in the intensities being dependent on the orientation of the polarized light. This problem was solved by normalizing the intensities to an isotropic region of the image, i.e. the L_{α} phase. The normalization to the isotropic phase also ensures that the intensities are independent of laurdan concentration, as long as bleaching is negated. The

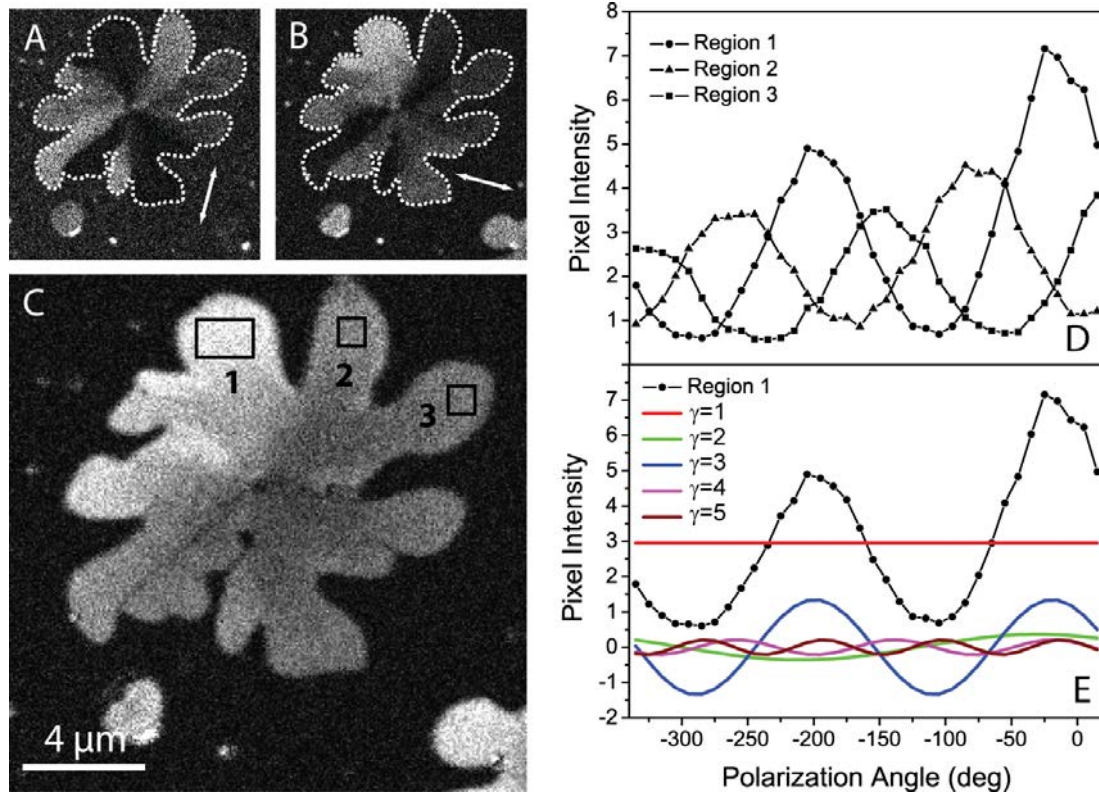


Figure 4.2 Selected fluorescence images (A,B) from a polarization scan sequence of 36 images of a supported bilayer with composition DOPC,DPPC (1:1). The direction of polarization is indicated with white arrows. The director length image L^{mn} is shown in (C) and has been used for the segmentation of the L_E domain as indicated with the dotted white line in (A,B). The variation of the average emission intensity in regions 1,2, and 3 (C) with respect to polarization angle is shown in (D). The phase shifts of the harmonic variation originate from the difference in director orientation within these regions. Fourier decomposition of the signal from region 1 is shown in (E). The mode $\gamma = 3$ is used to determine the orientation texture.

correction is small and normally well below 5 percent. Let ROI, be the coordinates to an isotropic region, then the corrected pixel intensity is given by:

$$I_k^{mn}(\text{corrected}) = \frac{I_k^{mn}}{\langle I_k^{mn} \rangle_{ROI}} \quad \text{Eq. 4.2}$$

The orientation of the molecular director (c) in each pixel is obtained from the discrete fast Fourier transform:

$$\tilde{I}_k^{mn} = \sum_{k=1}^N I_k^{mn}(\text{corrected}) \cdot e^{-\frac{i2\pi}{N}(\gamma-1)(k-1)} \quad \text{Eq. 4.3}$$

The intensity for a single tilted fluorescence probe completes two harmonic periods during a rotation from 0 to 2π . This harmonic variation is obtain from the Fourier mode \tilde{I}_3^{mn} . Other contributions to the signal, e.g. noise etc., are located in Fourier modes with $\gamma \neq 3$.

$$L^{mn} = |\tilde{I}_3^{mn}| \quad \text{Eq. 4.4}$$

Here the modulus, L , defines the director length, corresponding to the strength of the angular responds, which is related to the length of the c director. The angle of the c -director, φ_c , is obtained through the argument:

$$\varphi_c^{mn} = -\frac{1}{2} \cdot rot \cdot \arg[\tilde{I}_3^{mn}] + \phi_{offset} \quad \text{Eq. 4.5}$$

The interval for the director angle will thus be:

$$\left[-\frac{\pi}{2} + \phi_{offset}, \frac{\pi}{2} + \phi_{offset} \right] \quad \text{Eq. 4.6}$$

The limitation of the interval to π , instead of 2π , is due to the symmetry of the polarized light, since there is no difference in the polarized light for a rotation of π . The harmonic variations of the pixel intensity are shown in Figure 4.2C-D. The phase shift between the three regions is due to a difference in the molecular orientation, i.e. the c -director of the fluorescence probe. The scan is recorded right to left (since $rot = -1$ in Eq. 4.1), and a small photo bleaching can be observed as a decrease in the second peak of each scan. The different Fourier mode for region one is shown in Figure 4.2E, it is clearly evident that the two major contributors to the signal are the invariant $\gamma = 0$ and the $\gamma = 3$ used to calculate the orientation.

For each pixel the orientation of the lipids, φ_c , and the strength of the signal, L , which have been compiled from the image stack of 36 images, is acquired. The orientation is converted to a color and the strength to brightness/hue. The color scheme can be seen in insert in Figure 4.3E, and the resulting image can be seen in Figure 4.3A-E. The orientation is also marked by lines averaged over 8 by 8 pixels, where the length is proportional to the c -director length. Several things can be noticed in these images. The orientation is not uniform across the domain and there is a clear division of the domains into sub domains, each with a preferred orientation within. A closer look at the outer part of the domain reveals, that the change of orientation going from one sub domain to another is confined to a thin line, called a defect line, as seen in Figure 4.3F+G. The defect lines can be divided into two different pure types: splay or bend defect. Figure 4.3F shows a splay defect where the c -director is aligned parallel with the defect line, whereas Figure 4.3G shows a bend defect where the c -director is perpendicular to the defect line. Other defect lines can be observed in Figure 4.3E that display a mixture of splay and bend. Unlike the monolayer cases, discussed in chapter 2.4, where one type of defect dominates the texture, a mixture of defect types within the same domain is observed.

When taking a closer look at the central region of the domain, as seen in the zoom in Figure 4.3H, the defect line is no longer observed. Instead a continuously change of orientation, converging into a vortex like structure towards the nucleation point in the center is seen. We will later, in section 4.5 below, go into further details about the texture observed at the center of the domain.

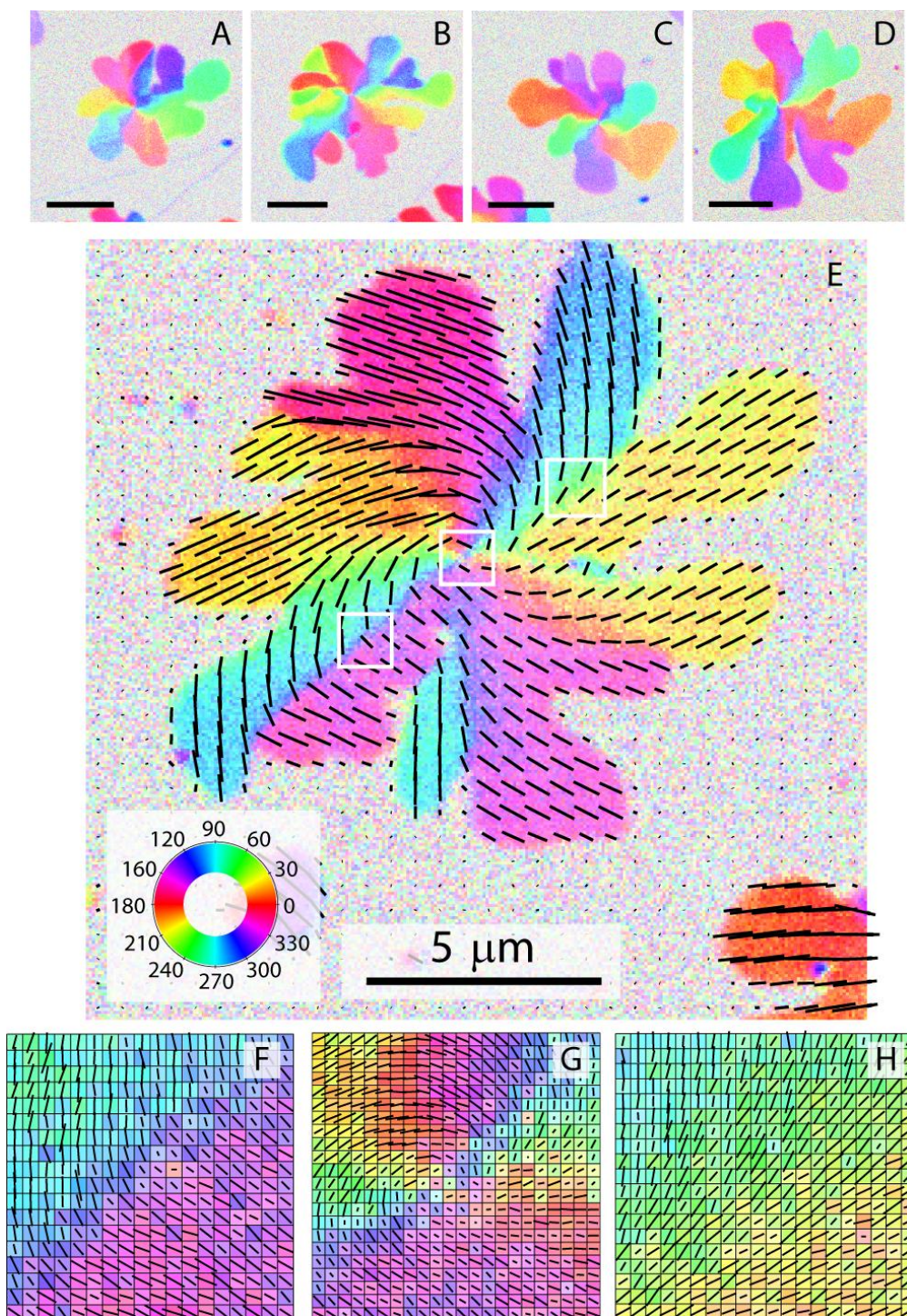


Figure 4.3 Examples of textures in gel domains (DOPC,DPPC, 1:1) (A–E). The orientation angle φ_c of the molecular director is represented by colors as in the legend (E). Image (E) shows black lines representing the directors, averaged over 8×8 pixel regions of the image. The length of each line is proportional to the director length L while the orientation is given by φ_c . Magnified textures (F,G,H) are resolved at the level of single pixels in the indicated regions of image (E). (G) shows a line with almost pure bend deformations, while (H) shows an example of a defect line with almost pure splay deformations. Other line defects in the domain may have mixed splay/bend character.

4.3 Internal Distribution of Orientations

In order to further analyze the domains they need to be separated from the L_α surrounding in the images. This was done in a simple fashion by plotting the director length, L , and converting it into a binary image using a cutoff value. The cutoff values were found visually using a manual sliding value, but could easily have been determined using a histogram. Figure 4.2C is an example of a plot of the director lengths, and the domain is clearly defined by the brightness. By using this it is possible to get the coordinates for each pixel inside the domain the perimeter. In Figure 4.2 the perimeter of the domain has been found and plotted in A and B.

By using the segmented domain, the orientations within the domain is plotted as a histogram. This permits a closer inspection of the distribution of angles within the domain. The result can be seen in Figure 4.4A, where three peaks are observable, as is typical for most domains. The orientation-histogram is fitted to a sum of three Gaussians and intervals representing the mean ± 1 standard deviation were colored red, green and blue. These distributions were used to recolor the image, where each pixel in the domain, having an orientation within one of the three values, were colored correspondingly. All other pixels were left black, as seen in Figure 4.4B. The three dominating angles are: 22° (red), 25° (green), and 95° (blue) and it is seen that these angle intervals account for most of the domain area. The dominating angles are clearly represented by separate regions and not mixed. The typical pattern is each color is located in two oppositely placed subdomains. Such two opposite subdomains will actually have parallel, but oppositely oriented directors, which cannot be discriminated here. Thus the 3 different angles in the

orientation-histogram correspond to 6 different physical orientations in the domain. From the peaks in Figure 4.4A the angle difference between neighboring subdomains is found. The measured values are: red-to-green = 47° , green-to-blue = 70° and blue-to-red = 63° . These values differ from the expected 60° present in an even 6-fold distribution of the orientations which none of the domains have been observed to have. The change in orientation is not always confined to the line between subdomains. In some regions of Figure 4.4B and Figure 4.4D, a black area between

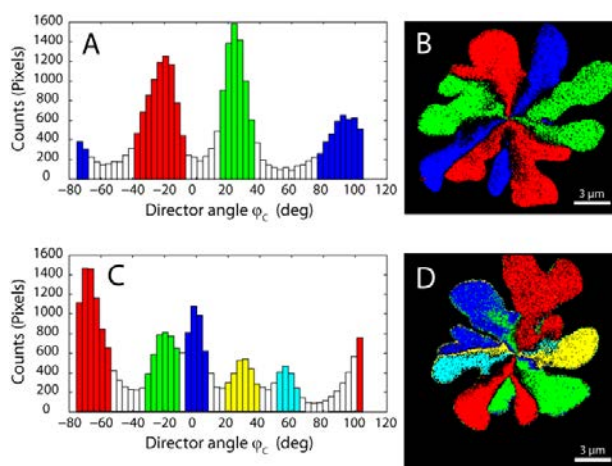


Figure 4.4 Histogram of the director angles within L_β domain (A). Three peaks are present corresponding to three (six) dominating orientations of the director in the domain. The peaks are fitted to a sum of three Gaussians to obtain mean (μ) and standard deviation (σ) for each peak. The red/green/blue bars are the intervals: $\mu \pm \sigma$. The pixels having values of φ_c within these intervals are shown in (B). An equivalent representation of a domain where 5 angles are discernible in the histogram (C,D).

subdomains indicates a gradual transition rather than a line defect, such as in the blue (left) and green (left) subdomains of Figure 4.4B. The majority of domains analyzed have 3 dominating orientations located in 6 subdomains, but a higher number of distinct orientations are sometimes observed. This occurs when the c-directors in two opposing subdomains are not completely parallel and therefore split into two peaks in the orientation-histogram. The example in Figure 4.4C, shows 5 peaks with positions 67° (red), 19° (green), 0° (blue), 29° (yellow) and 56° (cyan) and the corresponding color image in Figure 4.4D. In this example, 2 out of 3 angle peaks has split and created the pairs blue-green and yellow-cyan. Note, that the red peak is representing 2 opposite orientations in the domain such that there are still 6 physical orientations in the domain like in the previous domain of Figure 4.4B.

4.4 Defect Structures

By calculating the gradient of the orientation, $\nabla\varphi_c$, it is possible to investigate defect structures in the domains, which are identified by having a large gradient of the orientation. The gradient is related to the energy density of the texture. In order to calculate the gradient we need to smooth the data due to noise. We used a box average, where each pixel is defined by the average value of a S by S box (typical S = 3-5). We smoothed the Fourier component ($\gamma = 3$), and the smoothed director lengths and orientation were then calculated from the smoothed Fourier component.

$$\tilde{l}_3^{mn}(\text{smoothed}) = \langle \tilde{l}_3^{mn} \rangle_{sxs} \quad \text{Eq. 4.7}$$

The gradients were calculated numerical from the values of neighboring pixels, independently for the x and y components:

$$\nabla\varphi_c = (FX, FY) \quad \text{Eq. 4.8}$$

$$FX = \frac{\delta\varphi_c}{\delta x} |_{mn} \frac{1}{2} [\varphi_{c,\text{smoothed}}^{m,n+1} - \varphi_{c,\text{smoothed}}^{m,n-1}] \quad \text{Eq. 4.9}$$

$$FY = \frac{\delta\varphi_c}{\delta y} |_{mn} \frac{1}{2} [\varphi_{c,\text{smoothed}}^{m+1,n} - \varphi_{c,\text{smoothed}}^{m-1,n}] \quad \text{Eq. 4.10}$$

Due to the interval of the orientation and the symmetry thereof, as defined by Eq. 4.6, differences in director angles by more than $\pm\frac{\pi}{2}$ and therefore gradients larger than $\pm\frac{\pi}{4}$ are not resolved. In order to ensure this, values that were outside that range were brought into the range by $\pm\frac{\pi}{2}$. The gradient was only calculated on the segmented domain in order to avoid the noise from the random fluctuations in the isotropic L_α phase. The gradient calculated for a domain can be seen in Figure 4.5B, where a bright pixel represent a large change of orientation.

From the gradient image it is clear that there are two different areas within the domain that need further inspection: The center of the domain, and the defect

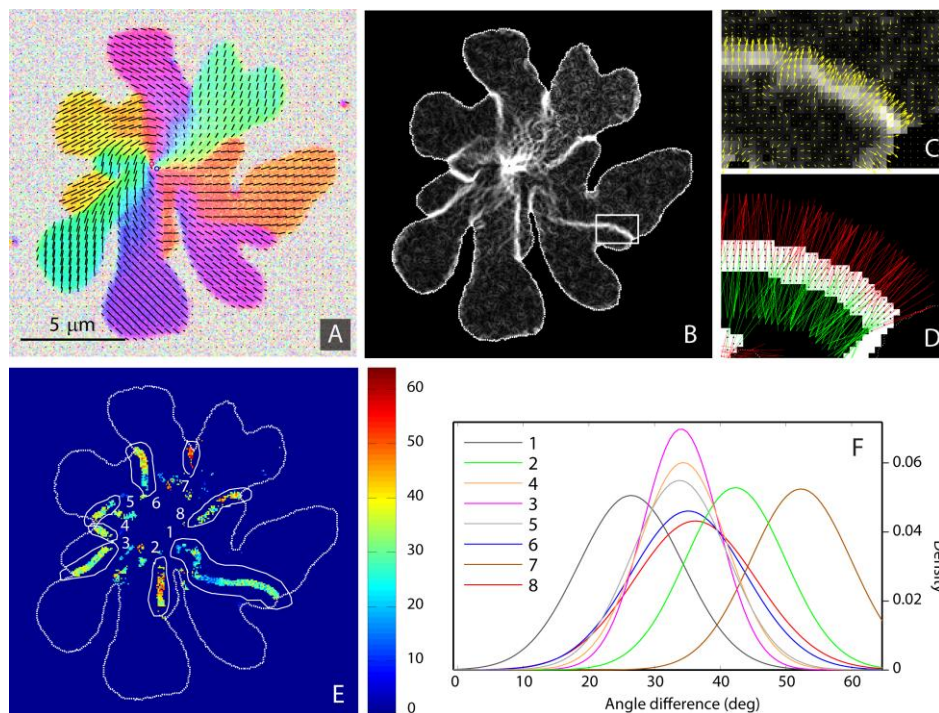


Figure 4.5 Analysis of jump-angles associated with line defects in the texture pattern. The domain texture (A) is analyzed by numerically computing the gradient $\nabla\varphi_c$ which is visualized as the gradient norm $|\nabla\varphi_c|$ shown in (B). The rectangle in (B) indicates the region of the zoom (C) of the gradient image. Yellow arrows show the gradient vectors at the single pixel level. The change in director angle (jump-angle) across a line defect is computed by examining the extension of the gradient from the boundary pixels. Image (D) illustrates this construction (write new here). The jump-angles for individual pixels on the line defects are shown as color coded pixels in image (E). The units of the color bar are degrees and all pixels not belonging to line defects are void (dark blue). Gaussian fits (F) to the distribution of jump-angles in 8 selected line defects as indicated by the outlined regions in (E). The distributions in (F) illustrate the typical variation in jump-angles among the line defects of a single domain.

lines. The defect lines become evident as bright lines in the gradient image, clearly indicating the change of orientation happening at a very confined line. Between the defect lines in the perimeter a dark area meaning no changes of orientation occur can be observed. The defect lines are disconnected from the center of the domain, and in the center we see a brighter region, again matching well with the previously described continuously change of orientation in the center region. In section 4.5 a closer inspection of the central defect will be presented. To examine the defect lines in the perimeter of the domain., the jump-angle, which is the change of orientation going across a defect line has to be investigated. The jump angles are determined locally for each pixel on a defect line. This allows the mapping of the spatial variations within a single line. The procedure involved the following 6 steps, illustrated in the Figure 4.5C-F:

1. Pixels belonging to a defect line are identified by segmenting the $|\nabla\varphi_c|$ image, using a cutoff value.
2. For pixels within a defect line, an extension of the gradient vector is drawn to both sides of the defect, as shown C and D. The length of the extension is set

manually. The jump-angles are not very sensitive to the extension length, since the orientation is quite uniform inside a subdomain.

3. Any extension which either fall outside the domain or inside a defect region are removed.
4. The absolute difference between the orientation at the forward and backward extension is recorded as the jump-angle for that pixel. Only jump-angles $< \frac{\pi}{2}$ are allowed as previously discussed.
5. A map of the jump-angles is created, where the color represent a jump-angle as seen in E and its legend.
6. Individual defect lines are manually marked and jump-angle distribution is recorded and marked in F.

A closer look at Figure 4.5E reveals a significant variation of the jump-angles both between line defects, but also within a single line defect. There is a small trend that some of the line defects have smaller jump-angles closer towards the center, whereas the opposite trend is not observed. By looking at the distribution of the different jump-angles within a line defect, as seen in Figure 4.5F, it is seen that all jump-angles are significant below the 60° that would have been expected from an evenly distribution of 6 subdomain.

It can be interesting to compare this result with the distribution of orientations as described in section 4.3. In Figure 4.6 the orientation histogram and recoloring of the domain, used in Figure 4.5, is shown. A comparison between

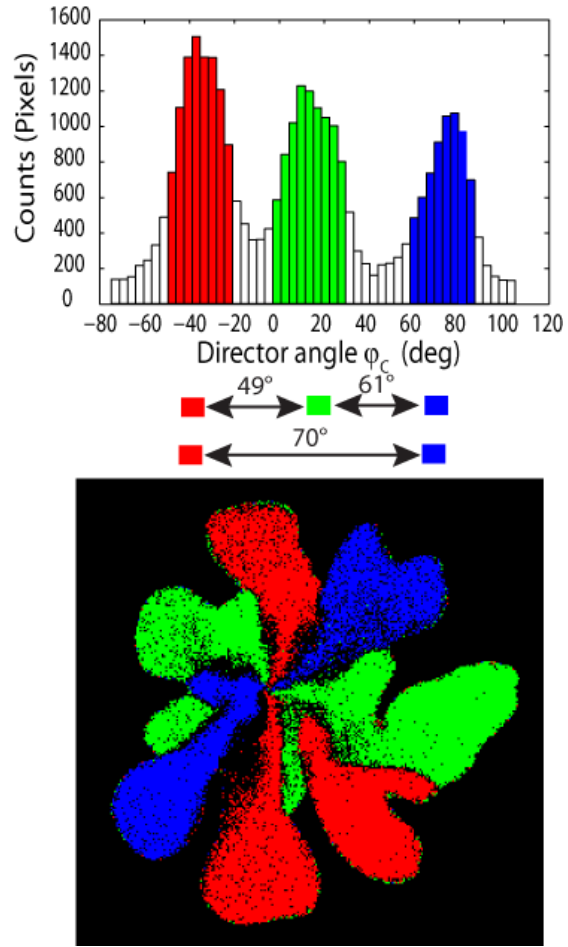


Figure 4.6 Histogram analysis of the domain used to calculate the jump angle in Figure 4.5. The angle difference between the three peaks are shown in the middle.

Defect line ^I	1	2	3	4	5	6	7	8
Jump-angle ^I	25°	40°	35°	35°	35°	35°	55°	35°
Histogram angle ^{II}	49°	49°	61°	61°	61°	49°	70°	61°

Table 4.1 A comparison between the jump-angle and the angle difference between the histogram analysis of the orientations.

I) Data taken from Figure 4.5

II) Data taken from Figure 4.6

the jump angles, and the angles obtained from the peaks positions in the orientation histogram is shown in Table 4.1. The jump angle yields a lower value in general, but it is important to notice the difference between the two methods. The jump-angle is, as mentioned above, calculated from the value just besides the defect line whereas the orientation histogram angle is taken from the two mean values within the subdomain. The jump-angles therefore come closer to a true value of the orientation change going across a defect line, whereas the other describes the difference between the mean orientations in neighboring subdomains. The large difference between the two values could indicate a change of orientation when going across a subdomain.

4.5 Central Point Defect

As earlier mentioned the central part of the domain exhibit a continuous change of angle in a vortex like structure. A closer look at the gradient in the center region is shown in a zoom in Figure 4.7A. It is clear that the center region actually consists of two closely spaced point defects. Such paired defects are present in all observable domains with this lipid composition. Some domains have bound vesicles at the domain center which obscures precise characterization of the defect pair for these domains. From the previous inspection of the texture pattern it shows that the central defect is of index $|m| = 1$ in the far field, such that the splitting generates two $|m| = \frac{1}{2}$ point disclinations. Pairs of $|m| = \frac{1}{2}$ point disclination must theoretically be connected by a defect line that separates regions with opposite orientations of the directors. By fitting a 2D Gaussian peak to each point disclination it was possible to measure the distance and angle between the two, as indicated by the line in Figure 4.7A insert. The location of defect pairs in 10 L_{β} domains is shown in Figure 4.7B, where the defect pairs have been translated to the same center of mass, to enable a comparison. Both the separation and orientation of pairs fluctuate between the

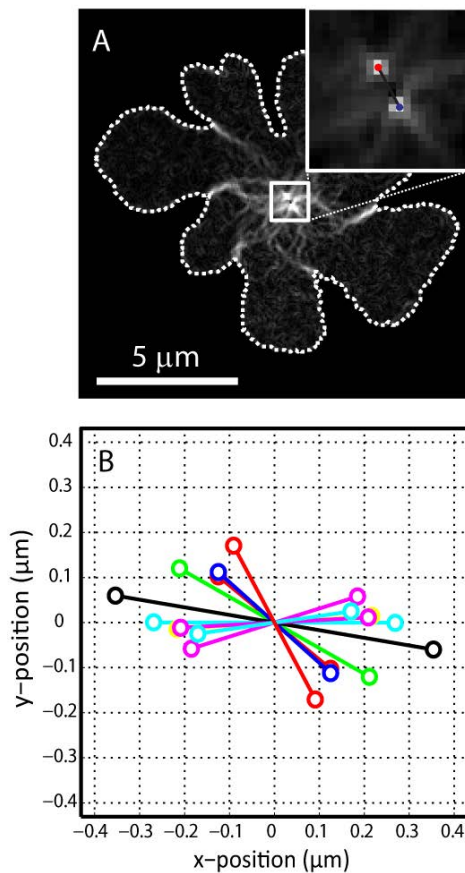


Figure 4.7 Detection of point disclination pairs in L_{β} domains. The gradient norm image $|\nabla\phi_c|$ in (A) shows a large magnitude of the gradient (bright) in the domain center. A zoom (insert) of the texture in this region reveals two closely spaced point defects whose positions are detected by fitting 2D Gaussian peaks to the gradient norm. The resulting positions are the red and blue point (insert). Plot in (B) shows defect pair locations for 10 L_{β} domains where all defect pairs have been translated to the same center of mass to enable comparison.

domains, thereby removing the possibility that the pair of point defect is an artifact of either the substrate (mica) or the analysis process.

We would like to investigate the nature of this vortex texture in the center of the domains. Watkins et al.[77] derived the formulation for a model of a single point disclination of index m given by the expression:

$$\varphi_s(x, y) = m \cdot \tan^{-1} \left(\frac{y}{x} \right) + \varphi_{s0} \quad \text{Eq. 4.11}$$

Where x, y is the lateral position, φ_s the simulated texture and φ_{s0} is an offset that determines whether the texture has splay or bend character. Pure splay is described by $\varphi_{s0} = 0, \pi$, and pure bend by $\varphi_{s0} = \pm \frac{\pi}{2}$. For a $m = 1$ point disclination the resulting orientational texture for pure bend, pure splay and a mixed is shown in Figure 4.8, first row. A pair of $m = \frac{1}{2}$ point disclinations were modelled to our experimental data by an extension of Eq. 4.11, where the two defect points are located at $(x_1, y_1), (x_2, y_2)$.

$$\varphi_s(x, y) = \frac{1}{2} \cdot \tan^{-1} \left(\frac{y - y_1}{x - x_1} \right) + \frac{1}{2} \cdot \tan^{-1} \left(\frac{y - y_2}{x - x_2} \right) + \varphi_{s0} \quad \text{Eq. 4.12}$$

Bend, splay and mixed for the two point disclinations are showed in Figure 4.8, second row. It is evident that the two $|m| = \frac{1}{2}$ point disclinations resemble a $|m| = 1$ seen from the far field as expected.

By comparing this simulated texture with the texture observed for the domains, it would be possible to determine the offset value and thereby the bend and/or splay character of the texture. Hopefully this would also tell whether the offset were a constant for the mixture or varying between domains. The texture in

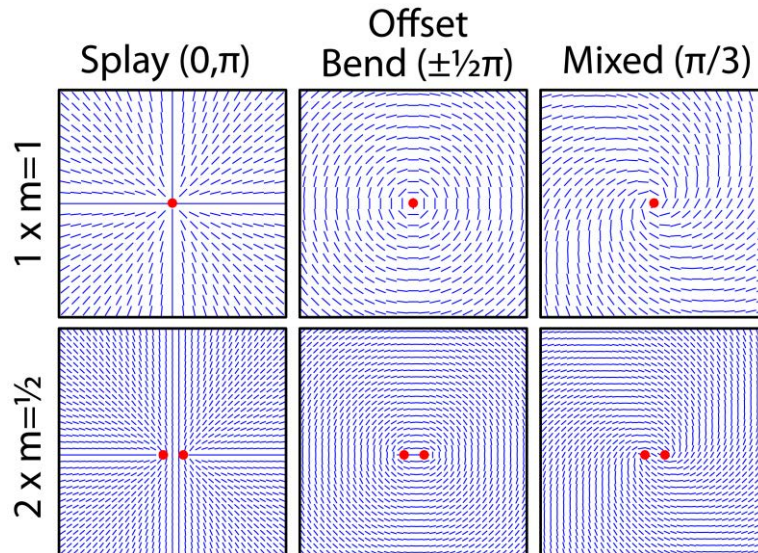


Figure 4.8 Examples of the simulated textures defined by Eq. 4.11 (top row, on point defect) and Eq. 4.12 (bottom row, two point defect). The illustrate textures of either pure splay (left), pure bend (middle) or a mixture of those two (right).

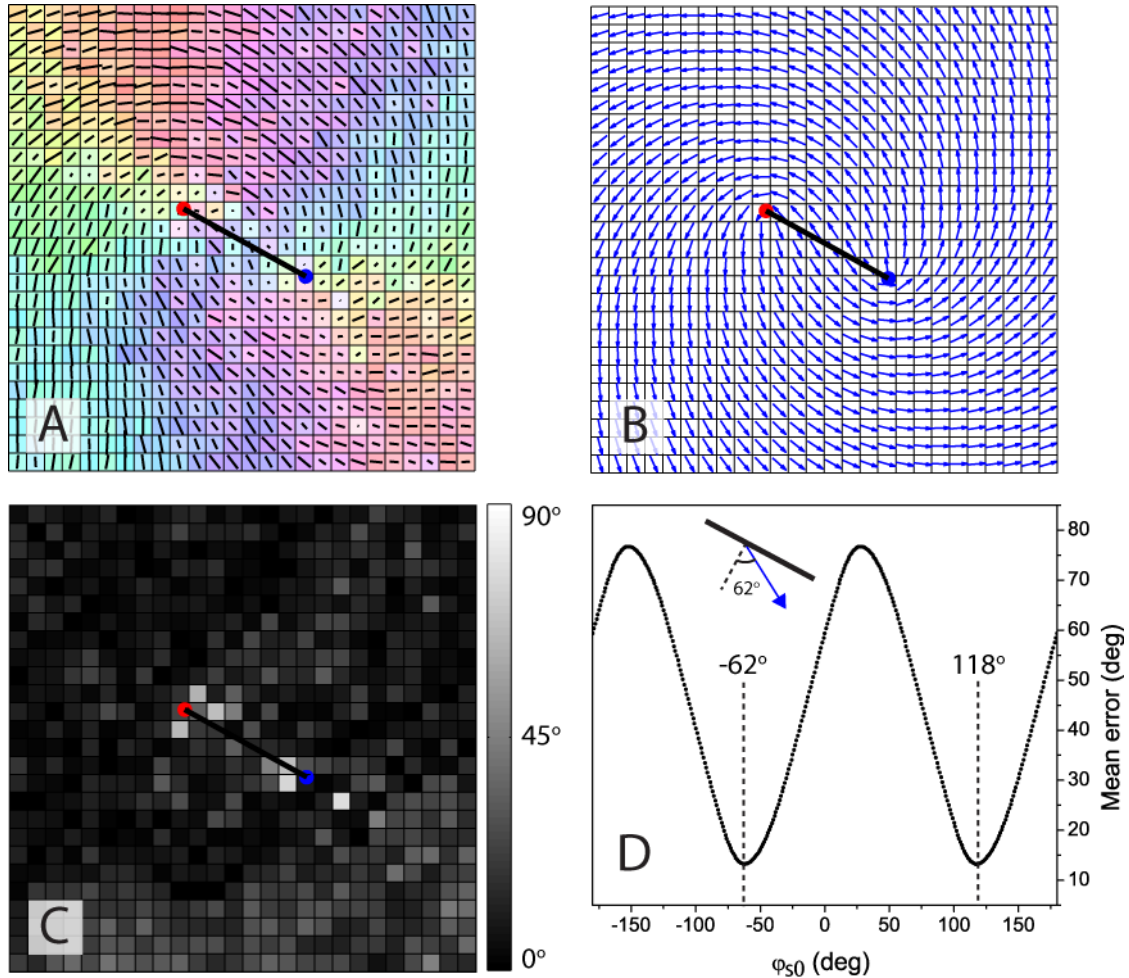


Figure 4.9 Analysis of defect pairs. Image (A) shows the measured texture in the vicinity of a pair of $m=1/2$ point disclinations in the center of a domain. The positions of the defects (red, blue points) were determined as in Figure 4.7. A simulated texture pattern (B) that was fitted to the measurement in (A) using Eq. 4.12. The simulation has two $m = 1/2$ defects at the experimentally measured positions and the offset φ_{s0} was fitted. There is an equivalent simulated texture with $\varphi_{s0}+180^\circ$ (not shown). An error map (C) showing the difference between measured and simulated director angles. Plot of the average difference between measured and simulated texture (D) showing the two equivalent minima. Insert (D) shows how the detected value of φ_{s0} relates to the director orientation on the defect line in (B). (Image size (A–C) is 1.6 by $1.6 \mu\text{m}^2$).

the center of a domain is shown in Figure 4.9A along with the detected pair of $|m| = \frac{1}{2}$ point disclinations. In this central region, the texture is continuous and does not exhibit line defects. Hence it is possible to model it by an expression of the form in Eq. 4.12. Keeping the detected defect positions fixed, makes the offset angle φ_{s0} , the only fitting parameter. The simulated texture best representing the data is shown in Figure 4.9B. Note that two equivalent textures, differ only by a rotation of the director by π , and will match the experimental data equally well. The error map in Figure 4.9C shows the pixel-by-pixel difference between measurement and simulation. It indicates good overall agreement across the simulated region. The average angle difference between model and experiment has been plotted against φ_{s0} in Figure 4.9D, highlighting the two minima where the simulation matches the

experiment. The experimental value for the offset averaged over 10 domains is $\varphi_{s0} = 60.5^\circ \pm 6.5^\circ$, where the deviation is plus/minus one standard deviation. Firstly this tells us the value is relatively constant within the mixture, and therefore is related to the lipid composition. Secondly it tells us that the sample has a mixture of bend and splay character, which again matches well with the observation done earlier about a spiral vortex like structure in the center and the observation of both types of line defects.

4.6 Effect of Substrate

Mica have been used as support for all the lipid bilayer in this thesis. It has a crystalline structure with ordered direction, and it is therefore relevant to wonder whether the observed orientational textures are induced or affected by the mica substrate. If the crystalline directions of mica have an effect on the orientational texture, the observed patterned would be expected to be regularly shaped. If comparing the different texture images presented, i.e. Figure 4.3A-E, this is clearly not the case. It is not a preferred set of angles that are repeatedly observed for different domains. Therefore the directions in the crystalline mica are not expected to have an effect. There could however still be some effect of the forces between the bilayer and the substrate.

This could in principle be investigated in two different systems of model membranes: GUV or planar lipid bilayer shielded from the substrate, e.g. by another bilayer.

The use of GUV offers the advantage of completely decoupling from a substrate. It does however introduce a curvature, which would further complicate the analysis of the data. Therefore the second approach with a shielded bilayer was tested. This is illustrated in Figure 4.10D, where the second bilayer is effectively shielded from the substrate by the first bilayer. This investigation was made on a bilayer of DOPC and Sphingomyeline C₁₈ (SM-C₁₈)(1:1 mixuter), which means the

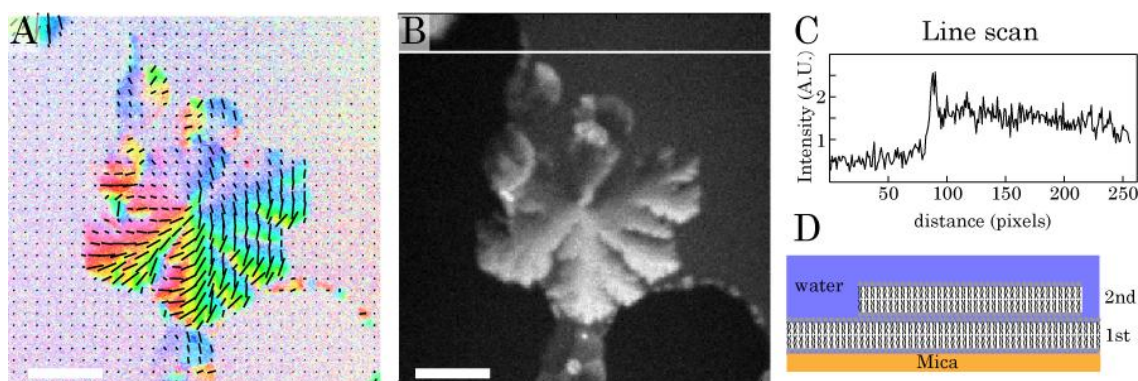


Figure 4.10 Images of a $L_{\beta'}$ domain in a DOPC: Sphingomyeline C₁₈ (1:1) bilayer located in the second level of bilayer (D). A) Shows the orientational texture. B) The average intensity for the 36 image recorded of the area, each with a different orientation of the excitation light. C) shows a line scan of the marked line in B. This shows the intensity in the dark region (left side) is about half the intensity of the bright region (right side). Confirming the $L_{\beta'}$ domain is located in the 2nd level of bilayers. The scale bar is 5 μm .

observed texture is not completely comparable to the DOPC,DPPC mixture used in this chapter. The orientational texture for a $L_{\beta'}$ domain in the second layer of the DOPC, SM-C₁₈ mixture are shown Figure 4.10A. It is evident from that image the domain exhibit an orientational texture. The image is not of a particular high quality, for instance the orientations for the top part of the domain seem to be missing. This is caused by a misalignment of the sample and the 2-photon excitation laser. In Figure 4.10B the average intensity of the 36 image (with different orientation of the excitation light) recorded of the area is shown. It can be seen that the domain is located in a second bilayer by comparing the dark region of the image (left and bottom), with the rest of the image which also includes the domain. A line scan that goes across both those region is shown in Figure 4.10C and marked in Figure 4.10B. The values in the dark region (pixel 0-75 in Figure 4.10C) is about half that of the brighter region² (pixel 100-256 Figure 4.10C), which confirms the presence of a first and second bilayer in the images, as schematized in Figure 4.10D. The observation of orientational texture in the second bilayer clearly indicates that the orientational texture is not merely an artifact caused by the forces between the substrate and the bilayer.

² The images are recorded using PMT, which means we do not have to worry about a gray scale offset as with CCD cameras. A complete dark image will have the value 0 for PMT, but for a CCD it will be a finite nonzero value dependent on the camera.

4.7 Discussion

In this chapter different types of image analysis of textures defect in membrane $L_{\beta'}$ domains, based on fluorescence polarizations scans, have been shown. The results reveal a complex pattern of defects and several issues and topics for further study have arisen.

First we discuss a possible correlation between the domain shape and the texture pattern. In the present system this correlation is found to be rather weak, but one could in general imagine this coupling to work in at least two ways: (1) That texture created early in the growth/nucleation regulates the domain shape during growth by defining certain optimal growth directions or: (2) That the domain shape controls texture via boundary conditions.

Regarding the first mechanism, the smallest leaf-shaped domains we have studied will typically contain six leaves that coincide with the six-fold texture pattern of a hexatic lattice. Such small domains are seen for temperatures slightly below the transition temperature and indicate that the domain shape can be partially controlled by the hexatic lattice and the point defect. However the larger domains forming at lower temperatures become more branched and asymmetric and this simple relationship is no longer valid.

Regarding the second mechanism, one could expect domain shape and texture to couple via boundary conditions for the director at the domain perimeter. In monolayers, normal boundary conditions are expected rather than parallel conditions, according to Fischer et al.[20] But in Figure 4.3, the director orientation is not fixed with respect to the boundary, and it can be concluded that this energy apparently is not strong enough to visibly align the texture with respect to the boundary. This indicates a rather weak influence of boundary conditions for large domains. Coupling between shape and texture could also occur via the energy cost of creating defect lines (splay and bendwalls). In this case, energy could be minimized by shortening the defect line leading to invaginations in the domain shape where the lines intersect the boundary. From Figure 4.3A-D this is seen for most of the lines, but not all. This indicates some variation in line energy, possibly related to the bend or splay character of the lines.

In this group $L_{\beta'}$ domain shapes have previously been examined in detail and found that shape is highly regulated by another mechanism, namely the spatial pattern of neighboring domains. The pattern of nucleation sites in the membrane effectively creates capture zones around each domain defining its nearest neighborhood region. The shape of such zones (Voronoi polygons) was shown to correlate strongly with the shape of domains possibly through competition for gel-phase lipids during growth. The correlation was increasingly strong for larger domains.[59]

Recently Longo and Blanchette reviewed various mechanisms influencing the shapes of cerebroside-rich domains in model membranes.[78] One of the mechanisms discussed was edge diffusion of lipids in gel domains. It has been observed[79] that gel domains may change isothermally from branched to more compact shapes following several hours after formation. This is attributed to edge diffusion and line tension which redistributing material to make the domain more circular, thereby shortening the perimeter and lowering the boundary energy. We did not specifically study shape relaxations in this work but this slow process is likely to occur. The influence of shape changes on the texture will depend on the importance of boundary conditions and may also be related to the lipid composition. In this system, boundary conditions for large domains are not strongly enforced. One possibility is that edge diffusion may simply lead to an ‘epitaxial’ redistribution of material on the edge such that the boundary shape changes, but without major changes in the texture pattern. Such behavior has in fact been seen in monolayer studies by Iñes-Mullol et al.[80] In bilayers this hypothesis should be subject to further study and verification.

In general, the domains should not be regarded as being in thermodynamic equilibrium although they are cooled slowly and are stable for several hours. The question of equilibrium should always be associated with a characteristic time scale for the equilibrium state since remodeling of domains and their texture may occur over several regimes and be slowed by high energy barriers. True thermodynamic equilibrium in these systems may be difficult to obtain on realistic time scales.

In contrast to typical monolayer textures,[81] the membrane textures display a radial variation of the defects. The trend is that the center always has continuous texture which transforms to a segmented structure with defect lines emerging at some distance from the center. In general, when the bond angle field and the tilt orientation are coupled we have a locked texture, as described in section 2.4. Here the c -director is bound to the hexatic grid, which is continuously varying. Line defects represent a local un-locking of these fields where the director orientation jumps to another minimum with respect to the bond angle field. Continuous textures are expected when the rigidity of the hexatic lattice (hexatic stiffness, K_6) is low and conversely for high hexatic stiffness it is more energetically favorable to create line defects separating segments with uniform orientation. One possible reason for the mixed character of the domains is that they are grown thermally. This means that the decreasing temperature during growth is captured as a spatial variation from the center towards the domain boundary. If the hexatic stiffness and/or other elastic constants of the free energy are temperature dependent, then a radial variation in the preferred texture could arise. Assuming that the hexatic stiffness decreases with temperature,[29] it would be expected that the outer regions (lower temperature) of a domain should be segmented and the center (higher temperature) should be continuous. This is indeed what is observed in the results. A similar issue was previously discussed by Iñes-Mullol et al.[80] who,

contrary to expectations, found continuous textures at low temperatures and segmented textures at higher temperatures in their DMPE monolayers using BAM microscopy to detect defect line and lipid orientations.

The line defects in the bilayers are more complex than the defect lines in monolayers. In this system the lines are generally not straight, but may consist of linear segments. The bend/splay character varies between lines in the same domain. There is also a significant variation in the jump-angle of lines as demonstrated in Figure 4.5 and Figure 4.4. The radial variation in jump-angle for the same line defect may be attributed to the thermal growth conditions as discussed above. Variations in temperature could possibly influence the potential for coupling between the bond angle field and the lipid orientation and thus also the jump-angle.[33, 82]

The fact that the jump-angle deviates from 60° suggest that the I- or F-phases, as discussed in chapter 2.4, are not likely to exist in the domains, since they consist of 6 distinct molecular orientations with 60° apart. For the L-phase however, jump angles below 60° can occur. The observed large variability in jump-angles and their spatial variation in membranes points to a complex coupling between the bond angle field and the director with a possible similarity with the L-phase.

An interesting aspect arises when we comparing the two different ways of calculating the orientations difference for two neighboring subdomains. The calculated jump-angle, as seen in Figure 4.5, gives in general smaller values than the orientation histogram approach, as seen in Figure 4.6 and Table 4.1.

As mentioned earlier orientation change associated with a defect line does not account for the entire change of orientation between neighboring subdomains. Some change of orientation must therefore occur within the subdomain and away from the defect line, likely caused by a gradual deformation of the hexatic grid.

The width of the defect lines is probably below the optical resolution limit of our microscope. As mentioned in chapter 2.4, information about the width of the defect line may allow one to estimate some of the elastic constants in the Landau free energy as proposed by Fischer et al.[20] AFM imaging of defect lines in monolayer domains has shown that the lines are at least below ≈ 100 nanometers.[81, 83, 84] We have attempted to image bilayer textures with friction and tapping-phase AFM for higher resolution, but without obtaining adequate contrast. This is not entirely unexpected since AFM on monolayer involves the tip interacting with the lipid acyl chain; whereas AFM on bilayer the tip interacts with the hydrated lipid head groups, which may not show any of the orientational texture the lipid acyl chains exhibit.

The observation of a pair of $|m| = 1/2$ point disclinations in the domain center is not made in monolayers under equilibrium conditions. The stability of a $|m| = 1/2$ disclination pair depends on the balance between the elastic repulsion between the point defects and the tension in the defect line connecting the two points. Under equilibrium conditions in monolayers, splitting of the central defect into

pairs will not happen due to a dominating contribution from the line tension. It has however been shown by Hatta and Fischer that infrared laser heating of a polymerized monolayer can produce this splitting.[85, 86] The fact that we observe a $|m| = 1/2$ disclination pair in bilayer domains suggests that the relative contribution from line tension is weaker in bilayers. The weak alignment between the defect pairs as seen in Figure 4.9B could possibly be ascribed to interactions with the crystalline mica substrate or to physical interactions between the domains following their nucleation. From a fit of the simulated texture pattern to the measurement it was possible to determine the value of $\varphi_{s0} = 60.5^\circ \pm 6.5^\circ$. With this value the texture becomes a spiral, that is intermediate between a pure bend or pure splay texture. All domains have essentially the same spiral pattern with a narrow spread in the values of φ_{s0} . This indicates that it is conserved and a characteristic property of the domains, possibly related to the membrane lipid composition and/or the thermal history of the sample.

The phenomenon of half-integer disclinations connected by a defect line has historically been observed in XY-model simulations as well as in experiments on smectic liquid crystals. Swendsen[87] and Lee et al.[88], both found patterns of strings connecting half-integer vortices in XY-type simulations. Subsequently Pang et al.[89] found intricate patterns of strings connecting fractionally charged vortices in tilted smectic-C liquid crystal thin films. Some of their patterns contained strings connecting $1/2$ vortices similar to ours, while others had different topological defects involving branched and circular string as well as vortex-antivortex pairs of zero net charge. An important difference between such liquid crystal and monolayer/bilayer textures is that liquid crystals are effectively infinite 2D systems with defects emerging spontaneously whereas in monolayers and bilayers the system is finite and texture may be regulated by boundary effects and the domain nucleation.

4.8 Conclusion

In this chapter it has been demonstrated how the orientational texture of $L_{\beta'}$ domains in a DOPC,DPPC (1:1) bilayers using polarized two-photon fluorescence microscopy could be measured. The domains were found to have a complex texture that involved a division into subdomains, in the outer part of the domains. The subdomains were separated by defect lines, whereas the center of the domains show a continuously change of orientation. The domains were found to be divided into 6 subdomains, which were connected to the center of the domain, each with a unique orientation of c-director. The differences between the orientations in the subdomains were different than the expected 60° for 6 evenly spaced subdomains. The same trend were found if the orientation were measured going across a single defect line, in which case the change of orientation were always less than 60° . A further study of the center of the domain revealed a vortex like change of orientation converging into two $m = 1/2$ point defects. Furthermore it was possible to fit the observed texture around those defect, and extract the offset value ($\varphi_{s0} = 60.5^\circ$), which describe the splay/bend characteristics of the vortex like structure. This value was found to be almost equal for all the domains of this specific mixture.

Chapter 5

Influence of Lipid Composition on Texture in Lipid Bilayers

In the previous chapter it was established that the $L_{\beta'}$ phase had a complex and intriguing orientational texture. This discovery has led to several new questions regarding the mechanisms and forces that control and form these orientational textures. A systematic research was therefore needed in order to shed light onto those phenomena.

As previously mentioned the energy at the interface between the two phases is a core element in explaining the orientational texture. Hence such an excellent place to start the study would be the hydrophobic mismatch between the two phases. The hydrophobic mismatch has been reported to affect many aspects of phase separation and domain formation, such as line tension[90], domain nucleation[91], domain size, and de-mixing temperature[92].

The hydrophobic mismatch can be manipulated experimentally by exchanging the lipids in the model membrane. Specifically it can be done by changing the length of the fatty acid tail of the lipid. In this chapter we report how changes in the hydrophobic mismatch affect the formation, and the orientational texture, of the domains. We have used these observations to gain insight into what controls and induces the orientational texture of the $L_{\beta'}$ phase.

This will start by an explanation about experimental preparation that was needed in order to make comparable measurements for the different mixtures (Section 5.1). After the different mixtures will be compared regarding the orientational texture (Section 5.2), the distribution of orientations within the domain (Section 5.3), the central vortex structure (Section 5.4), the hydrophobic mismatch (Section 5.5) and the intrinsic tilt of lipids (Section 5.6). Lastly the orientation of the lipids at the boundary of the domains will be examined (Section 5.7). This will be followed by discussion of the different results.

5.1 Experimental Preparations

In this work we investigated the texture of several different lipid mixtures. As with any model system it is imperative to choose the system which will provide relevant answers to your specific problem. For this study we wanted to affect the membrane domain formation, by changing as few physical parameters as possible.

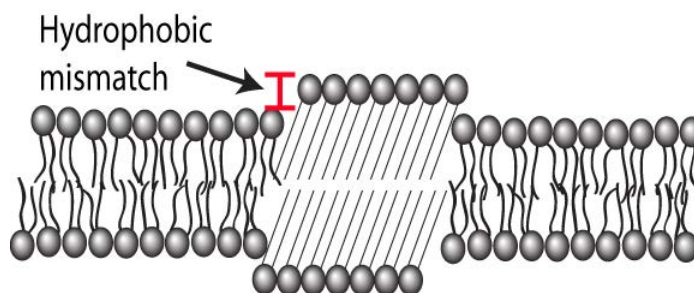


Figure 5.1 Illustration of the hydrophobic mismatch in a membrane with coexisting phases. During the condensation of the lipid into the $L_{\beta'}$ phase the thickness of the membrane will increase, thus creating a height difference between the two phases

We therefore decided to create model membranes with different lipid mixtures, with identical head-groups, i.e. phosphatidylcholine (PC), while changing the tail-length and/or the degree of saturation. This would effectively alter the hydrophobic mismatch between the $L_{\beta'}$ and L_{α} phases as seen in Figure 5.1 Three different lipids with a low melting temperature were chosen (the main component in the L_{α} phase), namely DOPC, POPC, and DLPC, whereas the three lipids with a high melting temperature were (the main component in the $L_{\beta'}$ phase) DMPC, DPPC, and DSPC. The melting temperature of the different lipids can be seen in Table 5.1[93], and the structure in Figure 5.2.

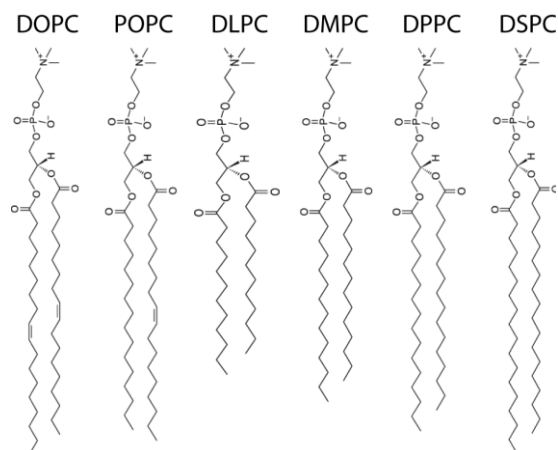


Figure 5.2 The different lipids used in this chapter to investigate the effect of the hydrophobic mismatch on the texture.

Prior to the measurements described in this chapter extensive work was carried out, in order to determine experimental parameters for the different mixtures. The goal was to create sufficient large macroscopic domains of similar size in a temperature range suitable for the microscope. This meant we wanted to have domains of a size about 10-20 μm , and as close to 20°C (room temperature) as possible. There were two problems associated with temperatures away from 20°C. Firstly the fluid cell had trouble cooling

	DOPC	POPC	DLPC	DMPC	DPPC	DSPC
Melting temperature ($L_{\beta'} \rightarrow L_{\alpha}$)	-18.3°C	-2.5°C	6.6°C	23.6°C	41.3°C	54.5°C

Table 5.1 Melting temperature from the 6 different lipids used in this chapter.

	DOPC DMPC	POPC DMPC	DOPC DPPC	POPC DPPC	DLPC DPPC	DOPC DSPC	POPC DSPC	DLPC DSPC
Name	I	II	IV	V	VI	VII	VIII	IX
Molar mixture	1:3	1:2	1:1	1:1	1:1	2:1	2:1	2:1
Cooling rate (per min)	0.1°C	0.1°C	1.0°C	1.0°C	1.0°C	1.0°C	1.0°C	1.0°C
Recording temperature	14 °C	20 °C						

Table 5.2 Experimental condition for the 8 different mixtures, the name row will be used to ease referral to the different compounds during the discussion.

anything below 17°C, and secondly the objective used in the microscope was a water immersion objective, which meant the objective, and the microscope, would act as a heat sink. The objective could be replaced with an air objective, but with significant impact on the quality of the results, which will be discussed in Section 5.7. We had two controllable parameters which could help us obtain the right domain size at the right temperature; 1. The ratio between the two lipids; this affects the horizontal position in the phase diagram, and thus the transition temperature and the molar fraction of the two phases. 2. The cooling rate; which affect the number of domains that are nucleated within a given area[59], and thereby affecting the size of the final domains.

Using those two control parameter we indentified the experimental conditions needed for 8 of the different mixtures, shown in Table 5.2. The missing mixture (DLPC,DMPC) was made and measured. However the quality of the supported bilayer was very low, due to human errors, and therefore results for that mixture are not included in this thesis. In the following sections, references to the different mixtures will be numerous, and in an attempt to simplify this each mixture have been given a Roman numeral as seen in the top row of Table 5.2. Notice the perturbation due to the missing mixture (DLPC,DMPC). The numbers have been chosen so that all samples containing DMPC have I, II, whereas DPPC is IV, V, VI lastly DSPC is VII, VIII, IX. The same goes for the low melting temperature lipids, where mixtures containing DOPC is I, IV, VII, whereas POPC is, II, V, VIII and DLPC is VI, IX. In the following sections the mixtures will be named by one or two lipid(s) and a Roman numeral, e.g. DLPC,DSPC (IX) refers to the specific mixture of DLPC,DSPC, whereas DPPC (IV-VI) refers to all the three mixtures containing DPPC, which is DOPC,DPPC; POPC,DPPC; and DLPC,DPPC.

5.2 Orientational Texture

The orientational texture for the eight different mixtures can be seen in Figure 5.3, and several features are immediately clear. Firstly the domains containing DPPC (IV-VI) and DSPC (VII-IX) have similar texture as the one described for the DOPC,DPPC mixture (IV) in Chapter 4. The spiral vortex-like texture at the nucleation center of the domains is preserved. The orientation varies across the domains, which are divided into more or less well defined subdomains, some of which are divided by line defects.

The DMPC (I,II) domains show remarkably different texture. For the DOPC,DMPC (I) mixture we see a few domains with a uniform texture (e.g. the big green domain), however most of the domains have a large uniform part, and smaller subparts with different orientation. The POPC,DMPC (II) mixture shows a

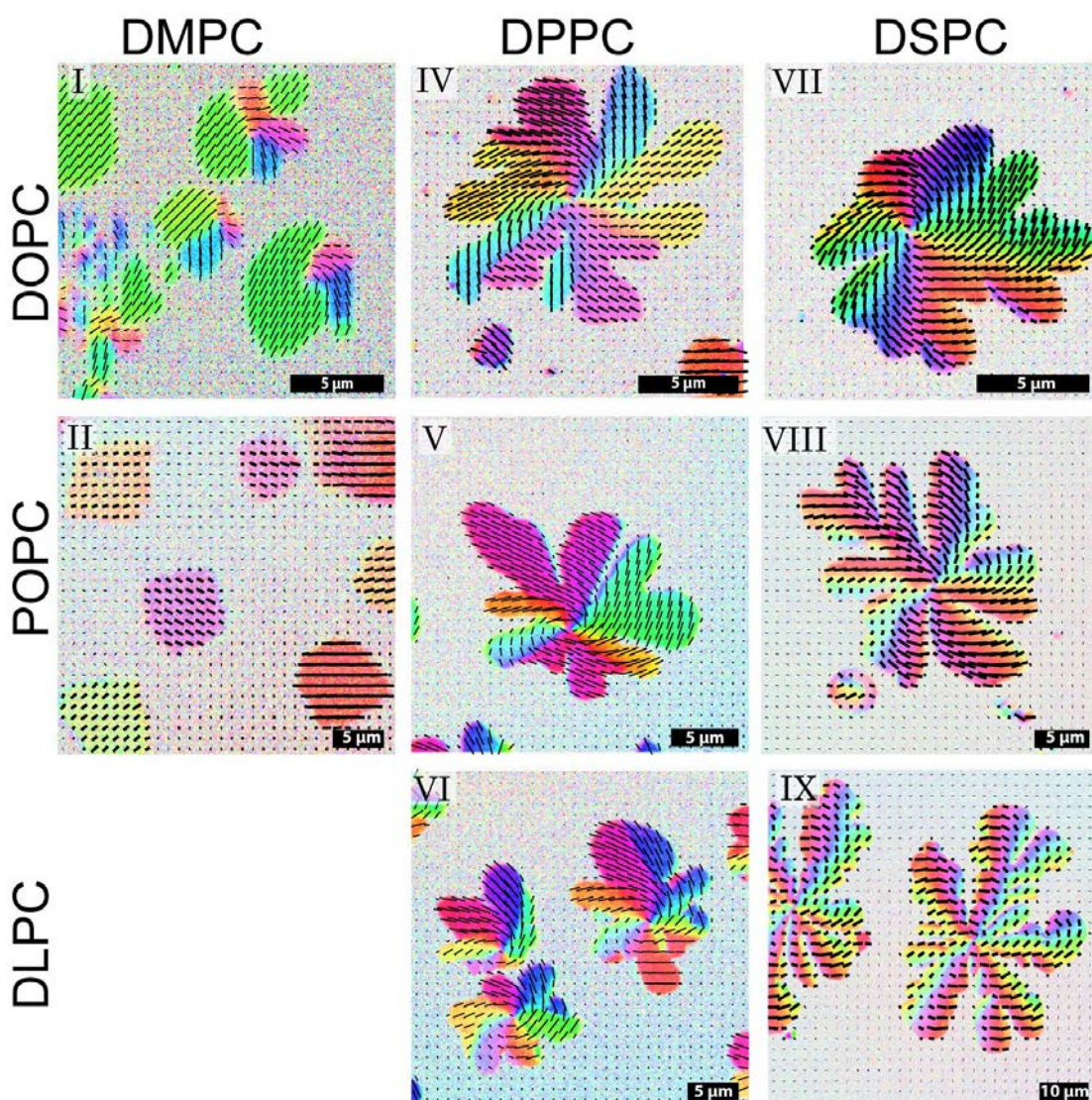


Figure 5.3 Overview of the texture for the 8 different samples made from the 6 different lipids. For a more detailed description on the mixture ratios and the experimental conditions see table 5.1.

uniform texture with no change of orientation across the entire domain. Several domains are observed in the image each with a different orientation, thus ensuring the uniform texture is not an effect of the mica substrate used. The shape of the DMPC (I,II) domains are roughly circular, which is in large contrast to the flower-shaped domains observed for the other domains.

The domains were analyzed using many of the same analysis described in Chapter 4 for the DOPC,DPPC domains (IV).

5.3 Distribution of Orientations within the Domains

To investigate the distribution of orientation within each domain, the values were plotted in an orientation histogram, and subsequently recolored, as described in detail in chapter 4.3. The DPPC (V,VI) domains are shown in Figure 5.4, while the DSPC (VII-IX) domains are shown in Figure 5.5. For the two mixtures containing DPPC, namely the POPC, DPPC (V) and DLPC, DPPC (VI) mixtures, we see a pattern that is qualitative similar to the pattern observed for the DOPC,DPPC (IV) domains discussed in chapter 4.3. The domains are divided into 6 subdomains with different orientation, connected to the center.

The DSPC (VII-IX) domains in Figure 5.5 are more complicated to interpret. The DOPC DSPC (VII) mixture, Figure 5.5A, shows the same pattern as described above. The peaks in the histogram however, are less distinct, and the relative height of the peaks, compared to the lowest value (the “background”), are much smaller than in the DPPC case, as seen in Figure 5.4 . However the pattern remains the same and 6 subdomains are connected to the center.

The observations for the POPC,DSPC (VIII) and DLPC,DSPC (IX) are not that simple since they split into two different populations within each mixture. Two domains are shown for the POPC,DSPC (VIII) mixture in Figure 5.5B+C. The domains are about equal in size and recorded from the same sample. In the texture images (Figure 5.5B1+C1) the difference is easily recognized. Figure 5.5(B1) has a clear distinction between the different subdomains. The orientation histogram (B3) shows 5 distinct peaks corresponding to 6 subdomains, as are evident in the re-colored image (B2). The orientational texture showed in Figure 5.5(C1) does not seem to have any sharp distinction between the subdomains. The orientation histogram (C3) confirms this, and does not show a clear division into peaks.

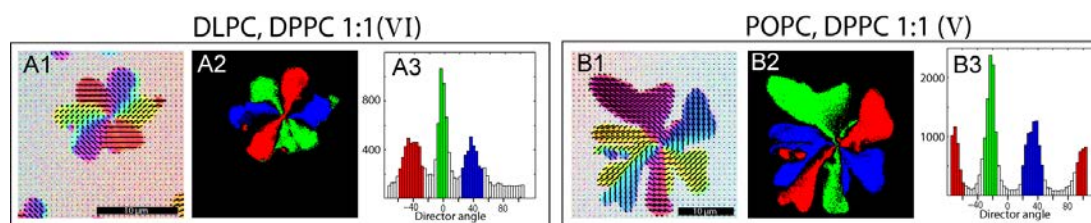


Figure 5.4 Histogram and re-colored images from the orientation for the DLPC DPPC and POPC DPPC mixtures. Both samples show the same pattern observed for the DOPC DPPC mixtures described in details in Chapter 4.3 The domains are clearly divided into 6 subdomains. Scale bars are 10 μm

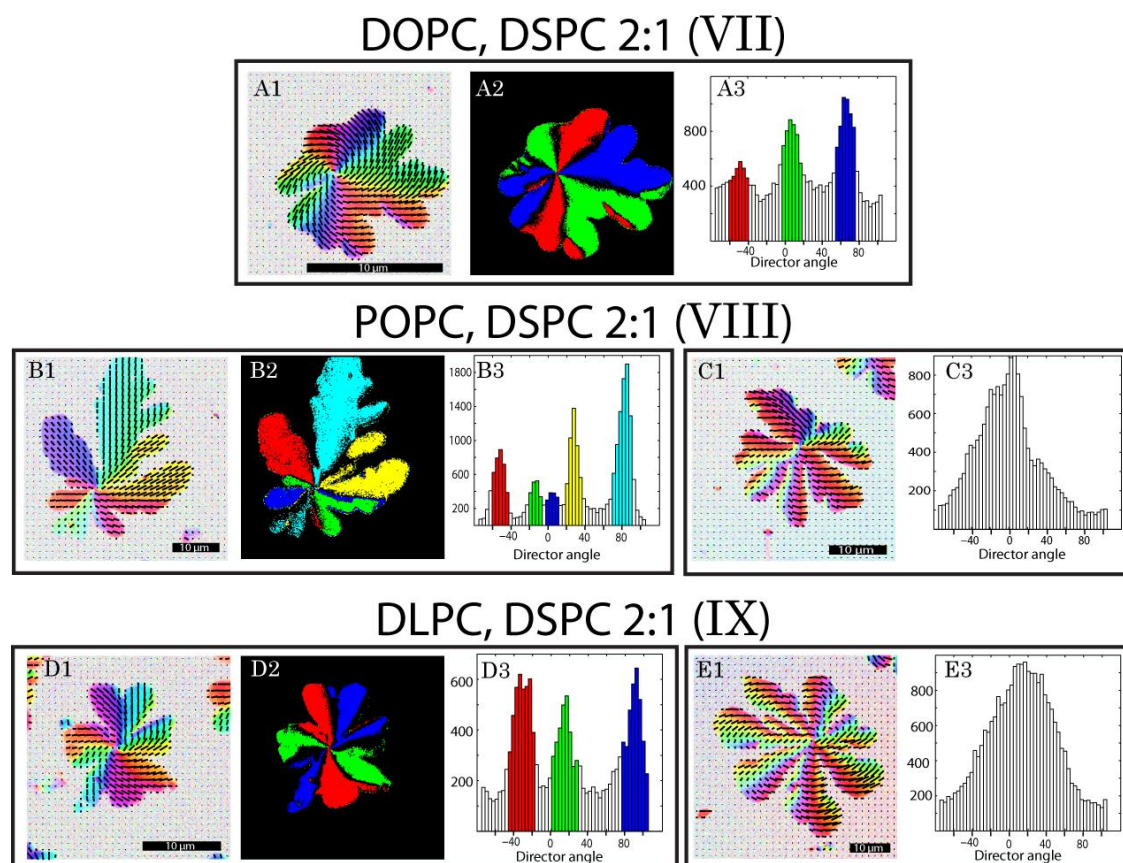


Figure 5.5 Histogram and re-colored images from the orientation for the three mixtures containing DSPC. All the mixtures can show subdivision of orientation. However the POPC DSPC and DLPC DSPC domains can also show domains with no clear subdivision, e.g. the two domains to the right. Scale bars are 10 μm

Instead one very broad peak is observed, which again confirms the lack of clear division into subdomains. Instead the change of orientation happens continuously, which is especially evident in the outer part of the domain. This domain has not been re-colored as the other images.

For the DLPC,DSPC (IX) domains, Figure 5.5D+E, we see the same pattern as the POPC,DSPC (VIII) domains described above; two different domains, one showing several peaks(D3), and one showing one large and wide ‘peak’ (E3). However in this case there is a size difference between the two domains. This is caused by a difference in the preparation of the two samples. One way of changing the size of the domain is through the cooling rate, if a sample is cooled faster, more nucleation points per area will arise, thus resulting in smaller but more numerous domains.[59] In this case the small domain Figure 5.5D (which was cooled fastest) shows 6 subdomains, whereas the large domain, Figure 5.5E, shows a clear, visible, and continuously changes of orientation across each leaf of the domain. This could indicate some dependency between the texture and the size of the domain.

A closer inspection of the two domains, of the DLPC,DSPC (IX) mixture, can be seen in Figure 5.6. For the large domain Figure 5.6A+B we see a clear change of

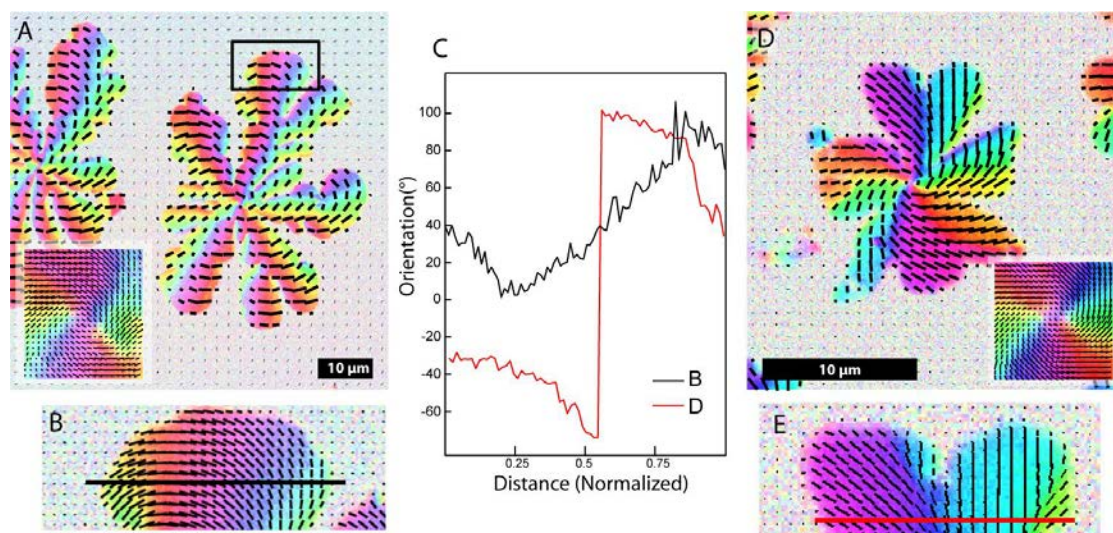


Figure 5.6 A) Texture image domains in a DLPC DSPC 2:1 membrane, insert shows the texture around the nucleation center. B) shows a zoom of the region marked with the black box in A. As it is clearly evident the orientation changes across the leaflet. C) Shows a line scan of the orientation for the two domains: (B) is black line, (E) red line. D) Texture image of DLPC DSPC 2:1 domain, much smaller than the other (A). E) shows a zoom of a leaflet in D. The two inserts show the texture around the nucleation center for A+D.

orientation across the one leaflet. This is further highlighted in the graph (C), which shows a line scan across the leaflet (black line), where the orientation changes continuously by almost 180° going across. This is in large contrast to the small domain (Figure 5.6D+E), cooled at a higher rate, which shows texture similar to the DPPC (IV-VI) domains. A closer inspection of the orientation across this leaflet is shown in Figure 5.6C (red line), where the change of orientation is clearly and almost exclusively confined to the defect line. A closer look at the nucleation center of the two structures reveals an interesting feature (Figure 5.6A+D insert): the texture around the nucleation center is almost identical for the two structures.

5.4 Central Vortex Texture

As described in Chapter 4.5 the texture around the nucleation center can be compared to a simulated texture and quantified to an offset value, φ_{s0} , which tells whether the observed texture is bend ($\varphi_{s0} = \pm \frac{\pi}{2}$), splay ($\varphi_{s0} = 0, \pi$), or a mixture of these two. We earlier identified that the DOPC, DPPC domains had an offset of $60.5^\circ \pm 6.5^\circ$ where the deviation is plus/minus one standard deviation. The same analysis was carried out for the mixtures showing a vortex texture in the center, i.e. sample IV-IX (the ones containing DPPC and DSPC), the result is shown in Table 5.3.

The offset value is reasonable identical for the three mixtures containing DPPC (IV-VI) with values in the range of $60^\circ - 70^\circ$. The DOPC,DSPC(VII) mixture gives a value of $62.8^\circ \pm 10.8^\circ$, which is similar to those. The POPC,DSPC(VIII) and DLPC,DSPC (IX) mixtures have values of about $35^\circ - 45^\circ$. The two samples of IX with different thermal history, and thereby different

domain sizes were compared. The small domains that were cooled faster had offset values of $43.8^\circ \pm 4.5^\circ$, whereas the values for the larger domains were $56.9^\circ \pm 4.6^\circ$. Although not equal they are within two standard deviations from each other, and taking into account the low number of measurement for each sample, 9 small domains and 16 large domains, those numbers can be related.

To illustrate these numbers two of the most extreme values have been shown in Figure 5.7A+B. The center of a POPC,DPPC (V) domain is shown in A, with an

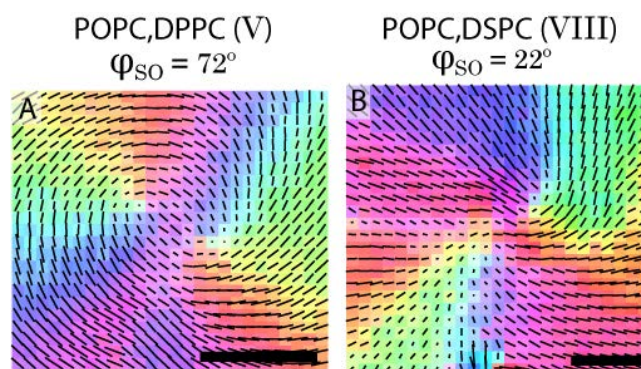


Figure 5.7 Two examples of the vortex texture in the center of the domains. (A) POPC,DSPC(V) have an offset value of -72° showing almost pure bend characteristics. (B) POPC,DSPC(VIII) have an offset value of -22° showing almost pure splay characteristics.

	DOPC DPPC	POPC DPPC	DLPC DPPC	DOPC DSPC	POPC DSPC	DLPC DSPC (1C/min)	DLPC DSPC (2C/min)	DLPC DSPC both
Name	IV	V	VI	VII	VIII	IX	IX	IX
φ_0	60.5°	73.9°	63.7°	62.8°	36.8°	56.9°	43.8°	48.5°
Standard deviation	6.5°	6.6°	6.6°	10.8°	12.3°	4.6°	4.5°	7.8°
N	10	9	16	13	8	9	16	25

Table 5.3 The offset values for the vortex like texture in the center of the domains, determined through a comparison to simulated texture.

offset value of 72° and therefore very close to a pure bend texture, whereas the POPC,DMPC (VIII) domain shown in B has an offset value of 22° and is therefore almost pure splay. This illustrates that the offset values is not just numbers, but the vortex structure for the two domains are visually different, and the observed texture matches well with the numbers.

5.5 Measuring the Hydrophobic Mismatch

As mentioned earlier the lipids in this chapter were all PC-lipids, to ensure that the only difference between the lipids were the size of the tail group. For the three high melting temperature lipids, the only difference was the length of the fatty acid tail, going from 14 carbon for the DMPC to 18 carbon for the DSPC. Therefore the physical parameter under investigation here is the hydrophobic mismatch between the L_α and the L_β' phase, as illustrated in Figure 5.1. AFM has been used to measure this height difference. The AFM images were recorded using contact mode in water on a sample where both phases were present. The samples were imaged with an identical and small force to ensure the measured height difference corresponded to the height difference of one leaflet. Images were recorded of several different domains at different location on the sample to prevent errors due to the sample. For each image the height was measured using an average of several lines across a domain edge, as indicated by the white boxes in Figure 5.8A-C, several measurement were taken for each image. The error bars in Figure 5.8D represent the standard deviation of those measurement, unless the standard deviation was smaller than the noise level from our AFM using contact mode in water (± 1.5 nm).

As expected the two DMPC mixtures (I, II) had a smaller hydrophobic mismatch than the two measured DPPC mixtures (IV, V). Interestingly the POPC,DMPC (II) had a hydrophobic mismatch of only 0.6 nm, whereas the DOPC,DMPC (I) was 0.9 nm. Therefore an exchange going from DOPC to POPC resulted in a lowering of the hydrophobic mismatch for the DMPC. The same is not found for the DPPC mixtures, where the hydrophobic mismatches are the same for

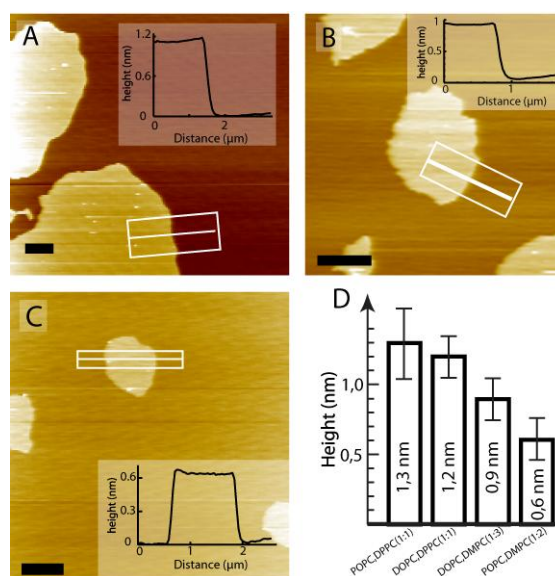


Figure 5.8 AFM images of three of the mixtures, DOPC DPPC 1:1 (A), DOPC DMPC 1:3 (B), and POPC DMPC 1:2 (C). Scale bars are 1 μ m. Inserts show line scans, taken as an average of the lines within the white boxes. The summary of several measurements is shown in D.

the two different mixtures with DOPC (IV) and POPC (V). A possible explanation is the fact that the L_α phase does not consist of 100% of the low temperature lipid (DOPC/POPC), which can also be seen in the phase diagram. Therefore the absolute thickness of the L_α phase is dependent on both lipids, and the ratio of the mixture, and therefore simple extrapolations, e.g. a change from DOPC to POPC lowers the hydrophobic mismatch, might not be valid.

Unfortunately the hydrophobic mismatch region is not measured for all the mixtures. However some assumptions can be made to the relative height of the eight mixtures. It is fair to assume that the DSPC domains, in general are thicker than the DPPC domains, thus indicating a larger hydrophobic mismatch between the DSPC domains and the fluid phases. Similarly it is a fair assumption that the DLPC forms the thinnest fluid phases. If this assumption is true it means that the mixtures showing a uniform or nearly uniform textures all have hydrophobic mismatches below 1.2 nm (I, II) whereas the mixtures with vortices have height differences above or equal to 1.2 nm (IV- IX).

5.6 Orientation at the Phase Boundary

It is interesting to study the connection between the phase boundary and the orientation at the boundary in a more quantitative way than pure observations. Therefore a Matlab GUI was implemented, which was able to calculate this angle for each pixel on the boundary. The procedure involved the following 6 steps in which the orientations at the boundary were found and compared to the normal of the boundary. An example of this procedure is shown in Figure 5.9:

1. The boundary of the domain was located through the binary cutoff value used to segment the domain in section 4.3
2. In order to avoid the effect of the pixels and their very finite step size, the boundary coordinates were smoothed in both dimensions independently, by a simple moving average filter.
3. For each point on the perimeter a 3rd degree polynomial was fitted to the point $\pm n$ points, where n normally was 2-4 points
4. From the fit the tangent was found, and rotated 90° to form the normal vector at that point. The vectors can be seen in Figure 5.9B, the color representing the quality of the fit, as seen in the legend.
5. The orientation of the lipids was found for each point at the boundary, by moving inside the domain a few pixels in the direction of the normal vector located in step four. The orientations are shown as vectors Figure 5.9C, and are also plotted as a histogram Figure 5.9D. Notice the resemblance between this histogram and the orientation histogram from the entire domains, as seen in Figure 5.4(B3), regarding the peak positions.
6. The angles between the normal vector and the orientation vectors are calculated within a range of $[0; \pi/4]$, which is plotted in a histogram Figure 5.9E.

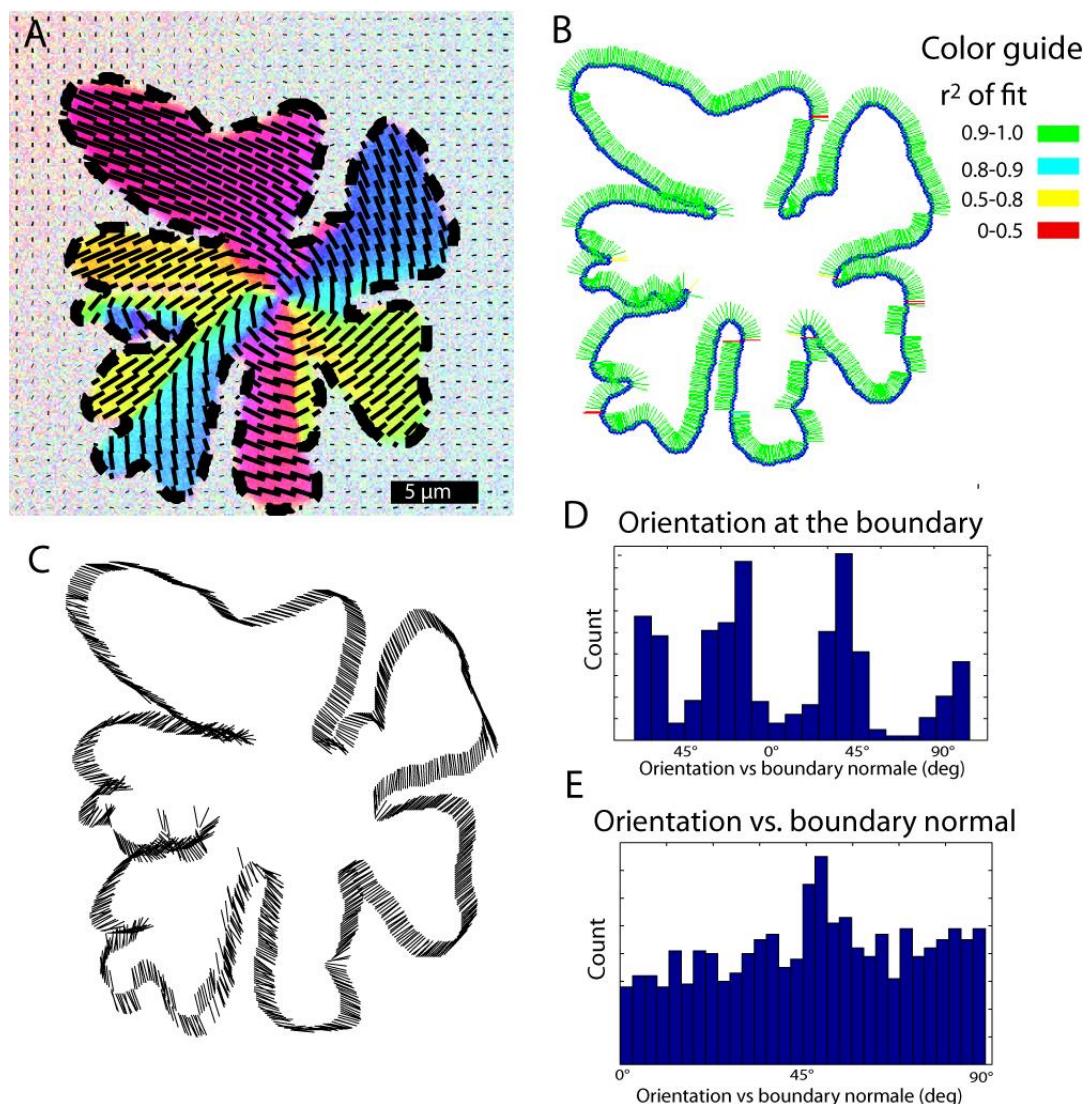


Figure 5.9 A) image of the texture of a POPC DPPC, with the boundary between the $L_{\beta'}$ and L_{α} phase shown by the dotted line. B) Shows the boundary and the vectors for the boundary normal, indicated by the colored lines, the color represent the quality of the fit used to calculate them. C) The texture calculated for each point on the boundary, also shown as a histogram in D. E) Histogram of the angle between the orientations (B) and the texture (C).

By looking at Figure 5.9 it is evident that the angles between the orientations and the boundary normal are more or less uniformly distributed between the 0° and 90° . There seems to be a small peak at 45° however nothing significant enough to be a trend. These analyses were done for several domains and several of the mixtures, all of which showed a uniform distribution of the angles. The uniform distribution is not entirely unexpected because the shape of the domains does not seem to be connected to the texture as discussed in chapter 4.6.

5.7 Texture of Early Domain Growth

As discussed in chapter 2.4 the domains are not grown isothermally but rather at a temperature ramp. This can affect the physical parameters, e.g. line tension, during domain growth. We therefore wished to investigate the texture during the domain formation, in order to see how the changes in temperature affected the texture, and to observe if any reorganization occurred. This proved a difficult task experimentally. As mentioned earlier the use of the water immersion objective was not possible at temperature different from room temperature. Hence the air immersion objective was used for these experiments. This however did cause several problems; firstly the air objective collects less light than the water immersion objective due to a lower NA. This problem could be solved by using a higher Laurdan concentration and/or a longer integration time for each pixel. Secondly it was much more sensitive towards misalignment between the microscope axis and the sample, where in some case a very non-uniform illumination of the sample was the result. Those faults resulted in several domains recorded during growth in which the fluorescence from half of the domain was “missing. This problem was simply solved by a time consuming “trial and error” process in which numerous samples have been used, and then using the one with an adequate alignment. There were also several problems involved in recording a sample that is undergoing change of temperature, but they were all found to be manageable.

Two of the mixtures have been investigated during the domain growth, namely the DOPC,DPPC (IV) and POPC,DMPC (II), and the measured

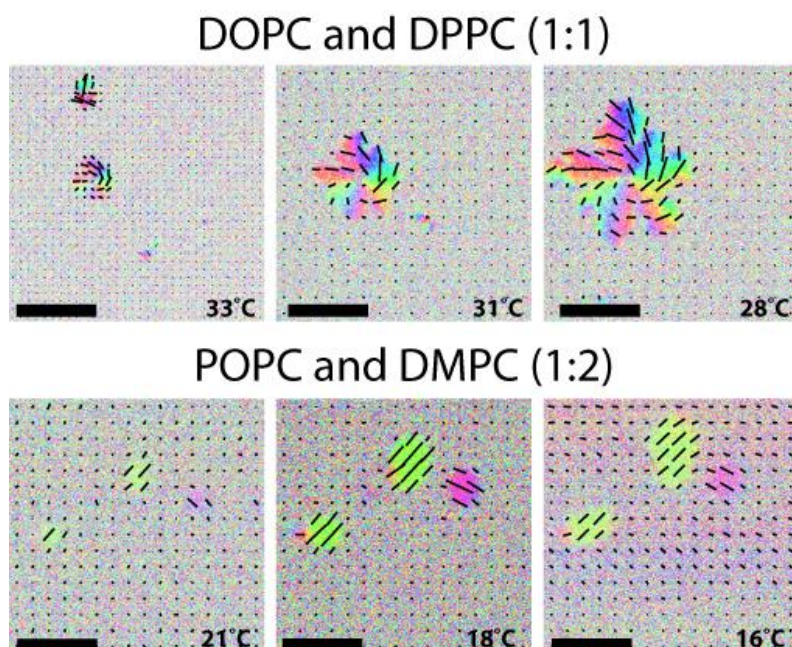


Figure 5.10 Image of the texture recorded during domain growth, across a temperature gradient. The images, for each mixture, are of the same area. Scale bars are 5 μm

orientational texture during the growth is shown in Figure 5.10, with mixture IV in the top row, and mixture II in the bottom row. The image with the highest temperature for each series has been taken as close to the nucleation as possible, and the images within each series are taken of the same area. The texture around the nucleation site remains constant during the further growth of the domain. Lipids that condense onto the domain during cooling have their orientation fixed to the texture of the existing domain. Thus the original texture formed during the nucleation is dominating for the texture of the rest of the domain growth.

As was discussed in the previous chapter the correlation between the shapes of the final domains is found to be rather weak, as was also illustrated with Figure 5.9. However this might not be the case for the smaller and earlier domains shortly after the nucleation. Therefore we wanted to measure the angle between the lipid orientations and the normal to the boundary for the early domain texture described in section 5.6. For the POPC,DMPC(II) it is simple enough, a uniform orientation and a roundish domain, will result in a uniform distribution of the angles between the orientation and the boundary normal. For the DOPC,DPPC (IV) mixture this need not be the case, a zoom of the texture from the first image in Figure 5.10 is shown in Figure 5.11. The domain appears roundish, and the texture is clearly visible, however it should also be noted that there is a significant amount of noise in the image, due to the difficulties described above. This impedes the detection of the phase boundary and makes an analysis similar to the one described in section 5.6 inadequate and noisy. However if the shape is round and there is a regular vortex structure, the angle towards the boundary is given by the offset value. Therefore the lipids in the DOPC,DPPC domain have an ordered orientation towards the boundary in the early domain growth, which is equal to the offset value. However as the shape changes during the domain growth, this ordering of the lipids towards the boundary vanishes due to the irregular domain shape.

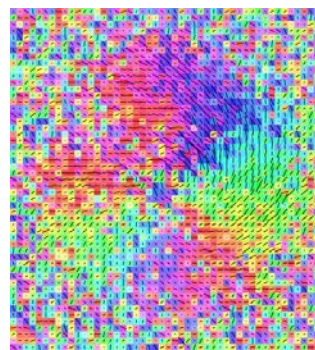


Figure 5.11 A zoom of the 33°C DOPC,DPPC mixture in Figure 5.10. The domain is found to be roundish. The signal to noise level is not excellent, which hinders the identification of the phase boundaries.

5.8 Domain Nucleation

An important parameter regarding the early growth of the domains is the nucleation density. Bernchou et al. investigated this thoroughly for a DOPC, DPPC mixture. [59] They investigated the number of nucleation per area as a function of the cooling rate, and found a linear dependency between the nucleation density and the cooling rate. The same quantitative measurements have unfortunately not been done for all the mixtures under investigation here. Instead a qualitative study has been made. This indicates that the mixtures with DMPC (I, II) have a higher nucleation density per area, resulting in small and more numerous domains, compared to the DPPC (IV-VI). The mixtures containing DSPC (VII-IX) show domains with the opposite trend, with a lower nucleation density per area, resulting in fewer large domains. These results are also apparent in Table 5.2, where the experimental parameters for the different mixtures are shown. The DMPC mixtures are cooled at a slower rate in order to generate sufficient large domains, whereas for the DSPC domains, a faster cooling rate were used to obtain domains of similar size as the DPPC, as earlier described. It should however be noted that the cooling rate is not the only part governing the domain size. The location in the phase diagram determines the molar fraction of the L_{β} phase and thereby also domain size. Since the average distance to neighboring domains is controlled by the cooling rate, this ultimately determines the individual domain size.[59]

The nucleation density was investigated for the POPC, DMPC (II) mixture. This and the results for Bernchou et al., regarding the DOPC, DPPC (II) mixture, is presented in Figure 5.12³. The experiment proved a linear relationship between the cooling rate and the nucleation density, with the equation given below:

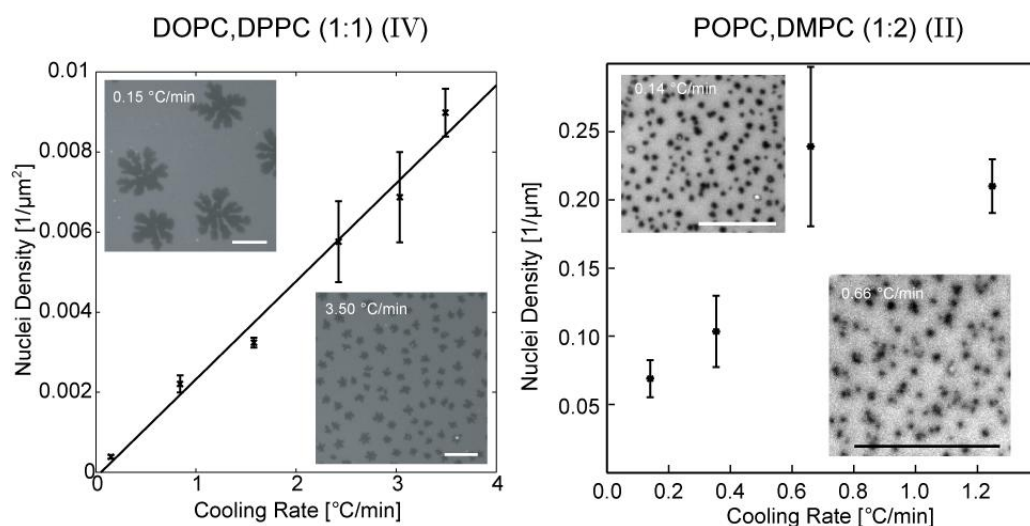


Figure 5.12 Density of nucleation for the DOPC,DDPC (1:1) mixture(IV) and the POPC,DMPC (1:2) mixture(II) as a function of cooling rate. The DOPC,DPC figure are borrowed with permission from Bernchou et al. Scale bars are 20 μm .

$$\text{Nuclei Density}_{(\text{DOPC, DPPC})} = (0.0025 \pm 0.0004) \frac{\text{min}}{\mu\text{m}^2 \cdot ^\circ\text{C}} \cdot \text{rate} \left(\frac{^\circ\text{C}}{\text{min}} \right) \quad \text{Eq. 5.1}$$

For the POPC,DMPC experiment also shown in Figure 5.12, the linear relationship is not as obviously. However it is easily seen that the slope is much higher than for the DOPC,DPPC mixture, and a linear fit gives the equation below.

$$\text{Nuclei Density}_{(\text{POPC, DMPC})} \approx (0.13) \frac{\text{min}}{\mu\text{m}^2 \cdot ^\circ\text{C}} \cdot \text{rate} \left(\frac{^\circ\text{C}}{\text{min}} \right) \quad \text{Eq. 5.2}$$

These results justify the qualitative description made from the DMPC (I, II) mixture made above. The linearity of the POPC,DMPC (II) results is however not that great, and the linear fit and equation is a coarse approximation at best. Several reasons can be thought to cause the large variation from a linear dependency. Firstly, there is an experimental uncertainty. The temperature cycling is very harsh on the model membrane, and the experiment has not been retried, therefore it is possible that one or more of the measurement point, could be moved by extra measurements points. Secondly the domains are very small, which make detection and distinction of the domains very difficult. Since this were done semi automated, by a script in ImageJ, systematic errors can have occurred. Lastly, as already mentioned the domains are very small, and it is possible there is a lower limit of domain size, and that we have reached that with the cooling of 1.2 °C/min. This would mean the Nuclei density as a function of cooling rate for the POPC,DMPC might only be linear at rates below approximately 0.6-0.8 °C/min, and at higher cooling rates it will stall and reach a plateau.

5.9 The Intrinsic Tilt of the Lipids

So far the intrinsic tilt (ρ) regarding the bilayer normal of the L_β phase for the different mixtures, as illustrated in figure 4.1, has not been mentioned. In theory we should be able to make a comparative study of the tilt (ρ) since we measure the director length as described in section 4.2, which should be related to the intrinsic tilt. However there is a multitude of experimental parameters that affect this measurement, e.g. concentration of fluorescence probe, laser intensity, gain settings of PMT. We are able to surpass many of those by normalizing the measurements to the isotropic fluid bilayer. However we have found that the director lengths are highly dependent on the geometry of the sample and the objective used. This has lead to inconsistent measurements within the same samples; therefore such a comparative study would be speculative, and biased towards the expectations from the literature.

In the literature several results have been shown for the lipids under investigation in this chapter. Most of the work has been done on DPPC, and some variations within the results are present. Watkins et al. made a comparison on DPPC monolayers and bilayers made with different techniques, using GIXD to

measure the tilt. The tilt in the monolayers was dependent on the lateral pressure, and as expected an increase in the pressure reduced the tilt. The tilts for the monolayers were: 31.0° , 30.6° and 25.8° for 30, 40 and 50 mN/m respectively. They measured the tilt for bilayers made with either Langmuir Blodgett-Schaeffer (LBS) (at 45 mN/m) or vesicle fusion, showing a tilt of 26.8° and 27.3° , respectively. They found the vesicle fusion produced more inhomogeneous bilayers than the LBS.[31] The tilt of DPPC was also measured by Sun et al. and Katsaras et al. using x-ray scattering and found to be 31.6° or 33° respectively.[94, 95] Tristram et al. measured the tilt of DMPC and found it to be close to DPPC and measured a value between 31.3° - 32.6° .[96] Sun et al. made a later study where they investigated the tilt as a function of the chain length going from C16 (DPPC) to C24. They found the tilt increased slightly as the chain length increased, giving DSPC a tilt of 32.5° in respect to the 31.6° for the DPPC.[97]

The actual tilt of the DPPC in our sample can be difficult to determine because of the distribution presented above. The trend presented by Sun et al. is very useful since it compares different lipids measured with the same technique. The tilt of the DPPC is likely close to 30° , with DMPC having a slightly small tilt, and the DSPC a slightly higher tilt. However the changes are very small, and are not considered having a large effect on the textures observed.

5.10 Discussion

The various orientational textures exhibited by the different mixtures have been shown in the sections above. Through the different analyses the similarities and difference were highlighted. The significance of the height of the hydrophobic mismatch region has been shown, and the texture of the small recently nucleated domains have been investigated and followed during the non-isothermal growth. However those observations should be placed in a context and through that describe which parameters are important for the texture, and how they affect it.

We will start this discussion by looking at the energy of domain and its texture. This will be done with inspiration from Fisher et al.,[20] as was done in chapter 2, where the energy of domains in monolayers were investigated. This discussion will therefore be based upon the assumption that the L_{β} phase under discussion is a hexatic phase as discussed in the previous chapter. However many of the arguments will still be true even if this is not the case, but the terminology would be different.

The energy cost of the texture for a domain can be split into the energy of the bulk of the domain (E_{bulk}), and the energy of the border of the domain (E_i).

$$E = E_{bulk} + E_i \quad \text{Eq. 5.3}$$

As Fisher et al.[20] explains the minimum energy contribution for the bulk is that of an uniform texture since it does not involve any defects or bend/splay in the hexatic grid, which must be true for both a monolayer and a bilayer

They further examined the energy difference between domains with a uniform texture or another texture, i.e. a splay texture (Eq. 2.16) or a defect pattern (Eq. 2.31) , and they find that uniform texture is only allowed for domains smaller than a certain size, related to the magnitude of the energy gain by having a specific orientation regarding the boundary normal, and the energy cost of bending the hexatic grid and/or the energy of the point defect in the center.[20] Monolayer systems however rarely/never show uniform texture. Which indicates that the energy gain by ordering the tails at the border of the domain, i.e. perpendicular or parallel, is higher than the energy cost of creating defect lines and/or point defects, thus domain orientational texture in monolayer is governed by boundary conditions. This does not seem to be the case for the bilayer system. The textures for the different mixtures, shown in Figure 5.3, do not indicate any preferred orientation towards the boundary. The orientation towards the boundary was further examined for the POPC,DPPC mixture in Figure 5.9, which again showed no preferred orientation. The other mixtures in this chapter have been examined as well, but none of them showed any significant difference from the histogram showed in Figure 5.9E. In other words the shape of the domains and the orientational texture are decoupled.

Another important energy parameter is the shape of the domain. The shape can roughly be divided into three groups, each controlled by a different mechanism.

- Line tension, low perimeter to area fraction. Would result in round domains.
- Texture defects and a preferred orientation towards the boundary. Would result in roundish hexagonal or six-leaved flowers[20], as seen in Figure 2.8.
- Diffusion limited aggregation (DLA). Would result in fractal ice crystal like domains.[98, 99]

The DMPC domains (I, II), which are roundish, fall nicely into the first category. For DSPC (VII-IX) and DPPC (IV-VI) domains the shape does not seem to be governed by one single phenomenon. We are currently investigating how the shape of the DPPC and DSPC domains can be explained. Through computer simulations, done by Jonas Camillus Jeppesen and Glenn Nielsen, we have been able to replicate the shapes of the domains by using an alternated DLA method, with the results shown in Figure 5.13. The DLA have been performed on a hexagonal grid, where the probability of condensation/adhesion is depended made curvature depended (line tension). The aggregated domain is allowed to relax after adhesion of each particle, to a structure with a smaller curvature, this is controlled by the line tension (γ).

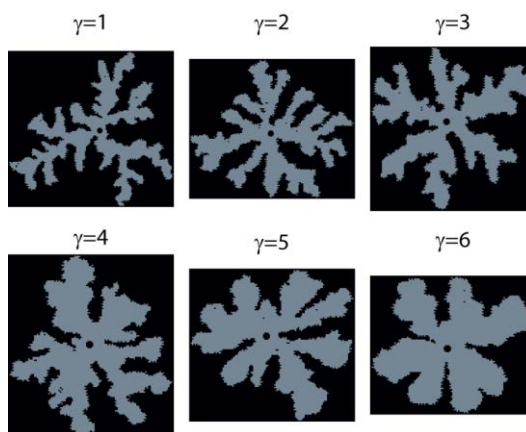


Figure 5.13 The effect of line tension on the domain shape, measured through a computer model. As the line tension increases the domain shape starts to resemble the one obtain in experiments.

This proves that the line tension is an important parameter, at least regarding the domain shape. If one disregards the orientation towards the boundary as an effect on the line tension, the main parameter governing the size of the line tension should be the hydrophobic mismatch[90, 92], the greater the hydrophobic mismatch, the greater the line tension. This would indicate that those mixtures with the highest mismatch region, DSPC > DPPC > DMPC, should have the highest tendency towards round or roundish domains. However the opposite trend is observed. The DMPC domains (I, II), which have the smallest hydrophobic mismatch, are expressed in round domains. This is a clear sign, that either the orientation has an important role in the domain shape and/or line tension, or there is another more important physical property that governs the line tension.

One possible explanation for the round shape of the DMPC containing domain (I, II) could be found with the experimental parameter in Table 5.2, since both those samples (I, II) were cooled much slower than the remaining samples. Longo and Blanchette et al. showed that domain reshaping can take place, in which edged diffusion allows the domain to reduce its circumference by making it

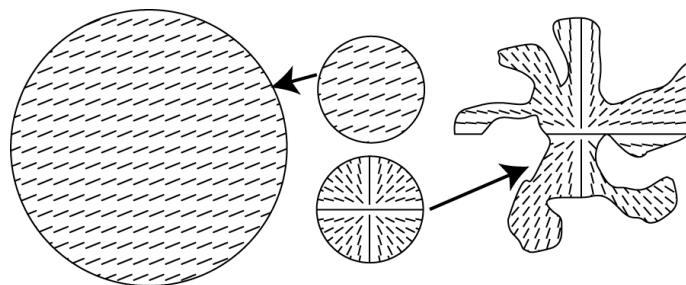


Figure 5.14 Illustration of the hypothesis about a nucleation core, in which the orientational texture of the nucleation core determines the orientational texture in the large domain at a later point.

more circular.[78, 79] The slow cooling of the DMPC domains, could potentially allow this rearranging to take place during the domain growth. It should however be noted that DPPC domains grown at an equally slow rate do not form round domains, or DMPC domains grown fast does not show flower liked domain shape, which is also evident from Figure 5.12.

One of the hypotheses, we have deduced from these experiments in order to explain the observations, is based on the effects of the nucleation core. We briefly touched this subject in section 5.7 regarding the texture of the early domains during the growth experiment. The nucleation core should be thought of as the smallest possible stable domain from which the rest of the domain will grow, thus it acts as a template for the rest of the domain growth, illustrated in Figure 5.14. This hypothesis is supported by the observed texture during the growth, as seen in Figure 5.10 and Figure 5.11, where the orientation of the domain does not change upon further growth and cooling of the domain. This would allow us to explain why the orientational texture is decoupled from the boundary conditions, since, as already described by Fisher et al., without any connection to the boundary conditions the uniform texture should be predominating. The observed texture could be explained through the energy of the nucleation core. The energy of the texture would then be minimized for the boundary of the likely roundish nucleation core; this will be further elaborated below.

The energy of the nucleation core is likely closely related to the nucleation density discussed in section 5.8. The lower the energy of the nucleation the more domains would nucleate, and once the nucleation cores are formed; it would always be more energetically favorable to expand an existing domain than nucleate new domains. One likely very important parameter for the energy of the nucleation core is the line tension, since a small domain would have a large perimeter to area fraction, and therefore a large line tension should result in low nucleation density. Regarding this point of view on line tension, the hydrophobic mismatch shows the same tendency. The DMPC mixtures with low hydrophobic mismatch have high nucleation densities (low energy nucleation cores), the DSPC mixtures have a large hydrophobic mismatch and low nucleation densities (high energy nucleation core),

with the DPPC domains lying between those. Those speculations however do not take into account the orientations as a parameter.

The orientation can be added to the equation by using it as a variation in the line tension. Fischer et al. solved this for the monolayer system by using a Fourier series, as was discussed in chapter 2.3, and arrived with the following expression, where E_i is the interfacial energy.[20]

$$E_i = \oint ds[\gamma - \Gamma_1 \bar{c} \cdot \bar{n} - \Gamma_2 (2(\bar{c} \cdot \bar{n})^2 - 1) \dots] \quad \text{Eq. 5.4}$$

In which, γ is the isotropic line tension, Γ are two constants related to the lipids, \bar{c} is the c-director of the lipids and \bar{n} is the vector for the normal to the boundary, as defined previously in Chapter 2.3. This implies that by ordering the lipid orientation, the interfacial energy of the domain can be lowered by effectively lowering the line tension. However one thing to consider is the fact that the line tension can never be zero or negative, which also applies for the interfacial energy. The energy gained by lowering the line tension should be compared with the energy cost of:

1. The disclination point(s) in the center of the domain
2. Defect lines
3. Bend and/or splay deformation of the hexatic grid

It is a reasonable assumption that the energy of those three is independent of the line tension and the hydrophobic mismatch. This means that the energy cost of forming the non-uniform texture is almost independent of the lipids in the mixture (for these experiments). This is not the case for the interfacial energy. Since the interfacial energy needs to be positive ($E_i > 0$) the mixtures with a higher isotropic line tension, can potentially gain more energy by ordering the lipid tails than the mixtures with low isotropic line tension. In other words the size of the line tension (γ) is a limiting factor on the Γ constants. As an example let, $\bar{c} \cdot \bar{n} = 0$, $\Gamma_1 > 0$ and $\Gamma_2 < 0$, thereby Eq. 5.4 simplifies to

$$0 < E_i = \oint ds[\gamma - \Gamma_1 - \Gamma_2] \Rightarrow \gamma > \Gamma_1 + \Gamma_2 \quad \text{Eq. 5.5}$$

In summary; the greater the isotropic line tension, the greater potential to reduce the interfacial energy by an ordering of the lipids at the phase boundary.

This makes it favorable for the DPPC and DSPC domains (IV-IX) to form the vortex like textures observed, since they have a high isotropic line tension due to a high hydrophobic mismatch.

This coupling between the isotropic line tension and the orientation matches well with the observations made. The DMPC domains have low hydrophobic mismatch, resulting in uniform textures, since the energy cost of the point disclination and bend/splay cannot be regained at the interface.

$$E_{i(\text{uniform})} = \oint ds[\gamma - \Gamma_1 \bar{c} \cdot \bar{n} - \Gamma_2 (2(\bar{c} \cdot \bar{n})^2 - 1)] = 2\pi r \cdot (\gamma) \quad \text{Eq. 5.6}$$

The DPPC and DSPC domains on the other hand have a high hydrophobic mismatch, meaning the energy cost can be regained at the interface resulting in the vortex like structure. This has an effect on the apparent line tension (γ_{app}), here calculated for a round domain (both \bar{c} and \bar{n} are assumed to be unit vectors)

$$\begin{aligned} E_{i(vortex)} &= \oint ds[...] = 2\pi r \cdot (\gamma - \Gamma_1 \cos(\varphi_{S0}) - \Gamma_2(2 \cos(\varphi_{S0})^2 - 1)) \\ &= 2\pi r \cdot \gamma_{app} \end{aligned} \quad \text{Eq. 5.7}$$

Where φ_{S0} is the offset angle calculated for the mixtures in Table 5.3. From this it follows that even though the isotropic line tension is higher for the DPPC and DSPC domains, due to the hydrophobic mismatch, the apparent line tension can theoretical be lower than the DMPC, due to the orientation of the lipids. If this is the case, it would explain why the DMPC shows domains shape characteristic for high line tension (round), whereas the DPPC and DSPC show flower like domain shapes, characteristic for a low line tension. The coupling between the line tension and the orientational texture thus explains both the observed textures and maybe the difference in the domain shapes. However it will be shown later in this section that different experiments make it unlikely that the effective line tension for the DMPC domain (I, II) is greater than the two others.

Following the assumption about concerning the nucleation core the growth of the domains can be divided into 4 different growth periods.

- **Nucleation** – Upon entering the co existing region the nucleation core is formed, showing either a continuously change of angle (DPPC, DSPC) or a uniform texture (DMPC). The texture is aligned with the boundary, and the shape is likely round or roundish. The size is hard to determine but likely very small, on the nm scale.
- **Early growth** – The domain grows and the texture is determined by the texture of the nucleation core, the continuously change of angle persist. The texture can theoretically be disconnected from the boundaries, since it is determined by the initial nucleation, the shape starts to show flower like tendencies (DPPC). The size for this state is still small, likely in the order of 1-5 μm .
- **Late growth** – The texture is still connected to the center, but instead of a continuously change of angle the domain is divided into subdomains with a preferred orientation within each. The subdomains are separated by defect lines as discussed in chapter 4.4. The flower shape is fully evolved for the DPPC and DSPC domains. The size is on the order of 10-20 μm
- **Late late growth of very large domains** – This late growth has only been observed for the DLPC DSPC mixture. A continuously change of angle in the outer part of the domain is observed, as seen in Figure 5.6. Furthermore the domains are very large 30+ μm .

It is important to again remember that the temperature changes through the different growth regions, which allows physical parameter to change. Regarding

the difference between the early and late growth we do not currently have an explanation for this, other than the change of temperature and domain size. However we have not been able to come up with a mechanism to explain this.

The discussion above differs in many ways from classical crystal nucleation theory in which the activation energy for a round domain spanning two bilayers is given by [100]

$$\Delta G^* = \frac{\pi\gamma^2 a}{2\Delta H} \frac{T_m}{T_m - T} \quad \text{Eq. 5.8}$$

Thereby the steady state nucleation rate (J) is:

$$J = j e^{-\left(\frac{\Delta G^*}{k_b T}\right)} \quad \text{Eq. 5.9}$$

Blanchette et al. [91] used this and plots similar to the ones shown in Figure 5.12 to calculate the line tension between the L_α and the L_β' phase, however instead of a cooling rate, as we did in Figure 5.12, they use “super cooling” ($T_m - T$) as the variable. With the system and experimental setup described in this thesis we have problems creating a “super cooling” situation, instead we see an immediately response upon lowering the temperature below the transition temperature. How the cooling rate rather than the “super cooling” works in those equations is not immediately clear. But by assuming the equation for the cooling rate is similar, it would mean, the greater the line tension the smaller the nucleation density. This implies that the line tension for the DSPC domain (VII-IX), is greater than the DPPC domains (IV-VI), which again is greater than the DMPC domains (I, II). In this case the line tension is likely the apparent line tension (γ_{app}) from Eq. 5.7

$$\gamma_{isotropic}(DMPC) < \gamma_{app}(DPPC) < \gamma_{app}(DSPC) \quad \text{Eq. 5.10}$$

This also matches well with the hydrophobic mismatch measured in Figure 5.8, it however reopens the question: why are the domains with the smallest line tension round? A question we currently are not able to answer!

The idea concerning the nucleation core description in the discussion above introduces an extra parameter not normally dealt with in classical nucleation theory, which is orientational texture and its coupling to the line tension. How this parameter could be introduced into the nucleation theory remains an unanswered question, which would be an interesting field for future studies.

Lastly the offset values calculated in section 5.4, with the result shown in Table 5.3, will be discussed. It is interesting to notice that each mixture give a constant value. This implies, as was also discussed in chapter 4, that the offset value is a physical parameter dependent on the lipids and/or the thermal history of the sample. The three DPPC mixtures (IV-VI) have values within a very narrow range, showing that the texture of the DPPC is invariant to the low melting temperature lipid. The DSPC mixtures (VII-IX) show two different populations. One mixture (VII) that is similar to the DPPC’s, and two mixtures (VIII, IX) that are closer to a pure splay result. The closer the offset value is to a pure splay, the

closer we are to a situation where normal boundary conditions are fulfilled for a round domain. Therefore it could imply that mixture VIII and IX have tendency to fulfill the normal boundary condition at the nucleation core. It would have been very useful to compare these results with measurement of the hydrophobic mismatch for the three DSPC mixtures, since there is a jump in the offset value for the DSPC mixture (VII-IX) and maybe a similar jump could have been found in the hydrophobic mismatch. But that is pure speculations.

5.11 Conclusion

The observations and discussion presented in this chapter have increased the knowledge of the complex behavior of domain and texture formation in a lipid bilayer. It was shown that there was a coupling between the hydrophobic mismatch and the observed texture. For samples with a low hydrophobic mismatch a uniform orientation of the lipids was observed. This was related to the energy of the nucleation core, and a relation between the hydrophobic mismatch and the line tension. An important lesson from these studies is that the mechanisms that govern the nucleation of the domains, is persistent in the much larger domains at a later time point and lower temperature. This effectively means the large macroscopic domains are a window into the parameter and behavior that govern nanoscopic domains as well. This effectively proves the essentiality of studies of model membrane system with respect to understanding domain formation, inhomogeneity, and phase separation in biological membranes and living cells.

Currently the importance of the offset value of the texture (section 5.4) is not completely understood, but it is very interesting that it is present, even in the very small domains, shortly after nucleation. Further work could be focused on the relations between this value, the hydrophobic mismatch, and the nucleation density. Such investigation could be very significant regarding energy calculations of nucleation cores, and therefore domain formation, and phase separation in biological membranes.

Chapter 6

Orientalional Texture in Monolayers

The Langmuir monolayer has always been a very popular model system, both as an experimental stage and as a theoretical study. The investigation of LC domains in a LE film have been intensely studied with BAM[34, 50-52, 66-69, 80, 101, 102] and polarized fluorescence microscopy[70-72], which permits real time measurements on monolayer films at the air-water interface. This facilitates the investigation of thermotropic phase transition between two condensed phases, in which the molecular orientation can be monitored, and thereby measuring the mechanism that controls the reorganizations of the condensed domains. [73, 74] Investigation of compression isotherms and x-ray diffraction data, has led to a detailed picture of domains and domain textures in monolayers. [22, 24, 25, 103] The possible orientational texture is preserved through a transfer to an air-solid interface, where the static monolayer system can be measured with techniques that allow a higher resolution, e.g. AFM which can allow the detection of individual surfactants, and thus can work as a complementary technique to x-ray scattering and diffraction.[104-108] With this diversity of instrumental techniques that allows detection of molecular orientation and ordering, the popularity of monolayer systems is expected. Undoubtedly investigation of monolayer systems analogous to the bilayer system could help explain the parameters that control the orientational texture exhibited by the bilayer domains.

In this chapter we will show how we found inspiration in the work of Sanchez et al.[81], to set up a Langmuir monolayer investigation, that should help us shed light on some of the aspect regarding the formation and pattern of the orientational texture exhibited by bilayer domains.

The first section will describe the motivation and work thesis for the work on monolayer. It will include proof of concept measurements of fluorescence microscopy on monolayers at the air-water (Section 6.1). The air-water interface will further be examined in Section 6.2 with the use of BAM. In Section 6.3 the transfer of the monolayer to a solid-air interface will be described, together with experiments regarding optimization of this procedure. Thereafter the orientational texture, at the solid-air interface, will be measured using AFM (Section 6.4) and polarized 2-photon fluorescence microscopy (Section 6.5). Lastly the obtained results will be discussed in Section 6.6.

6.1 Experimental Idea and Motivation

The measurements of orientational texture on phase co-existing bi-component monolayers using AFM by Sanchez et al.[81] bear many resemblances with the work described in the previous two chapters, with the significant difference being the system, i.e. monolayer vs. bilayer. They showed that DLPC, DSPC monolayers formed LC domains consisting of DSPC in a LE surrounding of DLPC. The LC domains exhibited an orientational texture that was maintained during transfer to a solid-air interface. The orientational texture at the air-water interface was measurable using BAM, however only texture for large domains could be observed (50 μm) due to the lateral resolution. The monolayers at the solid-air interface showed orientational texture in much smaller domains (5 μm), measured using AFM.

This inspired us to set up a similar system, in an attempt to gain insight into the observed orientational texture from the bilayer system, described in the previous chapter. The work with monolayers would allow us to investigate isothermally domain formation, since domains in monolayers are formed during a compression rather than a cooling, as also mentioned in chapter 2. This could prove pivotal in understanding the duality of many of the bilayer domains, e.g. DOPC, DPPC, where a continuously change of orientation in the center, and defect lines confining sub domains in the perimeter, is observed. As was discussed in chapter 4, this duality could perhaps be explained by the change of the hexatic stiffness and/or other elastic constant as a function of the temperature, since the center of the domain is formed at an elevated temperature compared to the outer part of the domain. Therefore the radial differences in the texture could be a consequence of the temperature range of the domain formation. Studies of similar monolayer domains could help determine the change of elastic constant by a shift in the observed texture from a continuously to a confined change of orientation, assuming a comparison between the elastic constants in monolayers and bilayers is possible.

6.1.1 Results: Fluorescence microscopy

Two monolayer systems were tested initially using fluorescence microscopy.

1. DLPC, DSPC (1:1)
2. DLPS, DPPC (1:1)

The first was chosen specifically in order to compare our techniques and ideas with the work of Sanchez et al,[81] since it is the same mixture they use. The second system was chosen since DPPC was the basis for the investigation of bilayers as described in chapter 4. For both of those systems compression isotherms were recorded, while fluorescence images were taken of the monolayer, doped with the fluorescence probe NBD. The results for both the samples are shown in Figure 6.1.

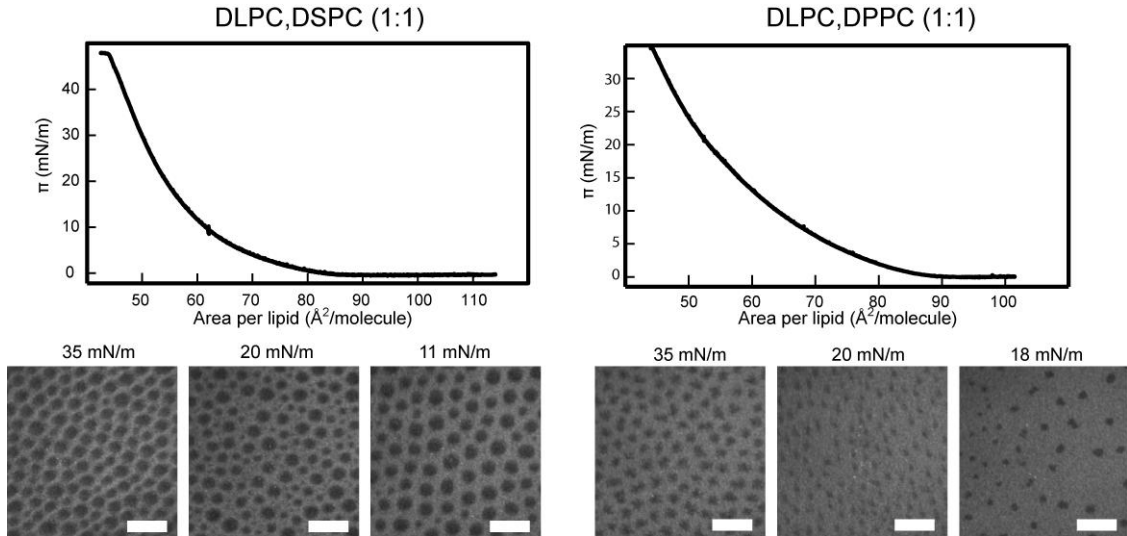


Figure 6.1 Isotherm (20°C) and selected fluorescence images for the two mixtures of DLPC,DSPC (1:1), and DLPC,DPPC (1:1) Scale bar is 30 μm . Recorded at U.C. Davis.

The DLPC, DSPC monolayer gave a very similar result as the work of Sanchez et al.[81] both in respect to the isotherm and the domain shapes observable in the fluorescence images. Sanchez et al. used BAM to investigate the domain formation during the compression, rather than fluorescence, but the observed features are very similar. The domains are present at even low surface pressures, but become closer packed and more distinct as the surface pressure increases. When the area was decreased, the surface pressure increases and, the monolayer will change in two ways. Firstly the domains will grow in size, secondly the area per lipid in the LE phase will decrease drastically, resulting in closer packed domains. [81]

The DLPC,DPPC isotherm is also shown in Figure 6.1. No distinct phase transition is observable in the phase diagram. At low surface pressures no domains are visible with the fluorescence microscopy. As the surface pressure increases, to about 18 mN/m, the domains start to appear, as seen in Figure 6.1. When the surface pressure is further increased the domains grow in size and are pushed closer together, see Figure 6.1.

6.2 Brewster Angle Microscopy

Brewster angle microscopy (BAM) is another way to monitor the domain formation in lipid monolayers during a compression. BAM has the advantage of being a probe free measurement, since the signal arises from a presence of the lipid monolayer itself, as was discussed in chapter 3. This removes any discussion concerning ‘contamination’ due to the fluorescent probe, eliminates ‘bleaching’, and obviates any considerations regarding choice of probe. In short a probe free microscopic technique is very advantageous. Furthermore it allows for the visualization of the internal order of the domains, since a difference in the orientation gives rise to a difference in the measured signal. However magnification is a limiting factor due to geometric constraints. The objective has to be positioned at the Brewster angle, and therefore the 50x, even with a SLWD (super long working distance) of 13.8 mm, cannot be moved close enough to be in focus without the objective being in contact with the water in the Langmuir trough. This means that 20x is the largest possible magnification attainable. BAM was used as a complementary technique to the fluorescence microscopy at the air-water interface. Both techniques allow the visualization of the domain formation during the compression, BAM further has the possibility to measure the internal orientational order of the domains.

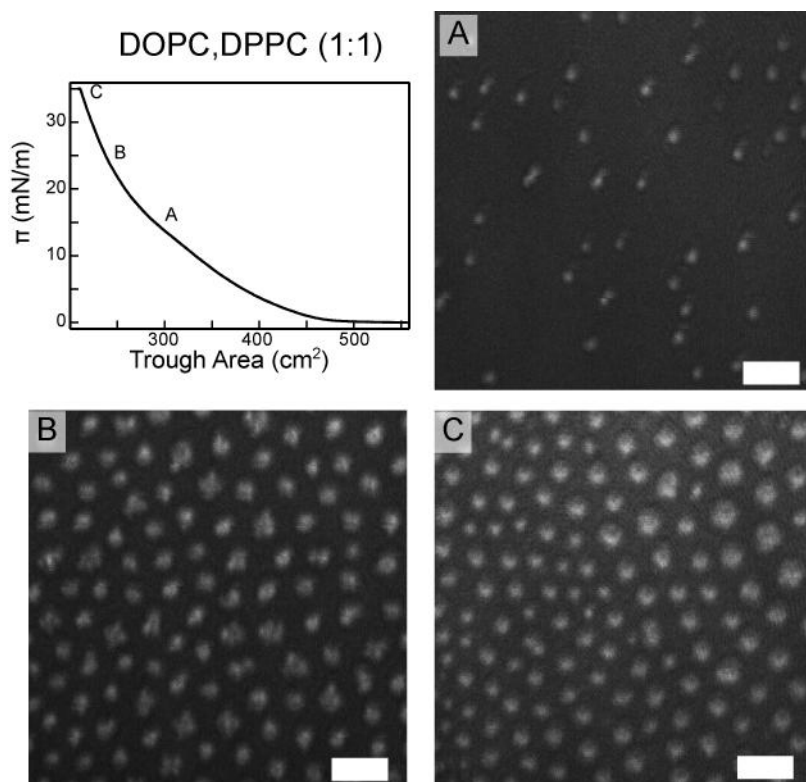


Figure 6.2 DOPC, DPPC (1,1) isotherm recorded at 20°C (A). BAM images have been recorded at different pressures corresponding to the graph, 14 mN/m(A), 24 mN/m(B) and 35 mN/m (C). The scale bar is 20 μ m.

6.2.1 Results: DOPC,DPPC mixture

The growth of LC domains in the DOPC,DPPC (1:1) monolayer was investigated using BAM, and the results, including the isotherm and BAM images during the compression, are shown in Figure 6.2. At a surface pressure of about 15 mN/m LC domains become visible in the BAM image (Figure 6.2A.), and the domains grew continually during the compression. The compression was terminated at 35 mN/m, at which point the LC domains were about 5-15 μm wide. The shape was hard to determine due to low resolution, and maybe small defocus, in the image. Likewise the internal orientational texture was not measurable, but it is evident that the intensity is inhomogeneous within the domains, which also makes the distinction of the domains circumference more difficult. These domains were compressed at the lowest speed attainable by the trough, which was 11.5 cm^2/min corresponding to about 1.5 $\text{\AA}^2/\text{min}/\text{molecule}$, it was therefore technically difficult to create larger domains, since connection between compression rate and domain sizes is evident. This made it necessary to transfer the monolayers to a solid-air interface that would allow the visualization with AFM. In this case domains of 5-15 μm in width would be an ideal size.

As previously described, the compression was halted at 35 mN/m, at which the software controlling the trough was set to maintain a constant surface pressure. However it should be noted from the isotherm in Figure 6.2 that at 35 mN/m a plateau occurs, at which the area is decreased but the surface pressure remains constant. This is not caused by a deposition onto a solid substrate or other external influence. Instead we believe it to be a sign of the instability of DOPC in the air-water interface. In general one should always be careful when working with monolayers of unsaturated compounds due to risk of oxidation. However monounsaturated fatty acid, and their corresponding phospholipids, can at least theoretically not be oxidized without a catalyst. Therefore we assume oxidation is not the problem. We presume the solubility in aqueous sub-phase to be the problem and that the DOPC are forming vesicles/micelles, however we have not been able to prove/disprove this hypothesis. Another possible explanation for the plateau is a relaxation of the monolayer. This means that mixtures containing DOPC are not ideal for monolayer studies. However we were able to form domains from the mixture of DOPC,DPPC, as is evident from the BAM images, indicating that the mixture could be used in the further experiments, but the actual mixture ratio between DOPC and DPPC, might vary from the initial deposited ratio (1:1).

6.2.2 Results: DLPC,DSPC mixture

The DLPC, DSPC mixture was also tested and the resulting isotherm and BAM images at three different temperatures are shown in Figure 6.3. The isotherms for the three temperatures, 20°C, 28°C, and 32°C, are slightly different. In general the entry into the LC phase, as indicated in the first rise of the

isotherm, is shifted towards higher areas for higher temperatures, which is as expected. This phase entry is at 84, 76, and 24 Å²/molecule for 32°C, 28°C, and 20°C respectively. The area difference at the final surface pressure of 35 mN/m is much smaller, which implies that the average slopes for the three temperatures are different, and that the slope of 20°C is steeper than the 28°C which again is steeper than the 32°C.

The BAM image of the 20°C monolayers, as seen in Figure 6.3A, reveals the shape of the domain to be mostly round, matching with the result from the previous subsection and the work of Sanchez et al.[81]. The round domain shape is not observed for the monolayers at elevated temperatures. For the 28°C monolayer, as seen in Figure 6.3B, the specific shape is hard to determine, because of the uneven intensities inside the domains, due to different orientations. The BAM images at 32°C, as seen in Figure 6.3C, show larger domains, with a more fractal character. The BAM image reveals only a weak indication of an internal orientational order, but this could be caused by the settings of the analyzer or another instrumental parameter.

6.2.3 Summary

The BAM technique proved that the DLPC,DSPC mixture was able to form DSPC domains in the LC-phase at different temperatures, which meant this

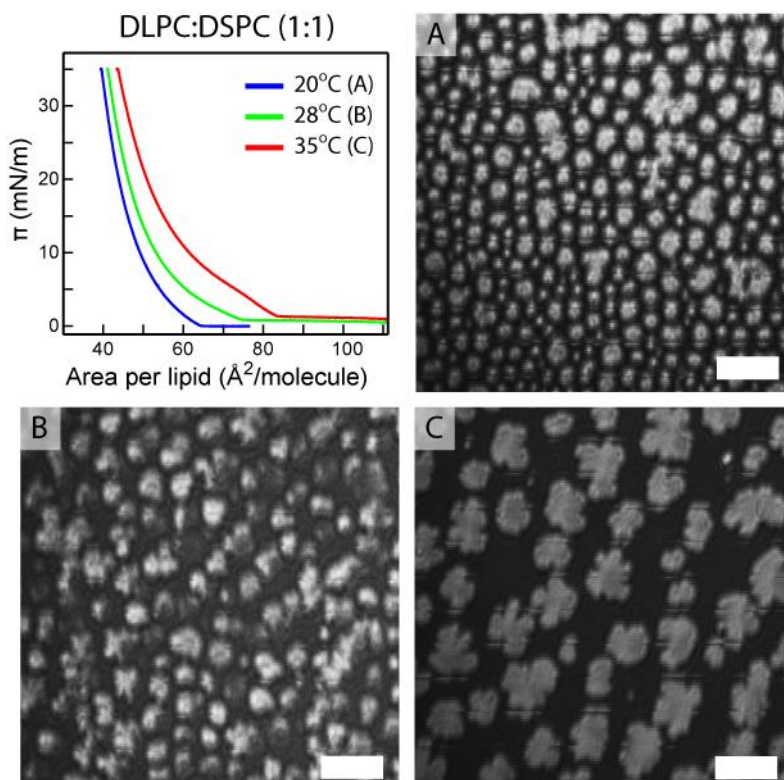


Figure 6.3 DLPC,DSPC (1:1) monolayers recorded at different temperatures. The BAM images have been recorded at 35 mN/m. The scale bar is 50 μm

mixture was suitable for the investigation of the effect of temperature on the elastic constant that govern the orientational texture. The orientational organization within the domains was not sufficiently detectable due to low lateral resolution. Likewise the monolayers of DOPC, DPPC showed domain formation, but the instability of the monolayer proved an issue. Therefore this mixture could be used with caution regarding the ratio of the mixture, and interpretation of the results.

6.3 Transfer of Monolayers to an Air-Solid Interface.

In order to investigate the orientational texture of the LC domains, they need to be transferred onto a solid substrate, and allowing investigation with higher lateral resolution than attainable with BAM. However the transfer of monolayers in a co-existing region from the air-water to an air-solid interface is not necessarily uncomplicated.

A classical way of transferring monolayers is the Langmuir Blodgett deposition technique. It involves a vertical sample being alternately lifted and dipped into the air-water interface, where each step involves the deposition of one monolayer.[21] Depending on whether the first step is a dip or a lift, the first monolayer will either have its head-region or tail-region in contact with the monolayer, see Figure 6.4A, however the hydrophobic/hydrophilic character of the substrate has to be considered as well. In this experiment, the tails should be exposed to the air to allow visualization of the orientational order, and thus the substrate is hydrophilic (mica), and the first and only step would be a lift. However as the lipids are deposited onto the substrate, the amount of lipids at the air-water interface decreases, and as a result the area of the trough should decrease in order to keep the lateral pressure constant during the deposition. Due to instrumental factors it is therefore best if the slope of the isotherm is steep ($\frac{d\pi}{dA} \gg 0$), since a small change in the amount of lipids have a large impact on the lateral pressure, and is measurable and adjustable mechanically. The Langmuir-Blodgett deposition

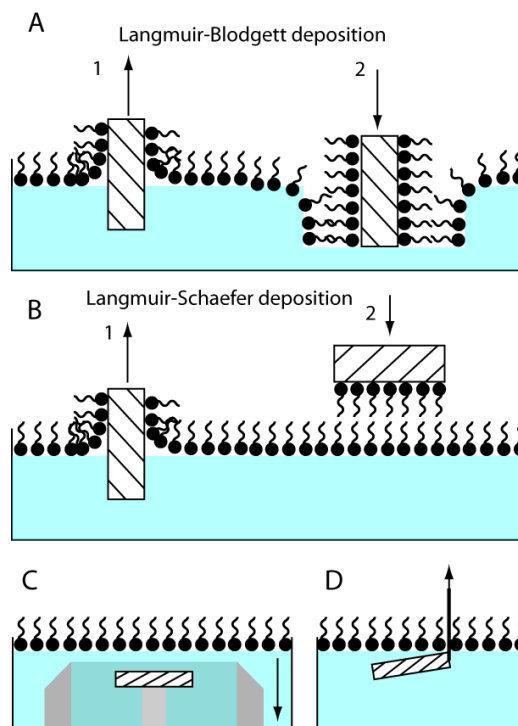


Figure 6.4 Illustrations of different deposition techniques. A) Langmuir-Blodgett, B) Langmuir-Schaefer, C) Inverse Langmuir-Schaefer, and D) the scooping up technique. The later have been used to create the samples investigated in this chapter.

technique has been proven able to maintain the orientational and positional order of monolayers [109-111], however since those experiments were done on single component films in a single phase configuration, it might not be applicable for the bi-component, phase co-existing monolayers used in this chapter.

Another possibility is to keep the substrate horizontal, see Figure 6.4B-D. This is a common procedure for producing bilayers, in which the first monolayer is deposited vertically, and the second monolayer is deposited horizontally. This method is called Langmuir-Schaefer, and can be seen in Figure 6.4B. To deposit a monolayer with the tails pointing towards the air interface onto a horizontal substrate two techniques can be used either the inverse Langmuir-Schaefer[112, 113], or the “scooping up” technique[114]. The inverse Langmuir-Schaefer is a bit more instrumentally taxing, as it involves the substrate being placed underwater in a ring/cage with a knife edge. To deposit the monolayer the sub-phase is lowered, initially beneath the knife edge of the ring, and subsequently beneath the substrate. The “scooping up” technique is more straight forward and involves the substrate being placed horizontally underneath the surface with a small tilt ($\approx 9^\circ$) to allow the runoff of the sub-phase. The substrate is then simply raised through the surface. Both techniques are illustrated in Figure 6.4C+D.

6.3.1 Experimental Comparison

The vertical deposition as well as the horizontal (scooping up) technique has been tried in order to determine which one, was most suitable for the monolayers in this project. The DLPC,DPPC mixture was a suitable system to test the transfer to a solid substrate due to the shape of the domains, since any deformation would be easily recognizable in the “starfish” shaped domains. After the transfer the monolayers were investigated using AFM, and can be seen in Figure 6.5. The vertical deposition, as seen in Figure 6.5A, reveals a clear striped structure in the LE phase, likewise the domains also seem to stretch in the same direction as the stripes. The stripes are parallel with the monolayer surface in the trough clearly proving to be an artifact of the deposition method. This artifact is likely caused by fluctuation in the surface pressure locally at the sample during the deposition, in which the compression tries to keep up with the pace of the removal of surfactant. The

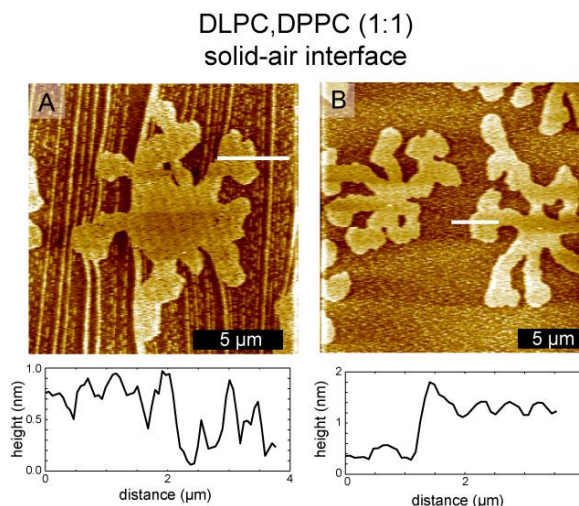


Figure 6.5 AFM images of DLPC,DPPC (1:1) monolayer on mica substrate. Transferred from monolayers at 20°C using two different techniques: vertical deposition (A) and horizontal/scoop deposition (B). Recorded at UC. Davis.

horizontal deposition, as seen in Figure 6.5B, proves to be much better, and the domain shapes are more coincident with the domain shapes observed with the fluorescence microscopy, as seen in Figure 6.1. This was not unexpected since transfer of monolayers in the co-existing region in the literature is done using a horizontal approach.[81, 84, 114]

The “scooping up” technique was also used to test the transfer of monolayers with the DLPC,DSPC mixture. The transferred monolayer was imaged using AFM, and the result is shown in Figure 6.6. The round domain shape is coinciding with the domain shape at the air-water interface, as seen in Figure 6.1, and no deformation is observed. The height difference between the LC domains of DSPC and the LE surrounding of DLPC was measure to approximately 1.2 nm, which is a higher value than the 0.7 nm reported by Sanchez et al.[81] This difference likely arises from a deformation of the LE-phase as a consequence of scanning at a too high force.

All monolayers were transferred at 35 mN/m, due to the precedent set by Sanchez et al.[81] The solid support was mica.

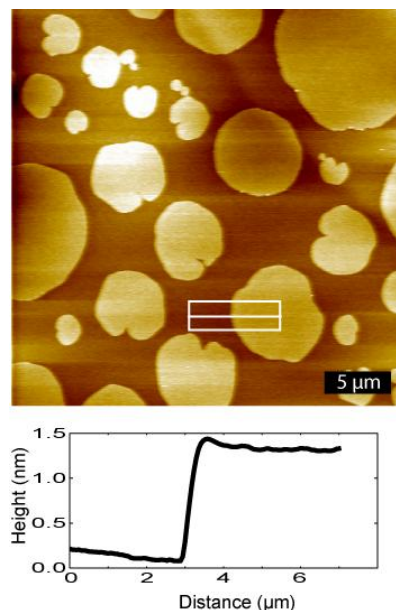


Figure 6.6 AFM images of DLPC, DSPC (1:1) monolayer on mica substrate. Transferred from monolayers at 20°C horizontal deposition. The white box represents the area of which the average is plotted as a line scan below. Recorded at UC. Davis.

6.4 AFM Friction Reveals Orientational Texture in Monolayers

The orientational texture of the LC domains on a solid substrate, e.g. mica, can be measured using contact-mode AFM, in which the texture is measurable as a friction force.[83, 84, 115-118] In contact-mode AFM, as described in chapter 3, the tip is in contact with the sample during the entire scan. Therefore, as illustrated in Figure 6.7, the tip is dragged across the sample and the local friction can be measured as a twist of the cantilever, and thereby a deviation in the lateral signal from the photodiode. This signal is greatly enhanced by scanning at high speed ($\approx 200 \mu\text{m/s}$), which unfortunately result in height images of poor quality. This technique is not very sensitive to continuous change in orientation of the lipid acyl tail, and is most efficient at detecting the line defects between subdomains with different orientations.

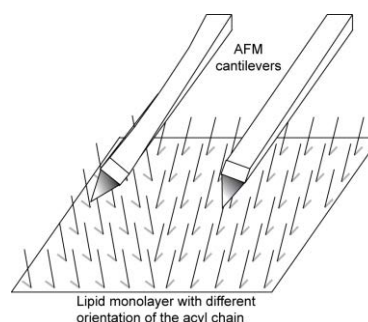


Figure 6.7 The orientational texture can be measured using AFM friction mode. Since the tail orientation will affect the friction between the cantilever and the sample and thereby the lateral deflection of the laser.

Sanchez et al. used tapping-mode AFM to measure the orientational texture of monolayers. This was made possible by a tilt of the cantilever in respect to the plane of the monolayer, thus making the interaction between the cantilever tip and the monolayer dependable on the orientation of the lipid acyl tails, and thus attainable from the phase image.[81]

The monolayers investigated by AFM were the following two mixtures DLPC,DSPC 1:1 and DOPC,DPPC 1:1. The monolayers were compressed at about $1.5\text{-}2 \text{ \AA}^2/\text{min}/\text{molecule}$ to the final surface pressure of 35 mN/m , followed by at least 20 min of equilibrium time, before the transfer to mica. As described above, the transfer was carried out using a horizontal “scooping up” technique. They were prepared at both 20°C and 32°C . Some samples were stained with the fluorescence dye DiI, to allow for a quick visualization of the transferred films. The shown AFM image of monolayers have been recorded on monolayers without any fluorescence dyes.

6.4.1 Results: DLPC,DSPC 1:1 20°C

The result is shown in Figure 6.8, where the friction image is shown for two domains (A+B). Figure 6.8E shows a fluorescence image of a sample after the transfer to the mica substrate. It is clearly seen that the domain shapes fall into two types, round or kidney shaped. Defect lines are clearly visible from the AFM image in all domains observed. They are divided into two categories. 1) Central point defects (Figure 6.8A) and 2) Point defect at the edge of the domains, so called Boojum[119] (Figure 6.8B). A line scan of the boojum structure is shown in

DLPC, DSPC (1:1) at 20°C

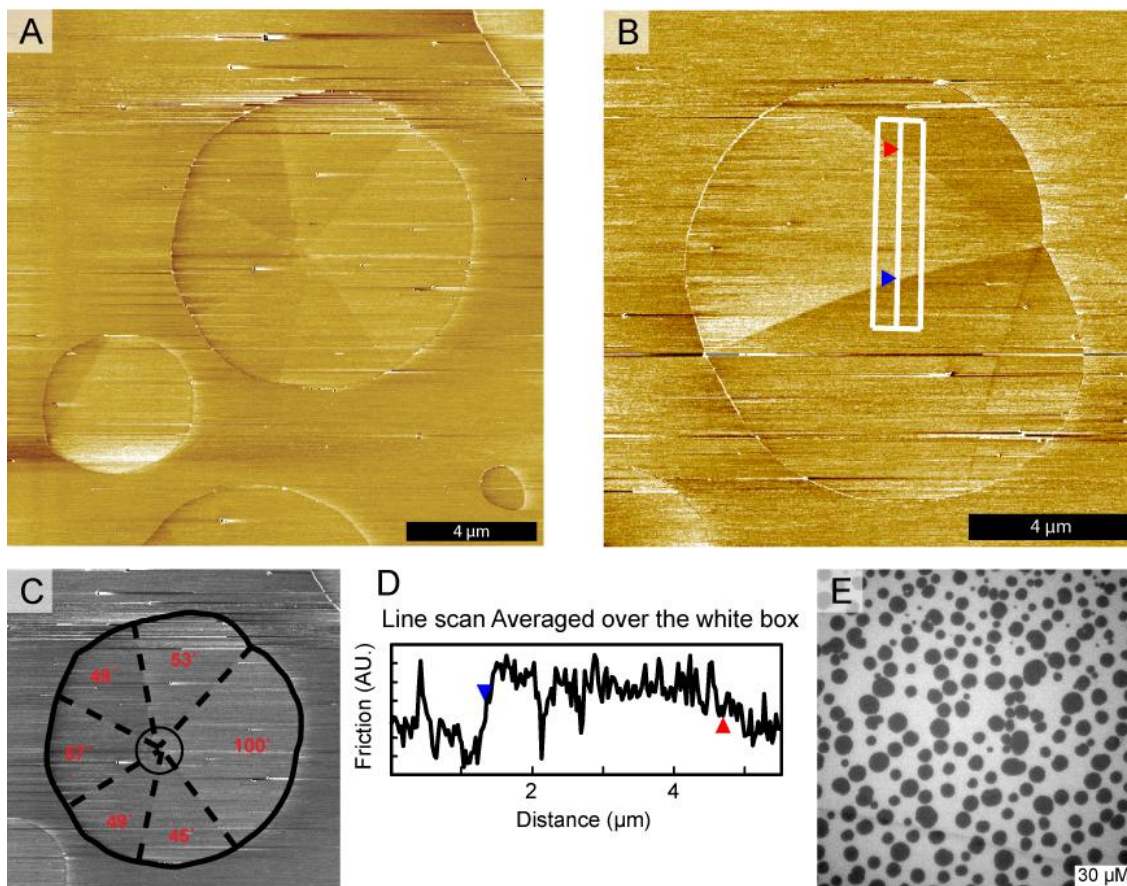


Figure 6.8 AFM friction images on DLPC, DSPC (1:1) monolayers on a solid substrate of mica. Transferred from a monolayer ($\eta=35$ mN/m at 20°C.) The domains are round or kidney shaped. Defect lines are clearly visible in all of them, and generally fall into two categories. 1) Central point defects (A) and 2) Boojum (B) with the point defect at the edge of the domains. For the central point defect (B) the defect lines are generally straight or slightly counterclockwise curved, they have been drawn in C, where the domain is divided into 5 small subdomains, with an angle between the defect line of about 45°-55°, and 1 large subdomain with an angle of 100°. The Boojum structures have fewer visible defect lines, 2-4 are normally observed resulting in 3-5 subdomains. The line scan (D) shows the average of the line within the white box in B, the two defect lines in the line scan is presented with the colored markers. E shows a fluorescence image of a larger area of the sample.

Figure 6.8D, the line scan intersect two defect lines. As the line scan indicates, the contrast between the different subdomains is not great, however in the AFM image (Figure 6.8B) they are clear and visually recognizable, hence demonstrating that this technique is usable for identifying the defect lines in monolayer domains. For the domain with the central point defect the defect lines are generally straight or slightly counterclockwise curved. In Figure 6.8A 6 defect lines are observed corresponding to 6 subdomains. Those defect lines are marked in Figure 6.8C, furthermore the angles between the defect lines are shown in the image. It is very interesting to notice that 5 out of the 6 lies within a range of 45°-57° while the last one is 100°, and this is not an unique observation. Sanchez et al. who used the same monolayer system and also used

DLPC,DSPC (1:1) at 32°C

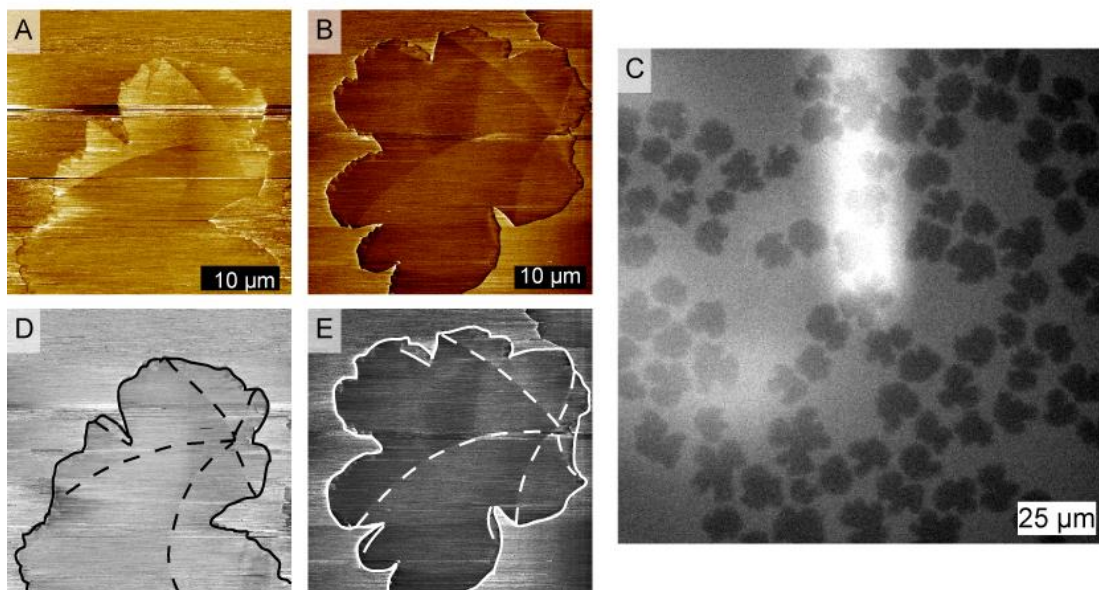


Figure 6.9 AFM friction images on DLPC, DSPC (1:1) monolayers on a solid substrate of mica, Transferred from a monolayer ($\pi=35$ mN/m at 32°C.) (A,B). (C) Shows a fluorescence wide field image, the bright region is the reflection of the cantilever. The domains deviate from a round shape and are more fractal shaped, with rough edges. The point defect is found inside the domain but off center, 5 defect lines are connected to the center, and they are all curve counterclockwise (D,E). At the outer part small defect lines, disconnected from the center, are observed.

AFM to measure the orientational texture, had similar observations.[81] They speculated that in fact there could be 7 subdomains, with one defect line being invisible to the AFM. The boojum structures have fewer visible defect lines, 2-4 are normally observed resulting in 3-5 subdomains.

6.4.2 Results: DLPC,DSPC 1:1 32°C

The results are shown in Figure 6.9. The AFM friction image of two different domains (Figure 6.9A+B), and the defect structure for each domains is further highlighted in Figure 6.9D+E. A larger area is visible in the fluorescence image, which clearly shows that the two domains in Figure 6.9A+B is representative for the sample, at least regarding the shape.

The shape of LC domains are more rugged at 32°C compared to the round shapes observed at 20°C. The point defect is normally placed within the domain, but towards an edge. 5 defect lines are connected to the center, and they are all curved counterclockwise. At the outer part short defect lines, disconnected from the center, are observed.

6.4.3 Results: DOPC,DPPC 1:1 20°C

The results are shown in Figure 6.10. Three AFM friction images are shown (A-C) and a fluorescence image that shows a larger area (D). The shapes fall within three categories, round, kidney shaped, or rounded “flower like”

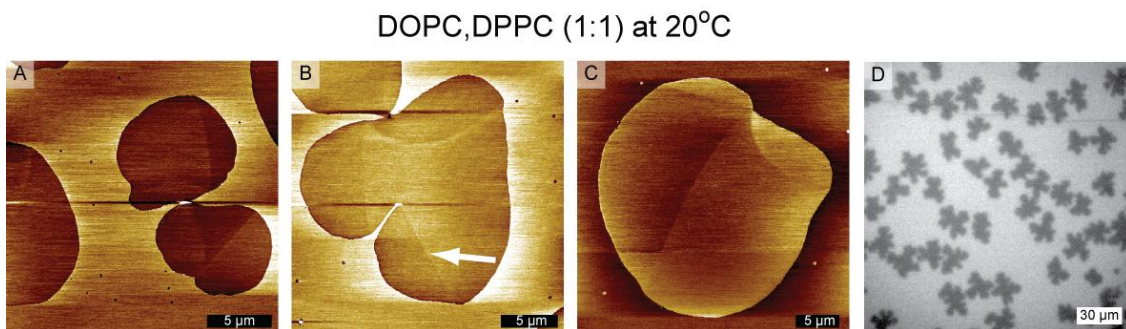


Figure 6.10 AFM friction images on DOPC, DPPC (1:1) monolayers on a solid substrate of mica. Transferred from a monolayer ($\pi=35$ mN/m at 20°C.) The domains are mostly round or kidney shaped, but other structures (B) are observed. The point defects are always located at the edge (boojum), and they generally have fewer defect lines, than the DSPC, DLPC domains. The defect lines are generally straight or lightly counterclockwise curved. Defect lines disconnected from the point defect is observed in several domains. D, shows a large area recorded with fluorescence wide field microscopy.

shaped. The point defects are always located at the edge (boojum), and they generally have fewer defect lines, than the DSPC, DLPC domains. The defect lines are generally straight or lightly counterclockwise curved. Defect lines disconnected from the point defect is observed in several domains, an example is the defect line marked by the white arrow in Figure 6.10B.

6.4.4 Results: DOPC,DPPC 1:1 32°C

This sample was attempted several times without any success. The reason for this is not completely well understood, since it was possible to compress the monolayer to 35 mN/m, but apparently something during the transfer to the solid substrate went wrong. It was found that the monolayer did not seem to be particularly stable, and the area was continuously decreased in order to maintain the same surface pressure. BAM images confirmed the presence of domains in the mixture, however the contrast were severely reduced, compared to same mixture at 20°C, which indicates something is amiss.

6.5 Polarized 2-photon Fluorescence on Monolayers

Another way to image the orientational texture of the monolayers at the air-solid interface is by using polarized 2 photon fluorescence microscopy as was used for the bilayers. This gives the advantage of measuring the absolute orientation, rather than the defect lines measured by the AFM, however this advantage comes at the cost of resolution. There was however a few problems related to this experiment.

One major problem was the birefringence nature of mica which was used as the substrate for the monolayers. Therefore it would be an advantage if it could be kept out of the optical pathway, as were the case for the bilayer setup described in chapter 3. This could be done by either using an air immersion objective and facing the monolayer towards the objective, or using a water immersion objective and a glass cover slip between the down facing sample and the water. Those two setups are shown in Figure 6.11A+B, though neither of them proved to be usable. The air immersion objective simply did not collect enough light, and the sandwich layered setup worked very poorly, due to the difference in refractive indexes of the water, glass, air, and sample sandwich. Therefore the use of the water objective directly onto the mica was necessary, which meant the birefringent mica was in the optical pathway.

In an attempt to cancel the effect of the mica, and thus ensure that the light that reaches the sample was linear polarized, a rotatable quarter wave plate (QWP) was added to the system already described in chapter 3. This meant the optical components, and their sequence, in the optical pathway is: Half wave plate (HWP), QWP, and lastly the mica. In order to evaluate whether the QWP would cancel the effect of the mica; an investigation of the polarization of the light through the optical pathway is needed. Therefore the Jones matrices for the system are presented below.[120]

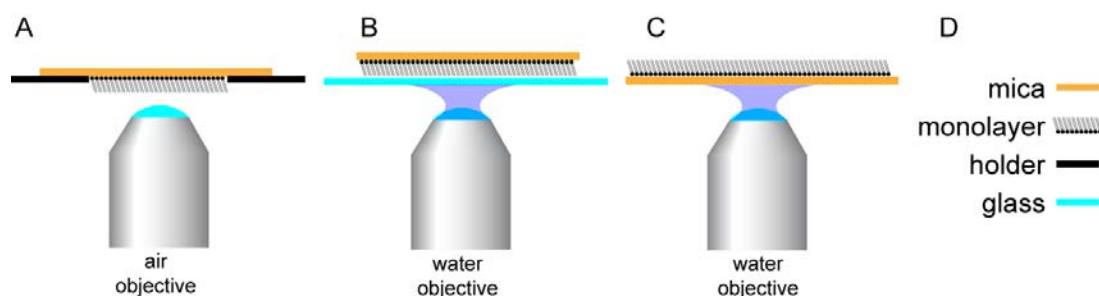


Figure 6.11 Three different approach toward image monolayers on a mica substrate using 2 photon polarized fluorescence microscopy. The two first describe setups that would avoid the birefringent mica in the optical pathway. A) using an air immersion objective, and B) using a water immersion objective in a sandwich layered build up. C) shows the actual setup used, due to problem with the two others. D) explains the different colors in the illustrations.

The initial light in the system is polarized light, which is given by the following Jones vector.

$$V_{light,in} = \begin{bmatrix} \cos(\alpha) \\ \sin(\alpha) \end{bmatrix} \quad \text{Eq. 6.1}$$

This is followed by a rotatable HWP, with an angle of φ_h . It is used to rotate the linear polarized light, while keeping it linear polarized.

$$M_{\frac{1}{2}\lambda\text{-plate}} = \begin{bmatrix} \cos(2\theta_h) & \sin(2\theta_h) \\ \sin(2\theta_h) & -\cos(2\theta_h) \end{bmatrix} \quad \text{Eq. 6.2}$$

The next element is the QWP, with an angle of θ_q . It will cause the light to be elliptic, or linear/circular which are both special cases of elliptic.

$$M_{\frac{1}{4}\lambda\text{-plate}} = \begin{bmatrix} \cos^2(\theta_q) + i\sin^2(\theta_q) & (1-i)\sin(\theta_q)\cos(\theta_q) \\ (1-i)\sin(\theta_q)\cos(\theta_q) & \sin^2(\theta_q) + i\cos^2(\theta_q) \end{bmatrix} \quad \text{Eq. 6.3}$$

Lastly we have the mica, here classified as a standard phase retarder. We have kept this Jones matrix simple by allowing it to define the axes of the system, i.e. the ‘x-axis’ of the system is set to be the fast axis of the mica.

$$M_{mica} = \begin{bmatrix} e^{i\varphi_{off,x}} & 0 \\ 0 & e^{i\varphi_{off,y}} \end{bmatrix} \quad \text{Eq. 6.4}$$

$$\Delta\varphi = \varphi_{off,y} - \varphi_{off,x} \quad \text{Eq. 6.5}$$

The difference in phase offset for the two directions in the mica can be determined, if we know the birefringence of mica. Özder et al. measured this and the result is redrawn in Figure 6.13A.[121]. The wavelength for the excitation light is 780 nm, and the corresponding birefringence is 0.023. For that wavelength the phase difference has been calculated as a function of the thickness (d) of the mica sheet, using the equation below. The result is plotted in Figure 6.13B.

$$\Delta\varphi = \frac{2\pi\Delta n}{\lambda}d \quad \text{Eq. 6.6}$$

The polarization of the light that reaches the sample is then given by:

$$\left(M_{\frac{1}{2}\lambda\text{-plate}} \cdot M_{\frac{1}{4}\lambda\text{-plate}} \cdot M_{Mica} \right) \cdot V_{light,in} = V_{light,out} \quad \text{Eq. 6.7}$$

Several features can be highlighted by examining the equations presented above. Firstly the best result is obtained if the QWP are either parallel or perpendicular with respect to the optical axes of the mica. Secondly, the idea of nullifying the effect of the mica only works if the mica itself function as QWP ($\Delta\varphi = \frac{\pi}{2}$), thereby the QWP can either nullify it or merge the two elements to a HWP, either way the result is linear polarized light. However if the mica works as a HWP the effect of the QWP is problematic, and for some orientation the resulting light will be circular polarized.

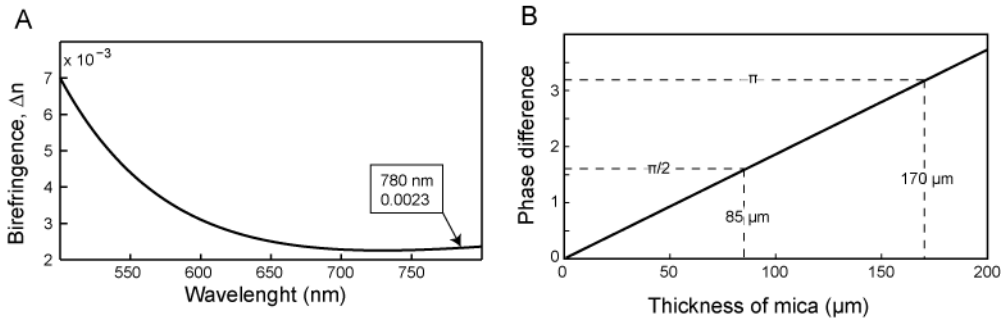


Figure 6.13 A) the birefringence of mica as a function of the wavelengths, the plot is made from Özder et al.'s data, the wavelength used in these experiments are 780 nm corresponding to a birefringence of 0.0023. B) the phase offset as a function of the thickness of the mica sheet. The values corresponding to a quarter wave plate and a half wave plate are marked.

In practice deviation from linear polarized light might be acceptable, since mica only works as a QWP (or HWP) for specific thickness, which has been marked in Figure 6.13B, for a QWP it is 85 μm and for HWP it is 170 μm . The mica sheets arrive 200 μm thick (hence the range of the graph), and are then cleaved resulting in a thickness below 200 μm . The cleaved mica substrates were tested in the setup before use to ensure the resulting light was close to linear polarized. The thickness range was tested numerically in a designed Matlab GUI, using the matrices presented above. The result of this analysis is shown in Figure 6.12. Both in experiments and in the numerical test a contrast of 1 to 5 was deemed acceptable. In Figure 6.12 it can be seen that this corresponds to phase differences of 1.2-1.9, which again is equivalent to thickness of 64-102 μm .

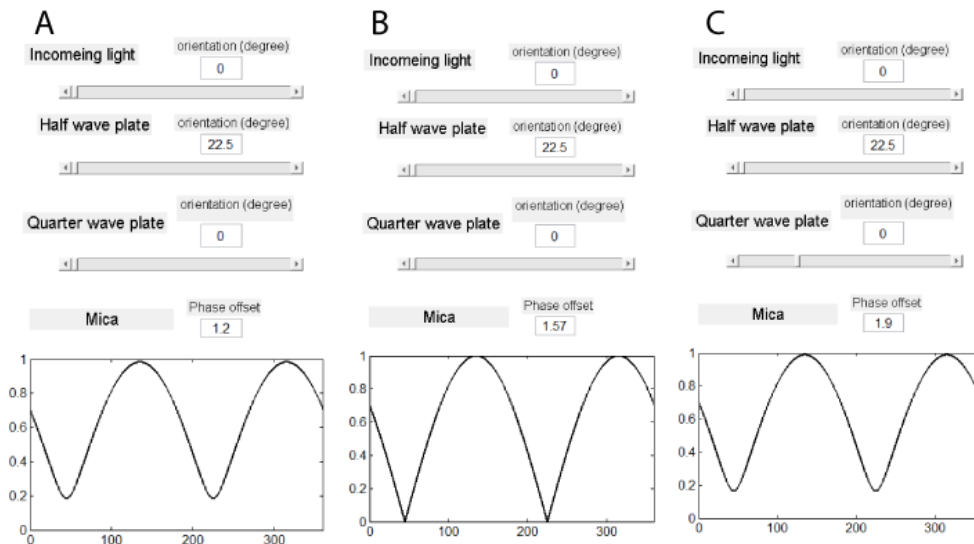


Figure 6.12 The resulting light intensity after it has passed a linear polarizer (analyser) for three different phase shifts of the mica. B, (1.57) works as a quarter wave plate, and the light is thus still linear polarized. A (1.2) and C (1.9) represent the min and max value allow for the mica to achieve an acceptable linear polarization.

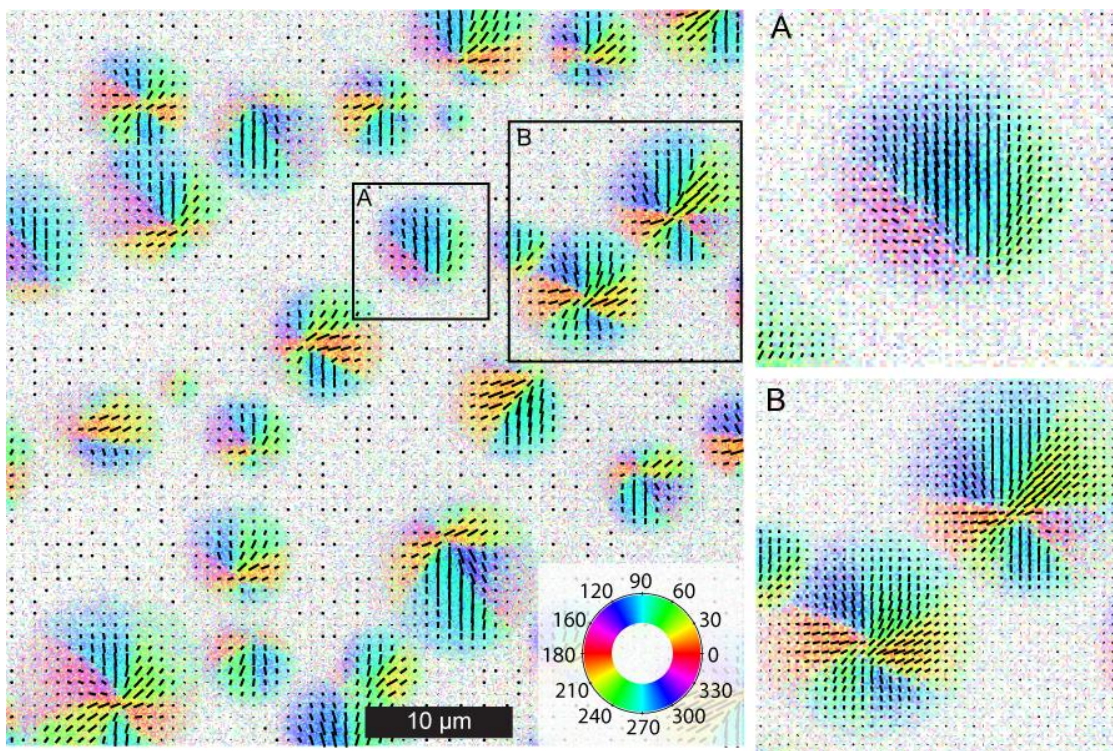


Figure 6.14 The orientational texture of DLPC:DSPC (1:1) monolayers on mica substrate transferred at 35 mN/m and 20°C. The lines and the color represent the orientation as seen in the inserted color scheme. A and B shows zoom of the marked regions.

This thickness range proved to be achievable experimentally.

As has already been mentioned the intensity of the fluorescence light from the Laurdan probe was an issue, and made the air immersion objective inadequate for these measurements. However even with the use of the water immersion objective, the intensity remained a problem. This was likely caused by the lack of water in the system, since water play a crucial role for the fluorescence of Laurdan[43-45]. Therefore it proved to be necessary with quite high concentration of the fluorescence probe Laurdan in order to achieve a sufficient signal to noise ratio during the image acquisition, which consist of several images of the same area. Therefore 5%, molar concentration, of Laurdan was added to the lipid sample, which proved to be sufficient for recorded a series of 9 images of the same area, after which the area was severely bleached. The effect of that high a concentration of Laurdan remains an untested question.

Only one sample have been recorded using polarized 2 photon fluorescence microscopy, which is the DLPC,DSPC (1:1) mixture, with the result shown in Figure 6.14, in which the recorded polarization scan has been converted into an orientation and a color, i.e. the same image analysis as described for the bilayers. These results show the same features described for the AFM measurements done on the same mixture, shown in Figure 6.8. Both LC domains with central point defects, and defects located at the interface are observed. The defect lines can again clearly be observed. But here the absolute orientations are observable, and

it is evident, that a normal boundary condition is preferable. For the domains with the central point defect, the majority are observed to have 6 subdomains; however few domains show indication of 7 subdomains, and one of them is shown in Figure 6.14B. This confirms the speculation by Sanchez et al. about 7 subdomains described previously in this chapter.[81]

6.6 Discussion

As mentioned in the beginning of this chapter, one of the major motivations for this investigation of orientational texture of bi-component monolayers was to compare the orientational texture, of monolayers, at different temperatures, with the bilayer measurements of the DOPC, DPPC (1:1) mixture. Unfortunately this particular mixture proved to be fairly difficult to work with in a monolayer system, likely due to the instability of the monolayer towards solubility in the subphase. We did manage to record samples at room temperature (20°C), but any attempt to transfer the monolayer at an elevated temperature failed.

The second mixture used in this chapter was monolayers consisting of DLPC, DSPC (1:1). This proved to be more amenable system, and we were able to produce sample at different temperatures, at which the orientational texture could be measured. The orientational texture of the bilayers domains of this mixture (DLPC, DSPC), were less unequivocal than the DOPC, DPPC mixture, both of which were described in chapter 5. Bilayer domains of the DLPC, DSPC mixture was divided into two population, both of which are schematized in Figure 6.15. One population had the same duality as the DOPC, DPPC mixture, with a continuously change of orientation at the center of the domain, and a division into subdomains confined by defect lines at outer part of the domains, see Figure 6.15A. The other population showed a continuously change of orientation for the entire domain, see Figure 6.15B. This made the DLPC, DSPC mixture less ideal regarding a comparison to the bilayer system.

The measured orientational texture of the DLPC, DSPC mixture transferred to the air-solid interface at 20°C showed a distribution of different defect patterns. The polarized 2-photon fluorescence microscopy measurement confirmed the expected normal boundary conditions. The defect patterns observed are identical to the ones reported by Sanchez et al.[81], and they fall within two categories, the point disclination at the center of the domains or at the edge of the domains (boojum), defect lines are observed for both groups. The split into two distinct populations indicates the energies of those two defect structures are of a

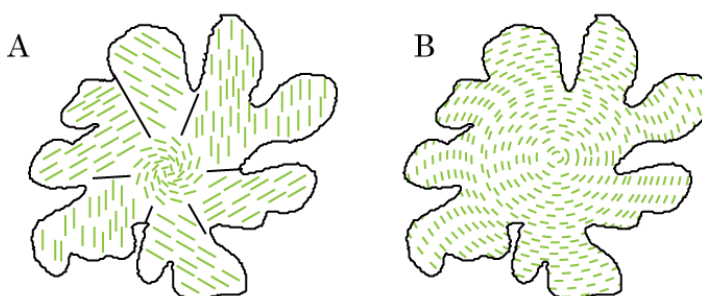


Figure 6.15 Illustration of two different orientational textures in bilayer domains, with subdomains in the outer part of the domains, and continuous change of orientation in the center (A), or a continuous change of orientation in the entire domains (B). The mixture of DLPC, DSPC in bilayers exhibit both texture, whereas DOPC, DPPC only form the first texture (A)

comparable order.

With inspiration from chapter 3.3 the energy of those two defect patterns can be compared, i.e. the Boojum and the central point defect. As a point of origin we will compare the Boojum observable in Figure 6.14A and the center defect in the lower left corner of Figure 6.14B, which are two domains of about equal size. As was shown in Eq. 2.31 the energy of a hexagonal domain with 6 defect line, the domain is shown in Figure 3.7, is given by:

$$E_{defects} = 6R_h\epsilon_0 \left(\frac{2K_1}{K_1 + K_3} \right) + 6R_h(\gamma - |\bar{\Gamma}_1| - \Gamma_2) + E_c(\text{defect lines}) \quad \text{Eq. 6.8}$$

$$E_{defects} = E_{defect-lines} + E_{boundary} + E_{core} \quad \text{Eq. 6.9}$$

Where R_h is the radius of a circles surrounding the hexagonal domains. The contribution to this is divided into three contributors, as seen in Eq. 6.8 and Eq. 6.9:

1. A contribution from the defect line, described as a line tension multiplied by the length of the defect lines.
2. The energy at the interface between the two phases, which is depend upon the orientation between the lipids and the boundary normal.
3. The energy of the point disclination.

By comparing the two domains (Figure 6.14A+B), the lengths of the defect lines are very close to identical, and being equal to 3 times the diameter of the domain. All the defect lines are splay wall, as discussed chapter 3, therefore the line tension of the defect wall must be identical. This means the first contributor to the energy is about equal for the two domains. When comparing the two domains at the phase interface it is evident that the normal boundary is more pronounced in the central defect domain (Figure 6.14B), in which each subdomain has a normal boundary condition. In the boojum case, the middle subdomain (the blue one) fulfills the normal boundary condition, whereas the other two (green and red) only partially fulfill it. This means the second energy contributor, i.e. the interface energy, is slightly higher for the boojum, however this is likely a minor difference. The last contributor, i.e. the point disclination, is different for those two, and are likely not directly comparable. However from the experiments we can conclude the total energy must be comparable, and as the two other contributors, i.e. defect lines and interface energy, the energy cost of the two point disclinations must be of a comparable size, maybe with the boojum being slightly higher, due to the difference in the interface energy.

The DLPC, DSPC monolayer at an elevated temperature, 32°C, showed a more uniform pattern of defect structures, with the point disclination inside the domain, but towards an edge. This means the similarity between the energy of the boojum and the central point defect is gone, clearly indicating a change of the physical parameter that governs the orientational texture. This proves the

feasibility of this setup, to detect changes in physical parameters induced by a change of temperature.

The domain shapes of the DLPC, DSPC mixture at 32°C, seen in Figure 6.9, are very interesting. They have a more rugged and irregular shape than the round domains observed at 20°C, this is of particular interest for two reasons. Firstly the domain shape roughly resembles the domain shape for the bilayer domains as shown in chapter 4 and 5, secondly, assuming splay texture around the point disclination, the normal boundary conditions are not completely fulfilled for the domains, and we see some decoupling between the orientational texture and the domain shape, again bearing resemblance to the bilayer domains. It should however be observed that the appearance of defect line disconnected from the center in the monolayer case, as observable in Figure 6.9D+E, could help keeping normal boundary conditions by introducing small extra subdomains. A better understanding of the orientational texture at this elevated temperature and especially its appearance during the compression could help the understanding of the decoupling between the texture and the domain shape of the bilayer domains.

Few relevant results were attained from the DOPC, DPPC monolayer system. There are several reasons for this, of which the most important has been mentioned several times, namely the stability of this particular monolayer. However the use of DPPC instead of the DSPC as the LC domain forming lipid might not be a trivial exchange. Firstly the DSPC, does not exhibit the LE, at least at 20°C, which means the phase transition from LE to LC does not happen during the compression,[81] this is not the case for DPPC. Secondly the monolayer experiment with DOPC, DPPC lacks, at least, two control experiments: 1. the isotherms and its corresponding phases for the two pure compounds, 2. an investigation of interactions between the two lipid components. The latter can be investigated by examining the average area per lipid for different mixtures. For an ideal mixing behavior the equation below holds true for any surface pressure[21]

$$a_{average} = a_1x_1 + a_2x_2 \quad \text{Eq. 6.10}$$

Where a is the area for the lipids and x is the mole fraction of that lipid. Any deviation from this rule indicates a non-ideal lipid-lipid interaction. Those control experiments would have helped clarify the different phases in the system, i.e. whether the observed domains are LC domains in a LE surrounding, and if there were other important interactions that should be considered, such as DOPC participation in the LC domains. Similar control experiments were carried out for the DLPC, DSPC mixture by Sanchez et al.[81], showing no deviation from ideal behavior.

6.7 Conclusion

In this chapter the various results regard monolayers have been presented. Bi-component monolayers in the co-existing phase region were showed to exhibit orientational order within the LC domains. This orientational order was shown to persist through a horizontal deposition onto a mica substrate. This allowed the measurement of the texture by both AFM and polarized 2-photon fluorescence microscopy. The initial monolayer system of DOPC,DPPC gave only limited results. Through the DLPC,DSPC mixture we were able to show the applicability of monolayer systems to investigate the effect of changes in temperature regarding orientational texture. Specifically we showed that DLPC,DSPC at 20°C showed two different patterns of the orientational texture, whereas only one was observed at 32°C.

The results presented here utilize only a fraction of the possibilities regarding comparing orientational texture in monolayers and bilayers. The ability to isothermally form ordered domains, and measure their orientational texture, allows for a minute mapping of the physical parameters in the temperature range of the bilayer domain formation. The monolayer system could also be used to measure thermotropic phase transition. This could allow a closer mimicking of the bilayer system in the experimental more accessible monolayer system.

Chapter 7

Conclusion

The main purpose of this thesis has been to investigate the orientational texture exhibited in lipid bilayer domains of the $L_{\beta'}$ phase. We wanted to heighten the knowledge of this rather complex phenomenon through systematic research. The orientational texture was measurable by the use of the fluorescence probe Laurdan and polarized 2-photon fluorescence microscopy.

This was started by a systematic search in bilayer domains of a single bi-component mixture, namely DOPC, DPPC. The $L_{\beta'}$ domains were found to have a complex texture that involved a division into subdomains. This division was only apparent in the outer part of the domain, where the subdomains were divided by defect lines. In the central region of the domains, around the nucleation point, a vortex-like texture with a continuously change of orientation was observed, together with two $m = 1/2$ point defects.

The difference between the inner and outer part of the domains, could potentially be caused by a change of the elastic constants during the non-isothermal growth of the domain. This was further investigated in a monolayer system, where domains can be grown isothermally. The monolayer system of DOPC, DPPC proved to be difficult to work with experimentally, due to an instability of the monolayer. The orientational textures were instead measured on LC domains in monolayers of DLPC, DSPC at an air-solid interface, by both AFM and 2-photon fluorescence microscopy. Through those measurements, we were able to show differences in the LC domain shape, and the orientational texture in monolayers compressed at different temperatures. We were however, unable to create LC domains without defect lines. Further work could be focused on a broader search regarding those. There is also an untapped potential in bi-component monolayers, and in this thesis, for instance, we did not investigate thermotropic induced phase transition in monolayer. Such work could perhaps help bridge the observations of orientational texture in bilayers and monolayers.

To better understand the orientational texture in lipid bilayers we preformed a broader investigation of several mixtures. These mixtures were made by combining three lipids with a low melting temperature (DOPC, POPC, and DLPC) and three lipids with a high melting temperature (DSPC, DPPC, and DMPC), with the latter three being the main component in the $L_{\beta'}$ domains. Since the difference between those three lipids is the tail length, the hydrophobic mismatch was the affected physical parameter. Many, but not all, of the mixtures formed $L_{\beta'}$ domains,

with the same distinctive features in the orientational texture as the DOPC,DPPC mixture. The two mixtures that formed $L_{\beta'}$ domains with DMPC, exhibited a uniform orientational texture (POPC,DMPC) or a nearly uniform texture (DOPC,DMPC). Those two mixtures also possessed the lowest hydrophobic mismatch ($< 1.0 \text{ nm}$). This was related to the energy of the nucleation core, and a relation between the hydrophobic mismatch and the line tension. Two of the mixtures that formed $L_{\beta'}$ domains with DSPC did not show any distinct division into subdomains, instead a continuously change of orientation was visible in the entire domain. Those two mixtures were DLPC,DSPC and POPC,DSPC mixtures,

For all the mixtures that exhibited a non uniform texture, the splay/bend character of the central vortex like structure was measured, quantified by an offset angle. This offset angle was found to be consistent within each mixture. Furthermore there seemed to be some similarities between the offset angle and content of the $L_{\beta'}$ domains, possibly related to hydrophobic mismatch. But further investigation is needed to fully enlighten this subject.

Investigation of the orientational texture during the domain formation revealed this vortex like texture to be present, in the domains recorded as close to the nucleation event as possible. No change of the vortex during the growth was observed. Since this vortex governs the orientational texture during the remaining domain formation, the nucleation core is in fact visible in the larger domain at a later point and lower temperature. This effectively means, the large domains are a window into the parameter and behavior that governs domain formation. This further highlights the possibility to gain insight regarding domain formation, inhomogeneity, and phase separation in biological membranes and living cells, through research on lipid model membranes.

Bibliography

1. Mouritsen, O.G., *Life - as a Matter of Fat* 2005: Springer.
2. Ipsen, J.H., G. Karlstrom, O.G. Mouritsen, H. Wennerstrom, and M.J. Zuckermann, *Phase-Equilibria in the Phosphatidylcholine-Cholesterol System*. *Biochimica Et Biophysica Acta*, 1987. **905**(1): p. 162-172.
3. van Meer, G., D.R. Voelker, and G.W. Feigenson, *Membrane lipids: where they are and how they behave*. *Nature Reviews Molecular Cell Biology*, 2008. **9**(2): p. 112-124.
4. Mouritsen, O.G. and M. Bloom, *Mattress Model of Lipid-Protein Interactions in Membranes*. *Biophysical Journal*, 1984. **46**(2): p. 141-153.
5. Heimburg, T., *Thermal Biophysics of Membranes* 2007: Wiley-vch.
6. Singer, S.J. and G.L. Nicolson, *The fluid Mosaic Model of the Structure of Cell Membranes*. *Science*, 1972. **175**(4023): p. 720-731.
7. Israelachvili, J.N., *Refinement of Fluid-Mosaic Model of Membrane Structure*. *Biochimica Et Biophysica Acta*, 1977. **469**(2): p. 221-225.
8. Simons, K. and E. Ikonen, *Functional rafts in cell membranes*. *Nature*, 1997. **387**(6633): p. 569-572.
9. Kusumi, A., C. Nakada, K. Ritchie, K. Murase, K. Suzuki, H. Murakoshi, R.S. Kasai, J. Kondo, and T. Fujiwara, *Paradigm shift of the plasma membrane concept from the two-dimensional continuum fluid to the partitioned fluid: High-speed single-molecule tracking of membrane molecules*, in *Annual Review of Biophysics and Biomolecular Structure* 2005, Annual Reviews: Palo Alto. p. 351-U54.
10. Simons, K. and M.J. Gerl, *Revitalizing membrane rafts: new tools and insights*. *Nature Reviews Molecular Cell Biology*, 2010. **11**(10): p. 688-699.
11. Elson, E.L., E. Fried, J.E. Dolbow, and G.M. Genin, *Phase Separation in Biological Membranes: Integration of Theory and Experiment*. *Annual Review of Biophysics*, 2010. **39**: p. 207-226.
12. Levental, I., M. Grzybek, and K. Simons, *Raft domains of variable properties and compositions in plasma membrane vesicles*. *Proceedings of the National Academy of Sciences of the United States of America*, 2011. **108**(28): p. 11411-11416.

13. Bagatolli, L.A., J.H. Ipsen, A.C. Simonsen, and O.G. Mouritsen, *An outlook on organization of lipids in membranes: Searching for a realistic connection with the organization of biological membranes*. Progress in Lipid Research, 2010. **49**(4): p. 378-389.
14. Simonsen, A.C. and L.A. Bagatolli, *Structure of spin-coated lipid films and domain formation in supported membranes formed by hydration*. Langmuir, 2004. **20**(22): p. 9720-9728.
15. Kubiak, J., J. Brewer, S. Hansen, and L.A. Bagatolli, *Lipid Lateral Organization on Giant Unilamellar Vesicles Containing Lipopolysaccharides*. Biophysical Journal, 2011. **100**(4): p. 978-986.
16. Bernchou, U., J. Brewer, H.S. Midtby, J.H. Ipsen, L.A. Bagatolli, and A.C. Simonsen, *Texture of Lipid Bilayer Domains*. Journal of the American Chemical Society, 2009. **131**(40): p. 14130-+.
17. Fidorra, M., L. Duelund, C. Leidy, A.C. Simonsen, and L.A. Bagatolli, *Absence of fluid-ordered/fluid-disordered phase coexistence in ceramide/POPC mixtures containing cholesterol*. Biophysical Journal, 2006. **90**(12): p. 4437-4451.
18. Plasencia, I., L. Norlen, and L.A. Bagatolli, *Direct visualization of lipid domains in human skin stratum corneum's lipid membranes: Effect of pH and temperature*. Biophysical Journal, 2007. **93**(9): p. 3142-3155.
19. Grassme, H., J. Riethmuller, and E. Gulbins, *Biological aspects of ceramide-enriched membrane domains*. Progress in Lipid Research, 2007. **46**(3-4): p. 161-170.
20. Fischer, T.M., R.F. Bruinsma, and C.M. Knobler, *Textures of surfactant monolayers*. Physical Review E, 1994. **50**(1): p. 413-428.
21. Petty, M.C., *Langmuir-Blodgett Films - an introduction*1996: Cambridge University press.
22. Iñes-Mullol, J., J. Claret, R. Reigada, and F. Sagues, *Spread monolayers: Structure, flows and dynamic self-organization phenomena*. Physics Reports-Review Section of Physics Letters, 2007. **448**(5-6): p. 163-179.
23. Weis, R.M. and H.M. McConnell, *Two-Dimensional Chiral Crystals of Phospholipid*. Nature, 1984. **310**(5972): p. 47-49.
24. Knobler, C.M. and R.C. Desai, *Phase-Transitions in monolayers*. Annual Review of Physical Chemistry, 1992. **43**: p. 207-236.
25. Kaganer, V.M., H. Mohwald, and P. Dutta, *Structure and phase transitions in Langmuir monolayers*. Reviews of Modern Physics, 1999. **71**(3): p. 779-819.

26. Chandrasekhar, S., *Liquid Crystals*1992: Cambridge University Press.
27. Halperin, B.I. and D.R. Nelson, *Theory of 2-dimensional melting*. Physical Review Letters, 1978. **41**(2): p. 121-124.
28. Kosterlitz, J.M. and D.J. Thouless, *Ordering, Metastability and phase-transitions in 2 dimensional systems*. Journal of Physics C-Solid State Physics, 1973. **6**(7): p. 1181-1203.
29. Nelson, D.R. and B.I. Halperin, *Dislocation-Mediated melting in 2 dimensions*. Physical Review B, 1979. **19**(5): p. 2457-2484.
30. Kosterlitz, J.M. and D.J. Thouless, *Long-Range Order and Metastability in 2-Dimensional Solids and Superfluids*. Journal of Physics Part C Solid State Physics, 1972. **5**(11): p. L124-+.
31. Watkins, E.B., C.E. Miller, D.J. Mulder, T.L. Kuhl, and J. Majewski, *Structure and Orientational Texture of Self-Organizing Lipid Bilayers*. Physical Review Letters, 2009. **102**(23): p. 4.
32. Nelson, D.R. and B.I. Halperin, *Solid and Fluid Phases in Smectic Layers with Tilted Molecules*. Physical Review B, 1980. **21**(11): p. 5312-5329.
33. Selinger, J.V. and D.R. Nelson, *Theory of Transitions among Tilted Hexatic Phases in Liquid-Crystals*. Physical Review A, 1989. **39**(6): p. 3135-3147.
34. Henon, S. and J. Meunier, *Phase-Transitions in Gibbs Films - Star Textural Defects in Tilted Mesophases*. Journal of Chemical Physics, 1993. **98**(11): p. 9148-9154.
35. Nagle, J.F. and D.A. Wilkinson, *Diatometric Studies of the Sub-Transition in Dipalmitoylphosphatidylcholine*. Biochemistry, 1982. **21**(16): p. 3817-3821.
36. Bernchou, U., H. Midtby, J.H. Ipsen, and A.C. Simonsen, *Correlation between the ripple phase and stripe domains in membranes*. Biochimica Et Biophysica Acta-Biomembranes, 2011. **1808**(12): p. 2849-2858.
37. Pabst, G., S. Danner, S. Karmakar, G. Deutsch, and V.A. Raghunathan, *On the propensity of phosphatidylglycerols to form interdigitated phases*. Biophysical Journal, 2007. **93**(2): p. 513-525.
38. Cevc, G. and D. Marsh, *Phospholipid bilayers: Physical principles and models*1987: Wiley interscience
39. Davis, P.J. and K.M.W. Keough, *Phase diagrams of bilayers of dimyristoyl lecithin plus heteroacid lecithins*. Chemistry and physics of Lipids, 1984. **35**(4): p. 299-308.

40. Furuya, K. and T. Mitsui, *Phase-transitions in Bilayer Membranes of Dioleoyl-Phosphatidylcholine-Dipalmitoyl-Phosphatidylcholine*. Journal of the Physical Society of Japan, 1979. **46**(2): p. 611-616.
41. Murphy, D.B., *Fundamentals of Light Microscopy and Electronic Imaging* 2001: Wiley-Liss.
42. Bestvater, F., E. Spiess, G. Stobrawa, M. Hacker, T. Feurer, T. Porwol, U. Berchner-Pfannschmidt, C. Wotzlaw, and H. Acker, *Two-photon fluorescence absorption and emission spectra of dyes relevant for cell imaging*. Journal of Microscopy-Oxford, 2002. **208**: p. 108-115.
43. Parasassi, T., G. De Stasio, A. Dubaldo, and E. Gratton, *Phase Fluctuation in Phospholipid-Membranes Revealed by Laurdan Fluorescence*. Biophysical Journal, 1990. **57**(6): p. 1179-1186.
44. Bagatolli, L., E. Gratton, T.K. Khan, and P.L.G. Chong, *Two-photon fluorescence microscopy studies of bipolar tetraether giant liposomes from thermoacidophilic archaeobacteria Sulfolobus acidocaldarius*. Biophysical Journal, 2000. **79**(1): p. 416-425.
45. Parasassi, T., E. Gratton, W.M. Yu, P. Wilson, and M. Levi, *Two-photon fluorescence microscopy of Laurdan generalized polarization domains in model and natural membranes*. Biophysical Journal, 1997. **72**(6): p. 2413-2429.
46. Bopp, M.A., Y. Jia, G. Haran, E.A. Morlino, and R.M. Hochstrasser, *Single-molecule spectroscopy with 27 fs pulses: Time-resolved experiments and direct imaging of orientational distributions*. Applied Physics Letters, 1998. **73**(1): p. 7-9.
47. Magonov, S.N. and M. Whangbo, *Surface analysis with STM and AFM - experimental and theoretical aspects of image analysis* 1996: Wiley - VCH.
48. Simonsen, A.C., *Cantilever-based microscopy and spectroscopy, Notes for KE84*, 2006.
49. Goldstein, D., *Polarized Light*, ed. 2nd 2003, New York: Marcel Dekker inc.
50. Overbeck, G.A., D. Honig, L. Wolthaus, M. Gnade, and D. Mobius, *Observation of Bond-Orientational order in floating and transferred monolayers with Brewster-angle Microscopy*. Thin Solid Films, 1994. **242**(1-2): p. 26-32.
51. Weidemann, G. and D. Vollhardt, *Long-Range Tilt Orientational order in Phospholipid Monolayers - A Comparison of the Order in the Condensed Phases of Dimyristoylphosphatidylethanolamine and Dipalmitoylphosphatidylcholine*. Colloids and Surfaces A, 1995. **100**: p. 187-202.

52. Weidemann, G. and D. Vollhardt, *Long-range tilt orientational order in phospholipid monolayers: A comparative study*. Biophysical Journal, 1996. **70**(6): p. 2758-2766.
53. Brian, A.A. and H.M. McConnell, *Allogeneic Stimulation of Cyto-Toxic T-Cells by Supported Planar Membranes*. Proceedings of the National Academy of Sciences of the United States of America-Biological Sciences, 1984. **81**(19): p. 6159-6163.
54. Watts, T.H., A.A. Brian, J.W. Kappler, P. Murrack, and H.M. McConnell, *Antigen Presentation by Supported Planar Membranes Containing Affinity-Purified I-AD*. Proceedings of the National Academy of Sciences of the United States of America-Biological Sciences, 1984. **81**(23): p. 7564-7568.
55. Flack, W.W., D.S. Soong, A.T. Bell, and D.W. Hess, *A Mathematical-Model for Sping Coating of Polymer Resist*. Journal of Applied Physics, 1984. **56**(4): p. 1199-1206.
56. Mennicke, U. and T. Salditt, *Preparation of solid-supported lipid bilayers by spin-coating*. Langmuir, 2002. **18**(21): p. 8172-8177.
57. Jue, T., S.H. Risbud, M.L. Longo, and R. Faller, *Biomembrane Frontiers: Nanostructures, Models, and the Design of Life* 2009: Humana Press.
58. Ogunyankin, M.O., A. Torres, F. Yaghmaie, and M.L. Longo, *Lipid Domain Pixelation Patterns Imposed by E-beam Fabricated Substrates*. Langmuir, 2012. **28**(18): p. 7107-7113.
59. Bernchou, U., J.H. Ipsen, and A.C. Simonsen, *Growth of Solid Domains in Model Membranes: Quantitative Image Analysis Reveals a Strong Correlation between Domain Shape and Spatial Position*. Journal of Physical Chemistry B, 2009. **113**(20): p. 7170-7177.
60. Dreier, J., J. Brewer, and A.C. Simonsen, *Texture defects in lipid membrane domains*. Soft Matter, 2012. **8**(18): p. 4894-4904.
61. Brock, J.D., R.J. Birgeneau, J.D. Litster, and A. Aharony, *Hexatic ordering in liquid-Crystal film*. Contemporary Physics, 1989. **30**(5): p. 321-335.
62. de Jeu, W.H., B.I. Ostrovskii, and A.N. Shalaginov, *Structure and fluctuations of smectic membranes*. Reviews of Modern Physics, 2003. **75**(1): p. 181-235.
63. Dierker, S.B., R. Pindak, and R.B. Meyer, *Consequences of bond-orientational order on the macroscopic orientation patterns of thin tilted hexatic liquid-crystal films*. Physical Review Letters, 1986. **56**(17): p. 1819-1822.

64. Pindak, R., C.Y. Young, R.B. Meyer, and N.A. Clark, *Macroscopic Orientation patterns in smectic-c films*. Physical Review Letters, 1980. **45**(14): p. 1193-1196.
65. Young, C.Y., R. Pindak, N.A. Clark, and R.B. Meyer, *Light-Scattering Study of 2-Dimensional Molecular-Orientation Fluctuations in a Freely Suspended Ferroelectric Liquid-Crystal*. Physical Review Letters, 1978. **40**(12): p. 773-776.
66. Weidemann, G., U. Gehlert, and D. Vollhardt, *Inner Structure of Condensed-Phase Domains in Monolayers at the Air-Water-Interface*. Langmuir, 1995. **11**(3): p. 864-871.
67. Honig, D. and D. Mobius, *Direct Visualization of Monolayers at the Air-Water-Interface by Brewster-Angle Microscopy*. Journal of Physical Chemistry, 1991. **95**(12): p. 4590-4592.
68. Henon, S. and J. Meunier, *Microscope at the Brewster-Angle - Direct Observation of 1st Order Phase-Transition in Monolayers*. Review of Scientific Instruments, 1991. **62**(4): p. 936-939.
69. Weidemann, G. and D. Vollhardt, *Long-Range Tilt Orientational order in Phospholipid Monolayers - The Inner Structure of Dimyristoyl-Phosphatidyl-Ethanolamine Domains*. Thin Solid Films, 1995. **264**(1): p. 94-103.
70. Moy, V.T., D.J. Keller, H.E. Gaub, and H.M. McConnell, *Long-range molecular orientational order in monolayer solid domains of phospholipid*. Journal of Physical Chemistry, 1986. **90**(14): p. 3198-3202.
71. Qiu, X., J. Ruizgarcia, K.J. Stine, C.M. Knobler, and J.V. Selinger, *Direct Observation of Domain-structure in Condensed Monolayer Phases*. Physical Review Letters, 1991. **67**(6): p. 703-706.
72. Ruizgarcia, J., X. Qiu, M.W. Tsao, G. Marshall, C.M. Knobler, G.A. Overbeck, and D. Mobius, *Splay Stripe Textures in Langmuir Monolayers*. Journal of Physical Chemistry, 1993. **97**(27): p. 6955-6957.
73. Schwartz, D.K. and C.M. Knobler, *Direct Observations of Transitions between Condensed Langmuir Monolayer Phases by Polarized Fluorescence Microscopy*. Journal of Physical Chemistry, 1993. **97**(35): p. 8849-8851.
74. Fischer, B., M.W. Tsao, J. RuizGarcia, T.M. Fischer, D.K. Schwartz, and C.M. Knobler, *The blooming transition in Langmuir monolayers and its microscopic origin*. Thin Solid Films, 1996. **284**: p. 110-114.
75. Kjaer, K., J. Alsnielsen, C.A. Helm, L.A. Laxhuber, and H. Mohwald, *Ordering in lipid Monolayers studied by synchrotron X-ray-diffraction and fluorescence microscopy*. Physical Review Letters, 1987. **58**(21): p. 2224-2227.

76. Ziblat, R., L. Leiserowitz, and L. Addadi, *Crystalline Lipid Domains: Characterization by X-Ray Diffraction and their Relation to Biology*. *Angewandte Chemie-International Edition*, 2011. **50**(16): p. 3620-3629.
77. Watkins, E.B., C.E. Miller, J. Majewski, and T.L. Kuhl, *Membrane texture induced by specific protein binding and receptor clustering: active roles for lipids in cellular function*. *Proceedings of the National Academy of Sciences of the United States of America*, 2011. **108**(17): p. 6975-6980.
78. Longo, M.L. and C.D. Blanchette, *Imaging cerebroside-rich domains for phase and shape characterization in binary and ternary mixtures*. *Biochimica Et Biophysica Acta-Biomembranes*, 2010. **1798**(7): p. 1357-1367.
79. Blanchette, C.D., C.A. Orme, T.V. Ratto, and M.L. Longo, *Quantifying growth of symmetric and asymmetric lipid bilayer domains*. *Langmuir*, 2008. **24**(4): p. 1219-1224.
80. Iignes-Mullol, J., J. Claret, and F. Sagues, *Star defects, boojums, and cardioid droplet shapes in condensed dimyristoylphosphatidylethanolamine monolayers*. *Journal of Physical Chemistry B*, 2004. **108**(2): p. 612-619.
81. Sanchez, J. and A. Badia, *Spatial variation in the molecular tilt orientational order within the solid domains of phase-separated, mixed dialkylphosphatidylcholine monolayers*. *Chemistry and Physics of Lipids*, 2008. **152**(1): p. 24-37.
82. Selinger, J.V. and D.R. Nelson, *Theory of Hexatic-to-Hexatic transitions*. *Physical Review Letters*, 1988. **61**(4): p. 416-419.
83. Meine, K., D. Vollhardt, and G. Weidemann, *Atomic force microscopy study of the texture of condensed phase domains in 1-monostearoylglycerol monolayers*. *Langmuir*, 1998. **14**(7): p. 1815-1821.
84. Gourdon, D., N.A. Burnham, A. Kulik, E. Dupas, F. Oulevey, G. Gremaud, D. Stamou, M. Liley, Z. Dienes, H. Vogel, and C. Duschl, *The dependence of friction anisotropies on the molecular organisation of LB films as observed by AFM*. *Tribology Letters*, 1997. **3**(4): p. 317-324.
85. Hatta, E. and T.M. Fischer, *String defects connecting pairs of half-integer disclinations and tilting transition of a Langmuir monolayer*. *Journal of Physical Chemistry B*, 2005. **109**(7): p. 2801-2804.
86. Hatta, E. and T.M. Fischer, *Splitting of an $s=1$ point disclination into half-integer disclinations upon laser heating of a Langmuir monolayer*. *Journal of Physical Chemistry B*, 2003. **107**(26): p. 6406-6410.
87. Swendsen, R.H., *1st-Order and 2nd-Order Phase-Transitions in the $D=2$ XY Model*. *Physical Review Letters*, 1982. **49**(18): p. 1302-1305.

88. Lee, D.H. and G. Grinstein, *Strings in Two-Dimensional Classical XY Models*. Physical Review Letters, 1985. **55**(5): p. 541-544.
89. Pang, J.Z., C.D. Muzny, and N.A. Clark, *String Defects in Freely Suspended Liquid-Crystal Films*. Physical Review Letters, 1992. **69**(19): p. 2783-2786.
90. Kuzmin, P.I., S.A. Akimov, Y.A. Chizmadzhev, J. Zimmerberg, and F.S. Cohen, *Line tension and interaction energies of membrane rafts calculated from lipid splay and tilt*. Biophysical Journal, 2005. **88**(2): p. 1120-1133.
91. Blanchette, C.D., W.-C. Lin, C.A. Orme, T.V. Ratto, and M.L. Longo, *Using nucleation rates to determine the interfacial line tension of symmetric and asymmetric lipid bilayer domains*. Langmuir, 2007. **23**(11): p. 5875-5877.
92. Garcia-Saez, A.J., S. Chiantia, and P. Schwille, *Effect of line tension on the lateral organization of lipid membranes*. Journal of Biological Chemistry, 2007. **282**(46).
93. Koynova, R. and M. Caffrey, *Phases and phase transitions of the phosphatidylcholines*. Biochimica Et Biophysica Acta, 1998. **1376**(1): p. 91-145.
94. Sun, W.J., R.M. Suter, M.A. Knewton, C.R. Worthington, S. Tristramnagle, R. Zhang, and J.F. Nagle, *Order and Disorder in Fully Hydrated Unoriented Bilayers of Gel Phase Dipalmitoylphosphatidylcholine*. Physical Review E, 1994. **49**(5): p. 4665-4676.
95. Katsaras, J., D.S.C. Yang, and R.M. Eppard, *Fatty-Acid Chain Tilt Angles and Directions in Dipalmitoyl Phosphatidylcholine Bilayers*. Biophysical Journal, 1992. **63**(4): p. 1170-1175.
96. Tristram-Nagle, S., Y.F. Liu, J. Legleiter, and J.F. Nagle, *Structure of gel phase DMPC determined by X-ray diffraction*. Biophysical Journal, 2002. **83**(6): p. 3324-3335.
97. Sun, W.J., S. TristramNagle, R.M. Suter, and J.F. Nagle, *Structure of gel phase saturated lecithin bilayers: Temperature and chain length dependence*. Biophysical Journal, 1996. **71**(2): p. 885-891.
98. Witten, T.A. and L.M. Sander, *Diffusion-limited Aggregation*. Physical Review B, 1983. **27**(9): p. 5686-5697.
99. Witten, T.A. and L.M. Sander, *Diffusion-limited Aggregation, a Kinetic Critical Phenomenon*. Physical Review Letters, 1981. **47**(19): p. 1400-1403.
100. Papon, P., J. Leblond, and P.H.E. MeIjer, *The physics of Phase Transistion - concept and application*2002: Springer.
101. Weidemann, G. and D. Vollhardt, *Long range tilt orientational order in fatty acid ethyl ester monolayers*. Langmuir, 1996. **12**(21): p. 5114-5119.

102. Weidemann, G. and D. Vollhardt, *Long-Range tilt Orientational Order in Phospholipid Monolayers - The Inner sStructure of Dimyrstoyl-Phosphatidyl-Ethanolamine Domains*. Thin Solid Films, 1995. **264**(1): p. 94-103.
103. Schwartz, D.K., *Langmuir-Blodgett film structure*. Surface Science Reports, 1997. **27**(7-8): p. 245-334.
104. Viswanathan, R., L.L. Madsen, J.A. Zasadzinski, and D.K. Schwartz, *Liquid to Hexatic to Crystalline Order in Langmuir-Blodgett-Films*. Science, 1995. **269**(5220): p. 51-54.
105. Zasadzinski, J.A., R. Viswanathan, L. Madsen, J. Garnæs, and D.K. Schwartz, *Langmuir-Blodgett-Films*. Science, 1994. **263**(5154): p. 1726-1733.
106. Zasadzinski, J.A.N., C.A. Helm, M.L. Longo, A.L. Weisenhorn, S.A.C. Gould, and P.K. Hansma, *Atomic Force Microscopy of Hydrated Phosphatidylethanolamine Bilayers*. Biophysical Journal, 1991. **59**(3): p. 755-760.
107. Schwartz, D.K., J. Garnæs, R. Viswanathan, S. Chiruvolu, and J.A.N. Zasadzinski, *Quantitative Lattice Measurement of Thin Langmuir-Blodgett-Films by Atomic-Force Microscopy*. Physical Review E, 1993. **47**(1): p. 452-460.
108. Bourdieu, L., P. Silberzan, and D. Chatenay, *Langmuir-blodgett films - From micron to angstrom*. Physical Review Letters, 1991. **67**(15): p. 2029-2032.
109. Shih, M.C., J.B. Peng, K.G. Huang, and P. Dutta, *Structures of Fatty-Acid Monolayers Transferred to Glass Substrates from Various Langmuir Monolayer Phases*. Langmuir, 1993. **9**(3): p. 776-778.
110. Engel, M., H.J. Merle, I.R. Peterson, H. Riegler, and R. Steitz, *Structural Relationships between Floating and Deposited Monolayers of Docosanoic Acid*. Berichte Der Bunsen-Gesellschaft-Physical Chemistry Chemical Physics, 1991. **95**(11): p. 1514-1520.
111. Brzezinski, V. and I.R. Peterson, *Deposition Effects on the Structure of Langmuir-Blodgett Monolayers of Docosanoic acid*. Journal of Physical Chemistry, 1995. **99**(33): p. 12545-12552.
112. Lee, K.Y.C., M.M. Lipp, D.Y. Takamoto, E. Ter-Ovanesyan, J.A. Zasadzinski, and A.J. Waring, *Apparatus for the continuous monitoring of surface morphology via fluorescence microscopy during monolayer transfer to substrates*. Langmuir, 1998. **14**(9): p. 2567-2572.
113. Ding, J.Q., I. Doudevski, H.E. Warriner, T. Alig, and J.A. Zasadzinski, *Nanostructure changes in lung surfactant monolayers induced by*

- interactions between palmitoyloleoylphosphatidylglycerol and surfactant protein B.* Langmuir, 2003. **19**(5): p. 1539-1550.
114. Leporatti, S., G. Brezesinski, and H. Mohwald, *Coexistence of phases in monolayers of branched-chain phospholipids investigated by scanning force microscopy.* Colloids and Surfaces a-Physicochemical and Engineering Aspects, 2000. **161**(1): p. 159-171.
 115. Chi, L.F., M. Gleiche, and H. Fuchs, *Study of long-range tilt orientation in fatty acid monolayers by dynamic scanning force microscopy.* Langmuir, 1998. **14**(4): p. 875-879.
 116. Hisada, K. and C.M. Knobler, *Friction anisotropy and asymmetry related to the molecular tilt azimuth in a monolayer of 1-monopalmytoyl-rac-glycerol.* Langmuir, 2000. **16**(24): p. 9390-9395.
 117. Liley, M., D. Gourdon, D. Stamou, U. Meseth, T.M. Fischer, C. Lautz, H. Stahlberg, H. Vogel, N.A. Burnham, and C. Duschl, *Friction anisotropy and asymmetry of a compliant monolayer induced by a small molecular tilt.* Science, 1998. **280**(5361): p. 273-275.
 118. Gehlert, U., J.Y. Fang, and C.M. Knobler, *Relating the organization of the molecular tilt azimuth to lateral-force images in monolayers transferred to solid substrates.* Journal of Physical Chemistry B, 1998. **102**(15): p. 2614-2617.
 119. Mermin, N.D., *E Pluribus Boojum: the physicist as Neologist.* Physics Today, 1981. **34**(4): p. 46-53.
 120. Pedrotti, F.L. and L.S. Pedrotti, *Introduction to Optics.* 2nd ed1993: Prentice Hall.
 121. Ozder, S., O. Koysal, S.E. San, and F.N. Ecevit, *Determination of the refractive index dispersion of thick films by continuous wavelet transform.* Thin Solid Films, 2004. **458**(1-2): p. 257-262.

Appendix 1

Paper

Texture defects in lipid membrane domains

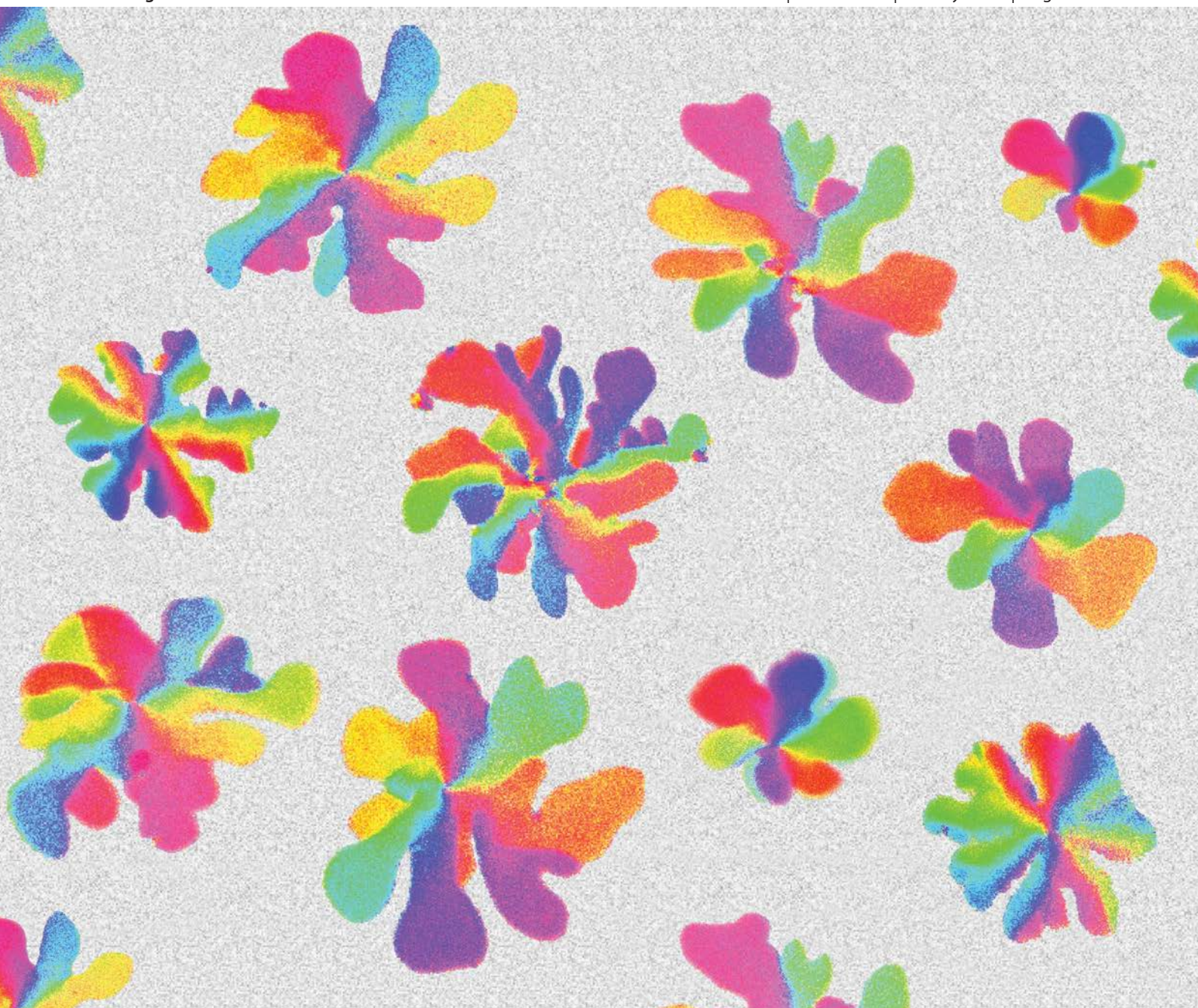
Jes Dreier, Jonathan Brewer and Adam Cohen Simonsen

Soft Matter, 2012, 8, 4894

Soft Matter

www.rsc.org/softmatter

Volume 8 | Number 18 | 14 May 2012 | Pages 4835–5088



ISSN 1744-683X

RSC Publishing

PAPER
Adam Cohen Simonsen *et al.*
Texture defects in lipid membrane domains



1744-683X(2012)8:18;1-9

Cite this: *Soft Matter*, 2012, **8**, 4894

www.rsc.org/softmatter

PAPER

Texture defects in lipid membrane domains

Jes Dreier,^{ab} Jonathan Brewer^{ac} and Adam Cohen Simonsen^{*ab}

Received 2nd December 2011, Accepted 25th February 2012

DOI: 10.1039/c2sm07290d

Important aspects of lateral organization in biomembranes can be addressed in model systems. Recently, it has become clear from polarized fluorescence imaging and X-ray scattering that gel domains in bilayers may contain orientational texture related to the tilted acyl chains. Such internal structure of domains can be imaged in polarized 2-photon fluorescence microscopy using the Laurdan probe that aligns with the lipids. By imaging intensity variations as a function of the polarization angle, we map the lateral variations within domains. A Fourier analysis of the signal enables the texture to be obtained in single pixels. Here we show that gel domains display a complex pattern containing line defects and a pair of $|m| = 1/2$ point disclinations in the domain center. We perform a detailed image analysis of the line and point defects using gradient calculations. In contrast to results from Langmuir monolayers, the membrane texture vary radially and is continuous in the center and segmented near the periphery. A possible explanation is that bilayer domains are grown thermally whereas Langmuir monolayer domains grow isothermally upon compression. The defect lines show significant variation in the angle jump across the lines. We simulate the structure of the central disclination pair and the fit to the experimental data yields an offset angle of $60.5^\circ \pm 6.5^\circ$. This indicates that the central defect has a conserved structure with an intermediate character between bend and splay.

1. Introduction

The principles governing the lateral organization of biomembranes has been a matter of intense study for decades. Due to the complexity of biomembranes, a large set of possible interactions is possible which has made it difficult to establish the underlying physical principles for membrane organization in biological cells. As an alternative, the development of simple membrane models has proven a successful strategy for mimicking and understanding domain formation.¹ Characterization of model membrane domains provides a reference as formulated in terms of soft condensed matter concepts and thermodynamics.

Model membrane studies are typically focused on the membrane phase state, domain sizes and lipid composition and only recently has it become clear that certain condensed membrane phases are not homogeneous, but may have orientational texture. Such texture arises if the lipid acyl chains are tilted with respect to the bilayer normal. This creates a degree of freedom associated with the orientation of the projection (the director) of the acyl chain in the bilayer plane. In gel membrane phases there may exist hexatic, long-range positional

orientational order in the crystal which couples to the lipid tilt orientation. This enables the system to sustain texture patterns with long-range order in the orientation angle that is visible in optical microscopy. In a previous report we have shown² that polarization two-photon fluorescence microscopy of Laurdan-labeled membranes is able to reveal an orientational texture in gel domains. Despite the internal structure of the domains their thermodynamic phase state was shown, by Laurdan GP measurements, to be uniform.

The existence of texture in lipid bilayers is not surprising as Langmuir monolayers have long been known to display texture and topological defects. These are in many aspects similar to textures initially found in liquid crystals.^{3,4} Thin films of smectic-C (Sm-C) liquid crystal can be drawn over an opening in a microscope slide and may display orientational textures when observed using depolarized reflected light microscopy (DRLM).⁵⁻⁷ This system of stacked layers can in some aspects be compared to lipid bilayers and, a priori, we would expect similar texture patterns to be possible in both systems. Topological defects observed in Sm-C systems include integer and fractional vortices as well as string defects and combinations thereof. An important difference from monolayer and bilayer domain textures is that domains in these systems are formed through nucleation and growth and have a finite size and a boundary to a surrounding isotropic phase. This means that boundary conditions and details of the nucleation and growth may influence the final texture.

^aMEMPHYS - Center for Biomembrane Physics, University of Southern Denmark, 5230 Odense M, Denmark. E-mail: adam@memphys.sdu.dk

^bDepartment of Physics, Chemistry and Pharmacy, 5230 Odense M, Denmark

^cDepartment of Biochemistry and Molecular Biology, 5230 Odense M, Denmark

Microscopy of coexisting liquid (LE) and condensed (LC) domains in Langmuir monolayers has been performed for decades. The early studies of texture in Langmuir monolayer (LC) domains were primarily done using Brewster angle microscopy (BAM)^{8–13} and polarized fluorescence microscopy.^{14–18} Combined with X-ray diffraction data and compression isotherms, a detailed picture of domains and domain textures has been established in monolayers.^{19–21} The energetics associated with different types of textures can be modeled by Landau-type free energy models²² which allow classification of textures and defects and explains how they are related to the relative strength of the free energy terms.

X-ray diffraction applied to Langmuir monolayers was initiated by Kjaer *et al.*²³ demonstrating that the LC domains had hexatic order. Many LC phases have since been shown to be hexatics¹⁹ while some phases are 2D crystals. The hexatic phase is intervening between the crystalline and liquid states and is prominent in 2D systems. It is characterized by short-range positional order and long-range order in the bond-angle (BA) field.^{24–27} This leads to a sixfold orientational symmetry in this phase. Results using grazing incidence X-ray diffraction (GIXD) on bilayer samples have established a link between hexatic order and texture in gel phase membranes and proven that texture can be influenced by biomolecular binding events.^{28–30} Note that while GIXD can measure the short-range positional order, complementary imaging by microscopy is necessary to detect the long-range texture.

Textures in monolayer and bilayer domains are rarely uniform, but may contain defects with the two main ones being point disclinations and line defects. Point disclinations are characterized by their index m which gives the number of turns of the director for one revolution around the defect point. Line defects are characterized by a discrete jump in the azimuth angle of the director when crossing the defect line. Both lines and point disclinations may have bend or splay character depending on the orientation of the director relative to the defect. In this paper we provide an analysis of texture patterns and defects in bilayer gel domains. Previously,² we introduced a Fourier method to extract texture from polarized fluorescence images. Here we provide a detailed image analysis of texture defects including an examination of line defects and the splitting of the central point disclination. The results reveal important differences from textures in monolayer domains.

2. Materials and methods

2.1. Materials

1,2-dipalmitoyl-sn-glycero-3-phosphocholine (DPPC) and 1,2-dioleoyl-sn-glycero-3-phosphocholine (DOPC) were purchased from Avanti Polar Lipids and used without further purification. The membrane probe Laurdan was from Molecular Probes/Invitrogen. All solvents and chemicals (Sigma-Aldrich) were HPLC grade quality, and ultra pure Milli-Q water (18.3 M Ω ·cm) was used in all steps involving water. HEPES buffer (10 mM HEPES, 148 mM NaCl) was prepared at pH = 7.0 by mixing appropriate amounts of HEPES acid, HEPES base and NaCl. Muscovite mica was from Plano GmbH (Germany) and cut into 10 mm \times 10 mm sheets for microscopy.

2.2. Preparation of supported lipid bilayers

A dry spin-coated lipid film (DOPC, DPPC, 1 : 1) on mica was prepared using a stock solution of 10 mM lipid mixture containing 0.5% fluorescent probe in isopropanol, hexane, water (60%, 20%, 20% volume ratio). A droplet (30 μ L) of the lipid stock was applied to freshly cleaved mica and spun on a Chemat Technology, KW-4A spin-coater at 3000 rpm for 40 s. The sample was placed under vacuum to ensure evaporation of solvents. The spincoated film was hydrated in a commercial fluid cell for microscopy (BioCell, JPK Instruments AG, Berlin, Germany). Buffer was added and the immersed sample was heated to 55 $^{\circ}$ C for 1 h. The sample was subsequently flushed with 55 $^{\circ}$ C buffer using a pipette. By epi-fluorescence microscopy of the lipid film while washing, the removal of lipid layers could be accurately controlled. Afterwards, the liquid volume was gently exchanged 5–10 times to remove membranes in solution. The sample was then cooled to 20 $^{\circ}$ C at a rate of 1 deg/min during which domain nucleation and growth takes place. After cooling, the domains stop growing and are stable in shape over at least 30–60 min. The sample is measured after \sim 30 min to ensure thermal equilibrium with the microscope. Further details of the sample preparation can be found in.³¹ Note that the rate of cooling influences the density of nucleation points and the final size of the domains, as previously documented.³² For polarized two-photon microscopy, the sample was placed with the membrane facing the objective to avoid transmission through the birefringent mica substrate.

2.3. Microscopy

The geometry of the system and the symbols used are explained in Fig. 1. The emission intensity of the Laurdan probe varies with the angle between the polarization of the excitation light and the azimuth orientation of lipid chains. By recording emission images as function of the polarization angle, we map the lateral

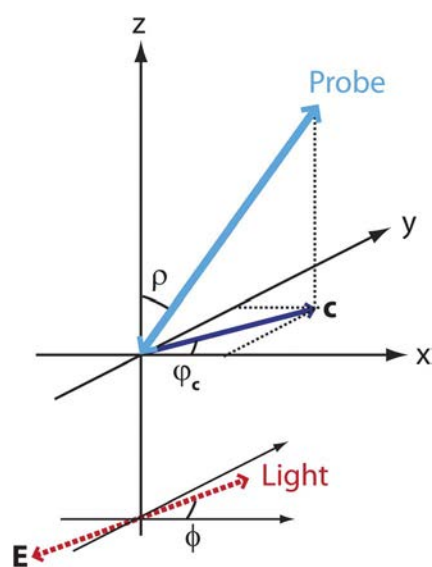


Fig. 1 Schematic explanation of the experiment in an xyz frame of reference. Top view shows the tilted Laurdan probe which is embedded in the bilayer and bottom shows the E-field of the polarized excitation light.

variations of the lipid tilt within domains. The direction of the excitation light is parallel to the bilayer normal and the electric field of the linearly polarized light is perpendicular. In the liquid phase, random fluctuations of the acyl chains will give rise to a non-zero projection of the probe dipole \mathbf{p} on the the polarization axis. This results in a net fluorescence signal, independent of the polarization angle of the excitation light. This is in contrast to the gel phase where the lipids are ordered. The planar, gel phase membranes considered here, have their acyl chains tilted from the bilayer normal at about $\rho = 33^\circ$.³³

Two-photon excitation fluorescence microscopy measurements were done using a custom built microscope, constructed around an Olympus IX70 microscope. The objective used was a 60X water immersion objective with NA = 1.2. The excitation source was a femtosecond Ti:Sa laser (Broadband Mai Tai XF W25 with a 10 W Millennia pump laser, tunable excitation range 710–980 nm, Spectra Physics, Mountain View, CA) and the excitation wavelength used was 780 nm. A half-wave plate was used to control the polarization, where a rotation of 5° of the half-wave plate results in a 10° rotation of the electric field. The emission wavelength of Laurdan depends on the membrane phase state and emitted light was collected in two channels using bandpass filters of 438 ± 12 nm (gel phase) and 494 ± 10 nm (fluid phase) and a dichroic mirror splitting at 475 nm. Detection was done with photo multiplier tubes (Hamamatsu H7422P-40).² The texture analysis was done on images taken at 438 ± 12 nm.

3. Image analysis procedures

Below we describe the procedure for analyzing texture patterns from the original stack of fluorescence images. The procedure was implemented as a series of Matlab GUIs. The angle of polarization with respect to the x -axis is denoted ϕ (see Fig. 1) and is sampled discretely from $0-2\pi$ in steps of $\Delta\phi$. The intensity of a single pixel is denoted I_k^{mn} where index k gives the angle increment and indices m,n are pixel rows and columns respectively. I_k^{mn} is defined in the following way:

$$I_k^{mn} = I^{mn}(\phi_k) = I^{mn}(\phi_{\text{offset}} + \text{Rot} \cdot k \cdot \Delta\phi) \quad (1)$$

Here we have specified an experimental angle offset ϕ_{offset} , and the direction of rotation of the polarizer in the image plane $\text{Rot} = \pm 1$, where $\text{Rot} = 1$ is counterclockwise rotation.

Due to non-ideal properties of the optical components in the microscope, the intensity of the excitation light can be slightly dependent on ϕ . We correct for this effect by normalizing against an isotropic sample region with a random orientation of the molecular director \mathbf{c} . The emission intensity in this region will approximately be proportional to the excitation intensity and we use this property for correcting. Let $I_k^{\text{ROI}} = \langle I_k^{mn} \rangle_{\text{ROI}}$ denote the average emission intensity in an isotropic region (ROI) of the sample. Then the corrected pixel intensity becomes:

$$I_k^{\text{mn}}(\text{corrected}) = \frac{I_k^{\text{mn}}}{I_k^{\text{ROI}}} \quad (2)$$

In reality, the correction is small and maximum variation of the intensity in the isotropic fluid phase was below 5 percent.

3.1. Texture

The spatial variation of the director field (the texture) is obtained from the discrete Fourier transform of the image stack:

$$\tilde{I}_\gamma^{mn} = \sum_{k=1}^N I_k^{\text{mn}}(\text{corrected}) \cdot e^{-i\frac{2\pi}{N}(\gamma-1)(k-1)} \quad (3)$$

For a tilted probe molecule, the intensity I_k^{mn} completes two harmonic periods when ϕ varies from 0 to 2π . This harmonic variation is conveniently contained in the Fourier mode \tilde{I}_3^{mn} . By considering only this mode we minimize other contributions to the signal arising from bleaching, static background and other sources which are primarily contained in Fourier modes with $\gamma \neq 3$. The modulus $L^{\text{mn}} = |\tilde{I}_3^{\text{mn}}|$ is denoted the *director length* and is a measure of the strength of the angular response corresponding to the length $|\mathbf{c}|$ of the molecular director. Similarly, the argument $-\frac{1}{2} \arg(\tilde{I}_3^{\text{mn}})$ gives the dominant angle of the probe director within the pixel xy . Taking into account the rotation direction in the experiment and the angle offset, we obtain for the *director angle* ϕ_c^{mn} :

$$\phi_c^{\text{mn}} = -\frac{1}{2} \cdot \text{Rot} \cdot \arg[\tilde{I}_3^{\text{mn}}] + \phi_{\text{offset}} \quad (4)$$

Note that the obtained director angles ϕ_c^{mn} will be distributed over the interval: $\pi : \left[-\frac{\pi}{2} + \phi_{\text{offset}}, \frac{\pi}{2} + \phi_{\text{offset}} \right]$. The limitation to an interval of π is a consequence of the fact that the fluorescence emission is equal for probe directors that differ by an orientation of π .

3.2. Smoothed texture and gradient calculation

It is of interest to determine the gradient of the director field $\nabla\phi_c$ since it will enhance defects and because the gradient is related to the energy density of the texture. Noise in the experimental data makes it necessary to perform smoothing of the texture before differentiation. We use moving-box averaging with a smoothing box $S \times S$ where typically $S = 3$ pixels. Smoothing is done on the Fourier component ($\gamma = 3$) and the smoothed director angles $\phi_{c,\text{smoothed}}^{\text{mn}}$ and director lengths are computed from the smoothed Fourier mode:

$$\tilde{I}_3^{\text{mn}}(\text{smoothed}) = \langle \tilde{I}_3^{\text{mn}} \rangle_{S \times S} \quad (5)$$

The gradient $(\text{FX}, \text{FY}) = \nabla\phi_c$ is calculated from the value of the neighboring pixels. We have for the x and y components:

$$\text{FX} = \frac{\partial\phi_c}{\partial x} \Big|_{mn} = \frac{1}{2} \left[\phi_{c,\text{smoothed}}^{m,n+1} - \phi_{c,\text{smoothed}}^{m,n-1} \right] \quad (6)$$

$$\text{FY} = \frac{\partial\phi_c}{\partial y} \Big|_{mn} = \frac{1}{2} \left[\phi_{c,\text{smoothed}}^{m+1,n} - \phi_{c,\text{smoothed}}^{m-1,n} \right] \quad (7)$$

Note that eqn (6) and (7) must be corrected for the fact that in our experiment the directors appear symmetrical forward/backwards as discussed above. For this reason we do not resolve differences in director angles by more than $\pm \frac{\pi}{2}$ and therefore gradients larger than $\pm \frac{\pi}{4}$. Since eqn (6,7) does not take this fact

into account, we correct by shifting gradient values that are numerically larger than $\frac{\pi}{4}$ by $\pm\frac{\pi}{2}$ to bring the gradient values into the measurable interval.

The analysis of texture is only relevant for pixels in gel domains where the director angle is not fluctuating randomly. We isolate pixels inside domains by performing thresholding on the director lengths image L^{mn} which gives a clean segmentation of domains. An example of the director lengths image is shown in Fig. 2C and the corresponding segmentation of the domains is shown as the outline in Fig. 2A and 2B.

3.3. Detection of line defect angles and pair disclinations

An important defect type is line defects where the director angle makes a discrete jump. We denote the angle across such line defects the *jump-angle*. To examine line defects in detail, we will determine the jump-angles locally for pixels on a defect line. This allows us to map the spatial variation within a single line. The procedure consists of the following steps:

1. Pixels belonging to defect regions are identified by a segmentation of the gradient norm $|\nabla\varphi_c|$.

2. For pixels on a line defect, an extension of the gradient vector is drawn to both sides of the defect. The extension beyond the defect region is set manually. The final jump-angles are not very sensitive to the length of this extension since the director is quite uniform inside the subdomains.

3. The extensions are filtered to remove a pixel if the defect region is too wide (not a line defect) or if the extension falls outside the domain.

4. The value of the director in the forward and backward directions are recorded and the absolute difference represents the

jump-angle for that pixel. Only jump-angles $<\frac{\pi}{2}$ are allowed, due to the modulo 180° issue as discussed above.

5. A map of jump-angles is constructed for pixels on the defect line.

In addition to mapping angles of line defects it is relevant to detect the central core defect. The defect may split into two $m = 1/2$ point disclinations that are easily detected as local spikes in the gradient norm of the texture angle. We detect the position of the defects within a pair by fitting 2D gaussians to each peak. The orientation and separation of defects are compared by translating the defect pairs to the same center of mass.

3.4. Simulation of texture

The measured textures are fitted to a simulation to provide information on the bend/splay nature of the texture. We simulate the continuous texture close to the central defect. As described recently by Watkins *et al.*,²⁹ a single point disclination of index m is modeled by the expression: $\varphi_s(x,y) = m \cdot \tan^{-1}(y/x) + \varphi_{s0}$. Here x,y is the lateral position, φ_s is the simulated texture and φ_{s0} is an offset which determines if the texture has bend or splay character. Pure splay is described by $\varphi_{s0} = 0, \pi$ and pure bend by $\varphi_{s0} = \pm\pi/2$. We model a pair of $m = 1/2$ point disclinations by an extension of this expression:

$$\varphi_s(x,y) = \frac{1}{2} \cdot \tan^{-1}\left(\frac{y-y_1}{x-x_1}\right) + \frac{1}{2} \cdot \tan^{-1}\left(\frac{y-y_2}{x-x_2}\right) + \varphi_{s0} \quad (8)$$

where the two point defects are located at positions (x_1,y_1) and (x_2,y_2) . These positions are determined experimentally as described above in section 3.3. The experimental value of φ_{s0} is

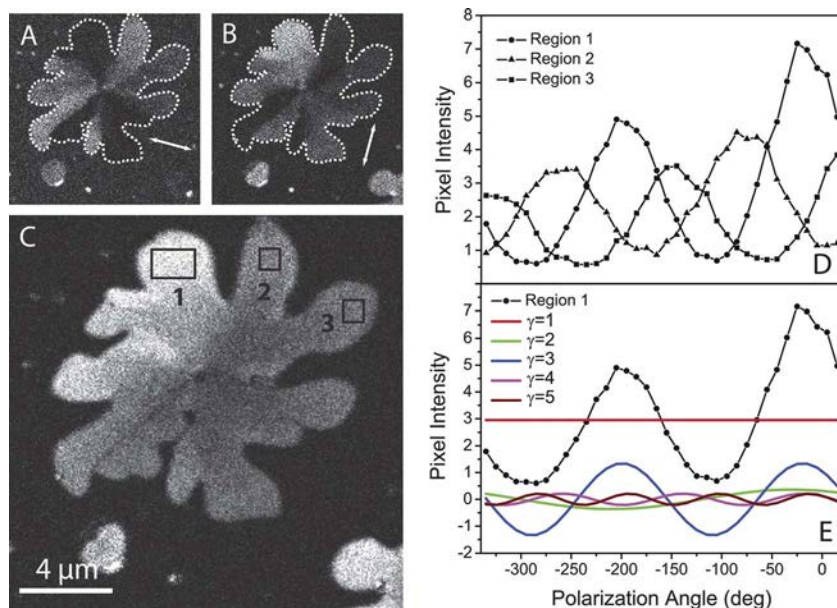


Fig. 2 Selected fluorescence images (A,B) from a polarization scan sequence of 36 images of a supported bilayer with composition DOPC, DPPC (1 : 1). The direction of polarization is indicated with white arrows. The director length image L^{mn} is shown in (C) and has been used for the segmentation of the gel domain as indicated with the dotted white line in (A,B). The variation of the average emission intensity in regions 1,2,3 (C) with respect to polarization angle is shown in (D). Note that the rotation direction of the polarizer is negative. The phase shifts of the harmonic variation originates from the difference in director orientation within these regions. Fourier decomposition of the signal from region 1 is shown in (E). The mode $\gamma = 3$ is used to determine the orientation texture.

obtained by fitting the simulation φ_s (eqn (8)) to the experiment φ_c (eqn (4)).

4. Results

A polarization scan typically consists of a stack of 36 fluorescence images covering a 2π rotation and two images with orthogonal polarizations are shown in Fig. 2A and 2B. Although some structure is visible, the presence of subdomains and texture defects is not always obvious in the raw images, but will appear clearly after calculation of the director pattern. The harmonic variation of the pixel intensity in small regions of a domain is illustrated in Fig. 2C and 2D. The harmonic signals are phase shifted due to differences in the orientation of the director in regions 1–3. Slight photo bleaching of the Laurdan probe during a polarization scan is visible as an amplitude decrease for more negative angles. The Fourier decomposition of the pixel signal from region 1 in Fig. 2E shows the original signal as well as the lowest 5 Fourier modes contributing to the signal. It is clear that the mode $\gamma = 3$ contains the relevant physical information about the probe orientation while bleaching and background intensity is mostly contained in modes with $\gamma \neq 3$.

The map of the director angles can be visualized using a translation of the angles into colors. This representation is shown in Fig. 3 which contains examples of textures in gel domains of membranes with the lipid composition (DOPC, DPPC, 1 : 1). Fig. 3A–3D show the color representation only, while 3E show the directors drawn as lines and averaged over 8×8 pixel regions. The examples illustrate a considerable variation in the texture pattern between domains, while some features are shared. All domains in this system are segmented into subdomains with each subdomain having a preferred orientation of the molecular director. Line defects separating the subdomains are in most cases oriented towards the center, while in larger domains there may be subdomains which are disconnected from the center and located closer to the domain perimeter. An example of this is seen in the domain in Fig. 3B. We show later that none of the defect lines are extending to the center which instead contains a continuous deformation.

The texture shown in Fig. 3E exhibits an overall spiralled deformation of the directors. The line defects can be divided in two pure types: splay or bend walls.²² In splay walls, the director at the position of the defect, is oriented parallel to the defect line and in bend walls the director is oriented perpendicular. Intermediate types with a tilted orientation across the line are also possible. In Fig. 3F and 3G we show magnified textures for two line defects. These examples demonstrate defects with pure splay (Fig. 3F) and bend (Fig. 3G) character occurring within the same domain. From inspection of Fig. 3E it is clear that other line defects in the same domain have a mixed bend/splay character with some variation in the angle relative to the defect line. Based on this we conclude that no single type of line defects dominates in a domain, but that several types are present simultaneously.

The histogram of director angles in a domain provides useful information about their distribution. Fig. 4A shows a histogram of the angles φ_c for pixels inside one domain. The histogram is fitted to a sum of three Gaussians and intervals representing the mean ± 1 standard deviation where colored red, green and blue. The pixels in the domain with angles in these intervals where

colored correspondingly and all other pixels left black, as shown in Fig. 4B. The three dominating angles are: -22° (red), 25° (green), and 95° (blue) and it is seen that these angle intervals account for most of the domain area. The dominating angles are clearly represented by separate regions and not mixed. The typical pattern is that each color is located in two oppositely placed subdomains. Such two opposite subdomains will actually have parallel, but oppositely oriented directors, which cannot be discriminated here. Thus the 3 different angles in the histogram correspond to 6 different physical orientations in the domain. From the peaks in Fig. 4A we find the angle difference between neighboring subdomains. The measured values are: red-to-green = 47° , green-to-blue = 70° and blue-to-red = 63° . These values differ from the 60° expected from an even 6-fold distribution of the orientations which none of our domains have been observed to have. The change in orientation is not always confined to the line between subdomains. In some regions of Fig. 4B and 4D, a black area between subdomains indicates a gradual transition rather than a line defect, such as in the blue (left) and green (left) subdomains of Fig. 4B. The majority of domains analyzed have 3 dominating orientations located in 6 subdomains, but a higher number of distinct orientations is sometimes observed. This occurs when the directors in two opposing subdomains are not completely parallel and therefore split into two peaks in the angle histogram. The example in Fig. 4C, shows 5 peaks with positions -67° (red), -19° (green), 0° (blue), 29° (yellow) and 56° (cyan) and the corresponding color image is seen in Fig. 4D. In this example, 2 out of 3 angle peaks has split and created the pairs blue-green and yellow-cyan. Note, that the red peak is representing 2 opposite orientations in the domain such that there is still 6 physical orientations in the domain like in the previous domain of Fig. 4B.

To examine more closely the defect structure of a domain we consider the gradient of the director angles $\nabla\varphi_c$. The gradient norm is useful for amplifying defect patterns and for revealing hidden defects. The gradient computation was carried out as explained in section 3.2 and Fig. 5 shows an example of the gradient analysis for one domain. The original texture of the domain is shown in 5A and the gradient norm $|\nabla\varphi_c|$ inside the domain boundary is shown in the grayscale image of 5B. Several conclusions can be drawn from Fig. 5B. The defect lines appear approximately halfway between the perimeter and the center. In contrast, the center region has a continuous variation of the director around a point defect and the texture in this region appears as a round bright structure in the gradient norm image. The defect lines are not straight, but can curve significantly as seen most clearly for the domain marked with the square in Fig. 5B. We identify 8 lines in Fig. 5B, but the classical 6-fold pattern is also observed in some domains.

Since the defect lines are clearly non-uniform, it is relevant to characterize them locally. The gradient of the azimuth angle is useful for this purpose. Specifically, we are interested in mapping the jump-angles between subdomains for each pixel on a defect line. As explained in section 3.3 we identify pixels on the line defects by a simple thresholding of the gradient norm as shown in Fig. 5C and 5D. By extending the gradient vector to outside the defect lines we determine the jump-angle locally along the line. This was done in Fig. 5E which shows a color coded map of the jump-angles on the defect lines. It is evident from Fig. 5E that the

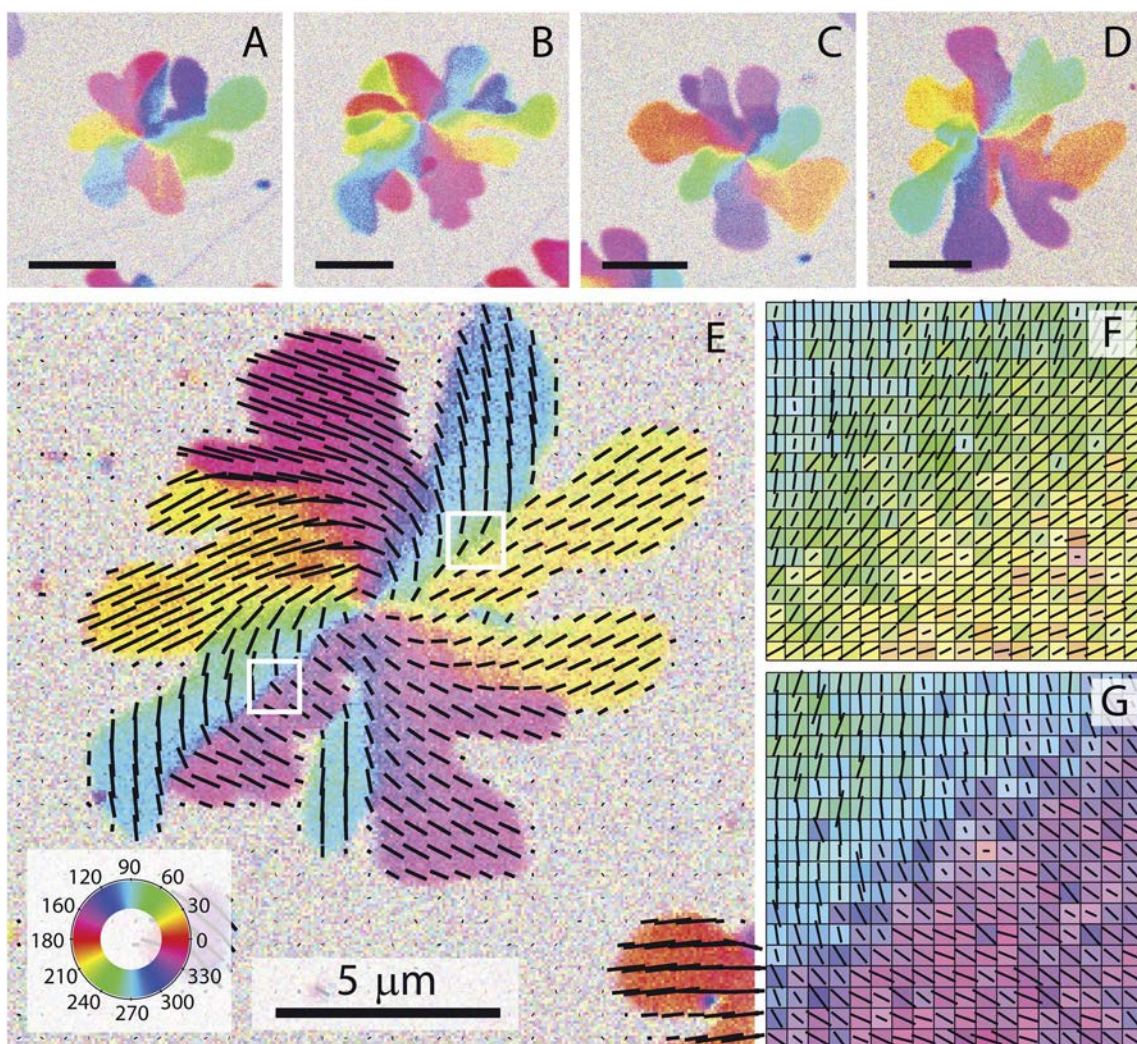


Fig. 3 Examples of textures in gel domains (DOPC, DPPC, 1 : 1) (A–E). The orientation angle φ_c of the molecular director is represented by colors as in the legend (E). Image (E) shows black lines representing the directors averaged over 8×8 pixel regions of the image. The length of each line is proportional to the director length L while the orientation is given by φ_c . Magnified textures (F,G) are resolved at the level of single pixels in the indicated regions of image (E). (F) shows example of a defect line with almost pure splay deformations while (G) shows a line with almost pure bend deformations. Other line defects in the domain may have mixed splay/bend character. All scale bars are $5 \mu\text{m}$.

jump-angle is varying considerably both between different defect lines and within single lines. For some line defects the variation along the line is such that the jump-angle increases with increasing distance from the domain center. The opposite trend is not observed, but some lines have a relatively constant jump-angle. The distribution of jump-angles for individual defect lines is shown in Fig. 5F which shows gaussian fits to the distributions. These distributions clearly reveal both the variation between the defect lines and the considerable internal variation within the lines.

In the far field the central point disclination behaves as an index $|m| = 1$ defect and for a simple star-shaped pattern of defect lines, the jump-angles should therefore sum to 360° . Our images show a more complex structure of the lines and variation of the director inside subdomains. This means that a straightforward summation of the jump-angles to 360° is not always obtained.

Next we focus on the point defect structure in the domain center. By appropriate scaling of the grayscale in the gradient norm image it becomes clear that the defect of the center, in fact consists of two closely spaced point defects as in Fig. 6A (and insert). Such paired defects are present in all observable domains with this lipid composition, but not necessarily if the lipid composition is changed. Some domains have bound vesicles at the domain center which obscures precise characterization of the defect pair for these domains. From the previous inspection of the texture pattern we know that the central defect is of index $|m|=1$ in the far field such that the splitting generates two $|m| = 1/2$ point disclinations. We first examine the separation and orientation of these defect pairs. Fig. 6A (insert) shows the gradient norm image along with the detected defect positions. Pairs of $|m| = 1/2$ point disclinations must theoretically be connected by a defect line that separates regions with opposite orientations of the directors. A hypothetical straight line is

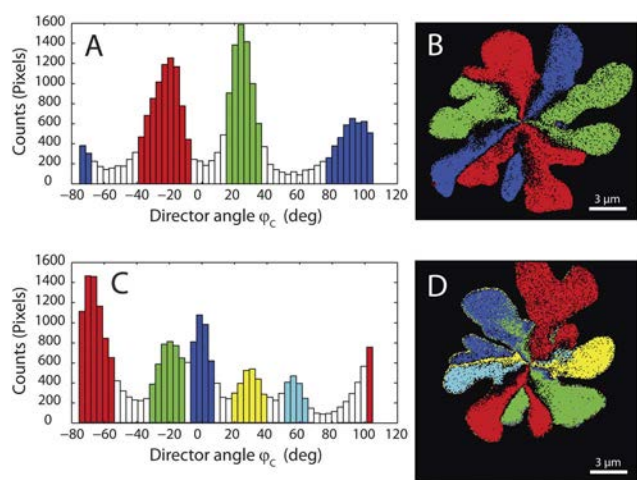


Fig. 4 Histogram of the director angles within a typical gel domain (A). Three peaks are present corresponding to three (six) dominating orientations of the director in the domain. The peaks are fitted to a sum of three gaussians to obtain mean (μ) and standard deviation (σ) for each peak. The red/green/blue bars are the intervals: $\mu \pm \sigma$. The pixels having values of φ_c within these intervals are shown in (B). An equivalent representation of a domain where 5 angles are discernible in the histogram (C,D).

drawn between the two defects in Fig. 6 to illustrate this fact. The location of defect pairs in 10 gel domains is shown in Fig. 6B, where the defect pairs have been translated to the same center of mass to enable a comparison. Both the separation and orientation of pairs fluctuate between the domains.

When comparing with a simulated texture pattern, more quantitative information can be extracted about the center defect. As an example, the texture in the center of a domain is shown in Fig. 7A along with the detected pair of $|m| = 1/2$ point disclinations. In this central region, the texture is continuous and does not exhibit line defects. Therefore it is possible to model it by an expression of the form in eqn (8). We keep the detected defect positions fixed in eqn (8) so the only fitting parameter is the offset angle φ_{s0} which determines the bend/splay character of the defect pattern. The simulated texture best matching the data is shown in Fig. 7B. Note that two equivalent textures, differing only by a rotation of the director by π , will match the experiment equally well and one is shown in Fig. 7B. The error map (7C) showing the pixel-by-pixel difference between measurement and simulation indicates good overall agreement across the simulated region. The average angle difference between model and experiment has been plotted against φ_{s0} in Fig. 7D highlighting the two minima where the simulation matches the experiment. The experimental value for the offset averaged over 10 domains

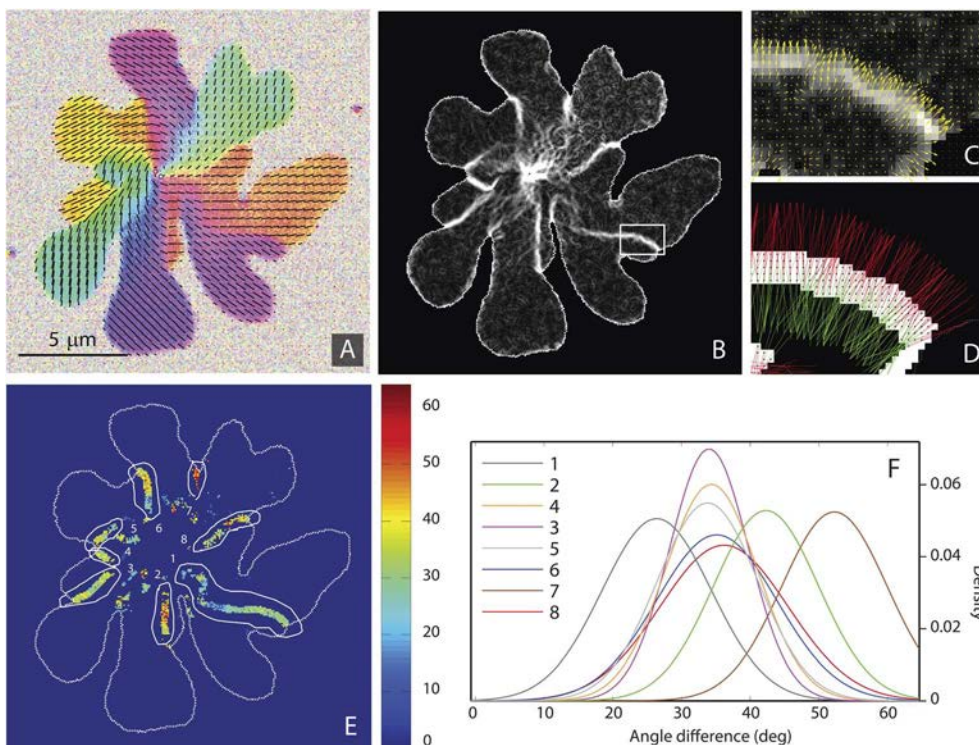


Fig. 5 Analysis of jump-angles associated with line defects in the texture pattern. The domain texture (A) is analyzed by numerically computing the gradient $\nabla\varphi_c$ which is visualized as the the gradient norm $|\nabla\varphi_c|$ shown in (B). The rectangle in (B) indicates the region of the zoom (C) of the gradient image. Yellow arrows show the gradient vectors at the single pixel level. The change in director angle (jump-angle) across a line defect is computed by examining the extension of the gradient from the boundary pixels. Image (D) illustrates this construction (see text). The jump-angles for individual pixels on the line defects are shown as color coded pixels in image (E). The units of the colorbar are degrees and all pixels not belonging to line defects are void (dark blue). Gaussian fits (F) to the distribution of jump-angles in 8 selected line defects as indicated by the outlined regions in (E). The distributions in (F) illustrates the typical variation in jump-angles among the line defects of a single domain.

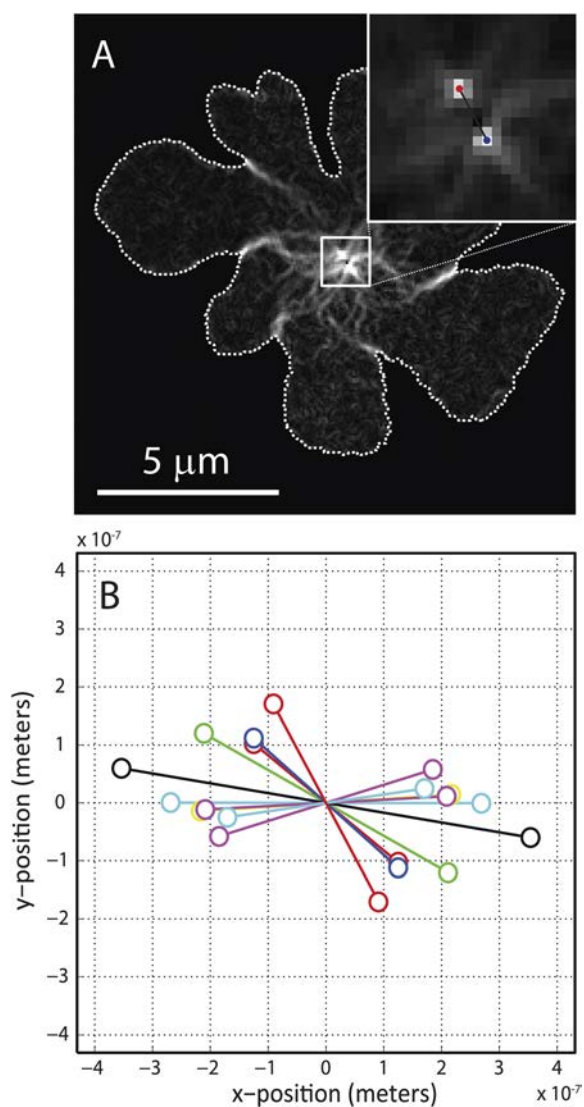


Fig. 6 Detection of point disclination pairs in gel domains. The gradient norm image $|\nabla\phi_d|$ in (A) shows a large magnitude of the gradient (bright) in the domain center. A zoom (insert) of the texture in this region reveals two closely spaced point defects whose positions are detected by fitting 2D gaussian peaks to the gradient norm. The resulting positions are the red and blue point (insert). Plot in (B) shows defect pair locations for $N = 10$ gel domains where all defect pairs have been translated to the same center of mass to enable comparison.

is $|\varphi_{s0}| = 60.5^\circ \pm 6.5^\circ$, where the deviation is plus/minus one standard deviation. We conclude from this that the experimental value of φ_{s0} can be extracted accurately from a fit to the model and that the spread in measured values is low.

5. Discussion and conclusion

In summary, we have performed image analysis of texture defects in membrane gel domains based on polarization scans. The results reveal a complex pattern of defects and several issues and topics for further study arise.

First we discuss a possible correlation between the domain shape and the texture pattern. In the present system this

correlation is found to be rather weak, but one could in general imagine this coupling to work in at least two ways: (1) That texture created early in the growth/nucleation regulates the domain shape during growth by defining certain optimal growth directions or: (2) That the domain shape controls texture *via* boundary conditions.

Regarding the first mechanism, the smallest leaf-shaped domains we have studied will typically contain six leaves that coincide with the six-fold texture pattern of a hexatic lattice. Such small domains are seen for temperatures slightly below the transition temperature and indicate that the domain shape can be partially controlled by the hexatic lattice and the point defect. But the larger domains forming at lower temperatures, as shown in this paper, become more branched and asymmetric and this simple relationship no longer holds.

Regarding the second mechanism, we could expect domain shape and texture to couple *via* boundary conditions for the director at the domain perimeter. In monolayers, normal boundary conditions are expected rather than parallel conditions, according to Fischer *et al.*²² But in Fig. 2, the director orientation is not fixed with respect to the boundary and we conclude that this energy is apparently not strong enough to visibly align the texture with respect to the boundary. This indicates a rather weak influence of boundary conditions for large domains. Coupling between shape and texture could also occur *via* the energy cost of creating defect lines (splay and bend walls). In this case, energy could be minimized by shortening the defect line leading to invaginations in the domain shape where the lines intersect the boundary. From Fig. 2A–2D this is seen for most of the lines, but not all. This indicates some variation in line energy, possibly related to the bend or splay character of the lines.

We have previously examined gel domain shapes in detail³² and found that shape is highly regulated by another mechanism, namely the spatial pattern of neighboring domains. The pattern of nucleation sites in the membrane effectively creates capture zones around each domain defining its nearest neighborhood region. The shape of such zones (Voronoi polygons) was shown to correlate strongly with the shape of domains possibly through competition for gel-phase lipids during growth. The correlation was increasingly strong for larger domains.

Recently Longo and Blanchette reviewed various mechanisms influencing the shapes of cerebroside-rich domains in model membranes.³⁴ One of the mechanisms discussed was edge diffusion of lipids in gel domains. It has been observed³⁵ that gel domains may change isothermally from branched to more compact shapes following several hours after formation. This is attributed to edge diffusion and line tension which redistributes material to make the domain more circular, thereby shortening the perimeter and lowering the boundary energy. We did not specifically study shape relaxations in in this work, partly due to photobleaching of Laurdan, but this slow process is likely to occur. The influence of shape changes on the texture will depend on the importance of boundary conditions and may also be related to the lipid composition. In our system, boundary conditions for large domains are not strongly enforced. One possibility is that edge diffusion may simply lead to an ‘epitaxial’ redistribution of material on the edge such that the boundary shape changes, but without major changes in the texture pattern.

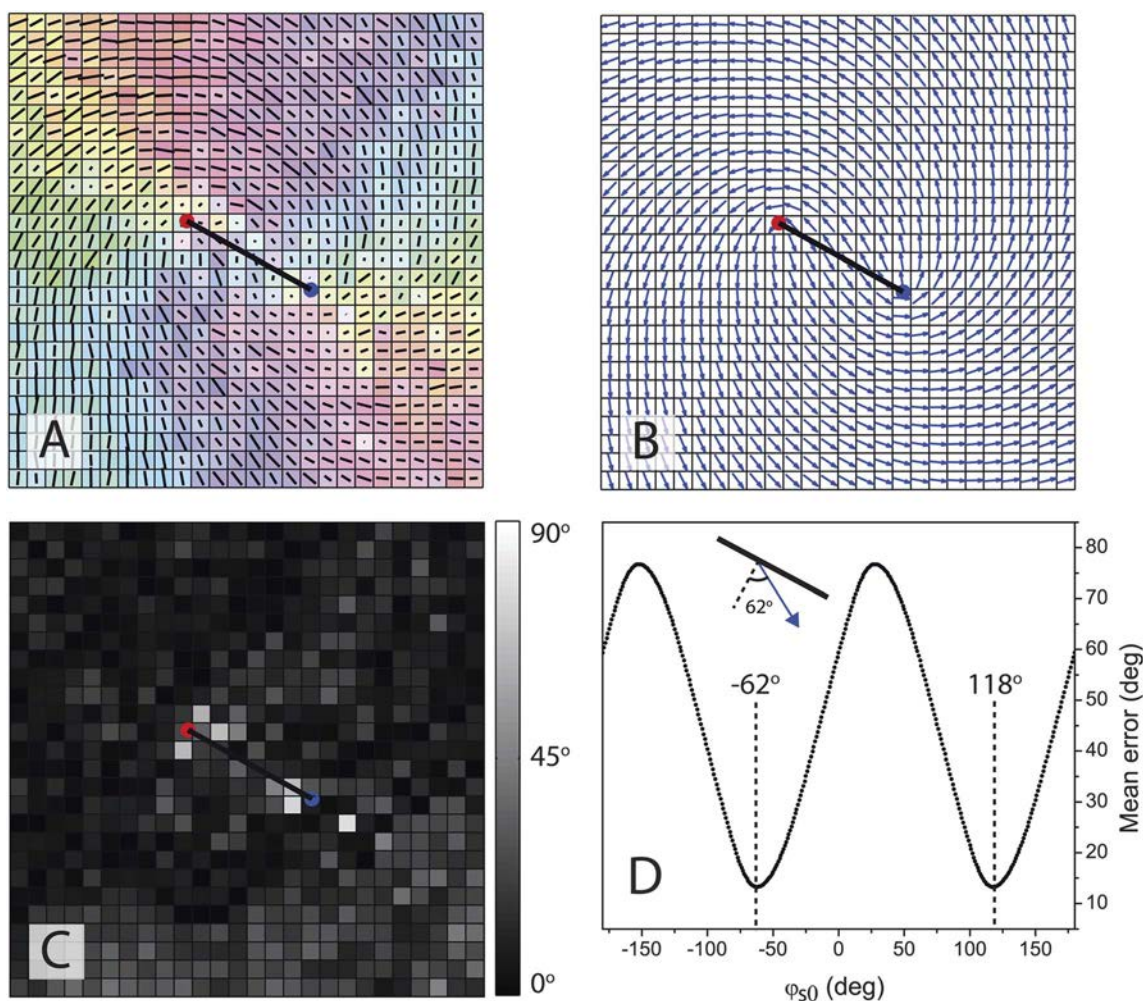


Fig. 7 Analysis of defect pairs. Image (A) shows the measured texture in the vicinity of a pair of $m = 1/2$ point disclinations in the center of a domain. The positions of the defects (red, blue points) were determined as in Fig. 6. A simulated texture pattern (B) that was fitted to the measurement in (A) using eqn (8). The simulation has two $m = 1/2$ defects at the experimentally measured positions and the offset φ_{s0} was fitted. There is an equivalent simulated texture with $\varphi_{s0} + 180^\circ$ (not shown). An error map (C) showing the difference between measured and simulated director angles. Plot of the average difference between measured and simulated texture (D) showing the two equivalent minima. Insert (D) shows how the detected value of φ_{s0} relates to the director orientation on the defect line in (B). (Image size (A–C) is $=1.6 \times 1.6 \mu\text{m}^2$).

Such behavior has in fact been seen in monolayer studies by Igenes-Mullol *et al.*³⁶(fig. 10). In bilayers this hypothesis should be subject to further study and verification.

In general, the domains should not be regarded as being in thermodynamic equilibrium although they are cooled slowly and are stable for at least 1 h. The question of equilibrium should always be associated with a characteristic time scale for the equilibrium state since remodeling of domains and their texture may occur over several regimes and be slowed by high energy barriers. True thermodynamic equilibrium in these systems may be difficult to obtain on realistic time scales.

In contrast to typical monolayer textures,³⁷ our membrane textures display a radial variation of the defects. The trend is that the center always has continuous texture which transforms to a segmented structure with defect lines emerging at some distance from the center. In general, when the bond angle field and the tilt orientation are coupled we have a so-called ‘locked texture’ which is continuously varying. Line defects represent a local

un-locking of these fields where the director orientation jumps to another minimum with respect to the bond angle field. Continuous textures are expected when the rigidity of the hexatic lattice (hexatic stiffness) is low and oppositely for high hexatic stiffness it is more energetically favorable to create line defects separating segments with uniform orientation. One possible reason for the mixed character of our domains is that they are grown thermally. This means that the decreasing temperature during growth is captured as a spatial variation from the center and towards to the domain boundary. If the hexatic stiffness as well as the other elastic constants of the free energy, are temperature dependent, then a radial variation in the preferred texture could arise. Assuming that the hexatic stiffness decreases with temperature,²⁷ we expect that the outer regions (lower temperature) of a domain should be segmented and the center (high temperature) should be continuous. This is indeed what is observed in our results. A similar issue was previously discussed by Igenes-Mullol *et al.*³⁶ who, contrary to expectations, found continuous textures at low

temperatures and segmented textures at higher temperatures in their DMPE monolayers.

The line defects in our bilayers are more complex than the defect lines in monolayers. In our system the lines are generally not straight, but may consist of linear segments. The bend/splay character vary between lines in the same domain. There is also a significant variation in the jump-angle of lines as demonstrated in Fig. 5. The radial variation in jump-angle for the same line defect may be attributed to the thermal growth conditions as discussed above. Variations in temperature could possibly influence the potential for coupling between the bond angle field and the lipid orientation and thus also the jump-angle.^{38,39}

The fact that the jump-angle deviates from 60° means that the I or F phases are not likely to exist in our domains. The I,F phases refer to the orientation of the director with respect to the bond angle field. When the director points to the nearest or next-nearest neighbors (I,F-phases) of the hexatic lattice, the jump-angle is $\pm 60^\circ$. But in some cases the system prefers an intermediate orientation between the nearest and next-nearest neighbor (L-phase) and jump-angles $< 60^\circ$ will occur. The observed large variability in jump-angles and their spatial variation in membranes points to a complex coupling between the bond angle field and the director with a possible similarity with the L-phase.

The width of the defect lines is probably below the optical resolution limit of our microscope. Gaining information about the width is relevant as it may allow an estimation of some of the elastic constants in the Landau free energy as proposed by Fischer *et al.*²² AFM imaging of defect lines in monolayer domains has shown that the lines are at least below ~ 100 nanometers.^{37,40,41} We have attempted to image bilayer textures with friction and tapping-phase AFM for higher resolution, but without obtaining adequate contrast. This difference from supported monolayers may be related to the fact that when scanning a membrane surface, the tip interacts with the hydrated lipid head groups which may block sensitivity to the acyl chain orientation underneath.

The observation of a pair of $|m| = 1/2$ point disclinations in the domain center is not made in monolayers under equilibrium conditions. The stability of an $|m| = 1/2$ disclination pair depends on the balance between the elastic repulsion between the point defects and the tension in the defect line connecting the two points. Under equilibrium conditions in monolayers, splitting of the central defect into pairs will not happen due to a dominating contribution from the line tension. But it has been shown by Hatta and Fischer that infrared laser heating of a polymerized monolayer can produce this splitting.^{42,43} The fact that we observe an $|m| = 1/2$ disclination pair in bilayer domains suggests that the relative contribution from line tension is weaker in bilayers. The weak alignment between the defect pairs as seen in Fig. 6B could possibly be ascribed to interactions with the crystalline mica substrate or to physical interactions between the domains following their nucleation.

From a fit of the simulated texture pattern to the measurement we have been able to determine the value of $|\varphi_{s,0}| = 60.5^\circ \pm 6.5^\circ$. With this value, the texture becomes a spiral that is intermediate between a pure bend or pure splay texture. All domains have essentially the same spiral pattern with a narrow spread in the values of $\varphi_{s,0}$. This indicates that $\varphi_{s,0}$ is conserved and that it is a characteristic property of the domains, possibly related to the

membrane lipid composition and/or the thermal history of the sample.

The phenomenon of half-integer disclinations connected by a defect line has historically been observed in XY-model simulations as well as in experiments on smectic liquid crystals. Swendsen⁴⁴ and Lee, Grinstein⁴⁵ both found patterns of strings connecting half-integer vortices in XY-type simulations. Subsequently Pang *et al.*⁴⁶ found intricate patterns of strings connecting fractionally charged vortices in tilted smectic-C liquid crystal thin films. Some of their patterns contained strings connecting $1/2$ vortices similar to ours, while others had different topological defects involving branched and circular string as well as vortex-antivortex pairs of zero net charge. An important difference between such liquid crystal and monolayer/bilayer textures is that liquid crystals are effectively infinite 2D systems with defects emerging spontaneously whereas in monolayers and bilayers the system is finite and texture may be regulated by boundary effects and the domain nucleation.

The nucleation of gel domains was previously investigated in detail.³² Among other things it was found that domains emerge by a combination of homogenous and heterogenous nucleation. From the present results we are not able to conclude with certainty that the nucleation point coincides with the central texture defect. But it is certainly possible that there is an intimate connection between the structure of the nucleation core and the central texture defect. Domains in both monolayers and membranes are always grown by starting with a minute nucleation core and these early events in the growth process may be much more important for governing the central defect pattern than equilibration with boundary conditions at the perimeter of a large domain. In a related system we have recently found that ripple domains in membranes can be templated by growing on a small gel domain.⁴⁷ More targeted studies are needed to clarify the importance of the nucleation event for texture formation in lipid bilayers.

Acknowledgements

We thank John Hjort Ipsen (MEMPHYS) for valuable discussions. The Danish National Research Foundation is gratefully acknowledged for support *via* a grant to MEMPHYS-Center for Biomembrane Physics. Experiments were carried out at DaMBIC (Danish Molecular Biomedical Imaging Center).

References

- 1 L. A. Bagatolli, J. H. Ipsen, A. C. Simonsen and O. G. Mouritsen, *Prog. Lipid Res.*, 2010, **49**, 378–389.
- 2 U. Bernchou, J. Brewer, H. S. Midtiby, J. H. Ipsen, L. A. Bagatolli and A. C. Simonsen, *J. Am. Chem. Soc.*, 2009, **131**, 14130.
- 3 J. Brock, R. Birgeneau, J. Litster and A. Aharony, *Contemp. Phys.*, 1989, **30**, 321–335.
- 4 W. de Jeu, B. Ostrovskii and A. Shalaginov, *Rev. Mod. Phys.*, 2003, **75**, 181–235.
- 5 C. Young, R. Pindak, N. Clark and R. Meyer, *Phys. Rev. Lett.*, 1978, **40**, 773–776.
- 6 R. Pindak, C. Young, R. Meyer and N. Clark, *Phys. Rev. Lett.*, 1980, **45**, 1193–1196.
- 7 S. Dierker, R. Pindak and R. Meyer, *Phys. Rev. Lett.*, 1986, **56**, 1819–1822.
- 8 D. Honig and D. Mobius, *J. Phys. Chem.*, 1991, **95**, 4590–4592.
- 9 S. Henon and J. Meunier, *Rev. Sci. Instrum.*, 1991, **62**, 936–939.
- 10 S. Henon and J. Meunier, *J. Chem. Phys.*, 1993, **98**, 9148–9154.

- 11 G. Weidemann, U. Gehlert and D. Vollhardt, *Langmuir*, 1995, **11**, 864–871.
- 12 G. Weidemann and D. Vollhardt, *Colloids Surf., A*, 1995, **100**, 187–202.
- 13 G. Weidemann and D. Vollhardt, *Thin Solid Films*, 1995, **264**, 94–103.
- 14 V. Moy, D. Keller, H. Gaub and H. McConnell, *J. Phys. Chem.*, 1986, **90**, 3198–3202.
- 15 X. Qiu, J. Ruiz-Garcia, K. Stine, C. Knobler and J. Selinger, *Phys. Rev. Lett.*, 1991, **67**, 703–706.
- 16 J. Ruiz-Garcia, X. Qiu, M. Tsao, G. Marshall, C. Knobler, G. Overbeck and D. Mobius, *J. Phys. Chem.*, 1993, **97**, 6955–6957.
- 17 D. Schwartz and C. Knobler, *J. Phys. Chem.*, 1993, **97**, 8849–8851.
- 18 B. Fischer, M. Tsao, J. Ruiz-Garcia, T. Fischer, D. Schwartz and C. Knobler, *Thin Solid Films*, 1996, **284–285**, 110–114.
- 19 V. M. Kaganer, H. Mohwald and P. Dutta, *Rev. Mod. Phys.*, 1999, **71**, 779–819.
- 20 C. Knobler and R. Desai, *Annu. Rev. Phys. Chem.*, 1992, **43**, 207–236.
- 21 J. Ignes-Mullol, J. Claret, R. Reigada and F. Sagues, *Phys. Rep.*, 2007, **448**, 163–179.
- 22 T. M. Fischer, R. F. Bruinsma and C. M. Knobler, *Phys. Rev. E: Stat. Phys., Plasmas, Fluids, Relat. Interdiscip. Top.*, 1994, **50**, 413–428.
- 23 K. Kjaer, J. Als-Nielsen, C. Helm, L. Laxhuber and H. Mohwald, *Phys. Rev. Lett.*, 1987, **58**, 2224–2227.
- 24 J. Kosterlitz and D. Thouless, *J. Phys. C: Solid State Phys.*, 1972, **5**, L124–L126.
- 25 J. Kosterlitz and D. Thouless, *J. Phys. C: Solid State Phys.*, 1973, **6**, 1181–1203.
- 26 B. Halperin and D. Nelson, *Phys. Rev. Lett.*, 1978, **41**, 121–124.
- 27 D. Nelson and B. Halperin, *Phys. Rev. B*, 1979, **19**, 2457–2484.
- 28 E. B. Watkins, C. E. Miller, D. J. Mulder, T. L. Kuhl and J. Majewski, *Phys. Rev. Lett.*, 2009, 102.
- 29 E. B. Watkins, C. E. Miller, J. Majewski and T. L. Kuhl, *Proc. Natl. Acad. Sci. U. S. A.*, 2011, **108**, 6975–6980.
- 30 R. Ziblat, L. Leiserowitz and L. Addadi, *Angew. Chem., Int. Ed.*, 2011, **50**, 3620–3629.
- 31 A. C. Simonsen, in *Handbook of Modern Biophysics: Biomembrane Frontiers. Nanostructures, Models and the Design of Life*, ed. R. Faller, T. Jue, M. L. Longo and S. H. Risbud, Humana Press/Springer, 2009, vol. 2, pp. 141–169.
- 32 U. Bernchou, J. H. Ipsen and A. C. Simonsen, *J. Phys. Chem. B*, 2009, **113**, 7170–7177.
- 33 J. Katsaras, D. Yang and R. Epand, *Biophys. J.*, 1992, **63**, 1170–1175.
- 34 M. L. Longo and C. D. Blanchette, *Biochim. Biophys. Acta, Biomembr.*, 2010, **1798**, 1357–1367.
- 35 C. D. Blanchette, C. A. Orme, T. V. Ratto and M. L. Longo, *Langmuir*, 2008, **24**, 1219–1224.
- 36 J. Ignes-Mullol, J. Claret and F. Sagues, *J. Phys. Chem. B*, 2004, **108**, 612–619.
- 37 J. Sanchez and A. Badia, *Chem. Phys. Lipids*, 2008, **152**, 24–37.
- 38 J. Selinger and D. Nelson, *Phys. Rev. Lett.*, 1988, **61**, 416–419.
- 39 J. Selinger and D. Nelson, *Phys. Rev. A: At., Mol., Opt. Phys.*, 1989, **39**, 3135–3147.
- 40 K. Meine, D. Vollhardt and G. Weidemann, *Langmuir*, 1998, **14**, 1815–1821.
- 41 D. Gourdon, N. A. Burnham, A. Kulik, E. Dupas, F. Oulevey, G. Gremaud, D. Stamou, M. Liley, Z. Dienes, H. Vogel and C. Duschl, *Tribol. Lett.*, 1997, **3**, 317–324.
- 42 E. Hatta and T. Fischer, *J. Phys. Chem. B*, 2003, **107**, 6406–6410.
- 43 E. Hatta and T. Fischer, *J. Phys. Chem. B*, 2005, **109**, 2801–2804.
- 44 R. Swendsen, *Phys. Rev. Lett.*, 1982, **49**, 1302–1305.
- 45 D. Lee and G. Grinstein, *Phys. Rev. Lett.*, 1985, **55**, 541–544.
- 46 J. Pang, C. Muzny and N. Clark, *Phys. Rev. Lett.*, 1992, **69**, 2783–2786.
- 47 U. Bernchou, H. Midtiby, J. H. Ipsen and A. C. Simonsen, *Biochim. Biophys. Acta, Biomembr.*, 2011, **1808**, 2849–2858.

Appendix 2

Manuscripts in preparation

Variations in the Hydrophobic Mismatch affects the Orientational Texture in Phospholipid Bilayers

Jes Dreier, and Adam Cohen Simonsen

Variations in the Hydrophobic Mismatch affects the Orientational Texture in Phospholipid Bilayers

Jes Dreier, and Adam Cohen Simonsen

(Dated: October 30, 2012)

Abstract

In this letter we describe phosphocholine lipid bilayers with coexisting L_α and $L_{\beta'}$ phase. By changing the lipids in the mixture the hydrophobic mismatch is affected, which impacts both the shape and the orientational texture, measured using polarized two-photon microscopy, of the $L_{\beta'}$ domains. These changes can be traced back to a coupling between the line tension and the orientation of the lipids at the domain boundary. Furthermore the forces and mechanism that control domain nucleation is present in the large macroscopic domains, and thus available to measure using fluorescence microscopy.

The cell membranes primary function is to separate the interior and exterior of both the whole cell and its compartment, however that it is not its sole purpose.[1] The first membrane model were the "fluid-mosaic" model proposed by Singer and Nicolson in 1972[2], in which the lipid bilayer is merely a two dimensional solvent. Since then several new model have been described, all of which bestow a larger role to the lipids. However it is highly debated which model best fits current results, which have made the study of lateral organisation of the cell membrane an important and rapid expanding scientific topic.

A basic understanding of the forces and mechanisms that drive and control the ordering and phases behavior of a simple binary model membrane will prove instrumental in the task of understanding the biological membrane. In order to achieve this, a better understanding of the thermodynamics for lipid bilayers are needed. Lipids bilayers can, even in quite simple model system, exhibit numerous different phases. The most important phases are, here using the nomenclature used for lamellar phases[3]: 1. The L_α phase, characterized by a high disorder in the tails and high mobility of the lipids, also referred to as liquid-disordered (L_D) or fluid phase. 2. L_β (or $L_{\beta'}$ for tilted lipids), characterized by a slower diffusion ($D \simeq 10^{-10}cm^2s^{-1}$)(ref?) and an ordering of the tail, also referred to as the gel phase or solid-ordered. 3. The liquid-ordered phase, only present in sterol containing bilayers, is characterized by ordered tails but high mobility of the lipids.[1] Besides from the three mentioned several more exist, e.g. a crystalline subgel phase, the ripple phase[4] etc. and several new phases have been suggested through the last few years, e.g. the textured lipid phase[5], the raft phase[6] etc.

What have intrigued us is the resemblance between the $L_{\beta'}$ phase and liquid crystals. The use of liquid crystal theory to describe monolayer system has been done for the last few decades,[7, 8] i.e. Fisher et al. developed a theory explaining the textures observed in monolayer system by expanding the theory for liquid crystal films. However only theoretical work has been done for lipid bilayer systems. Recently we have showed that the orientational texture in lipid bilayer $L_{\beta'}$ domains could be measured by using polarized 2-photon fluorescence microscopy.[9, 10] Several different features and defect structures were observed,e.g. divided into subdomains, points and line defects etc., revealing a complexity that previously had been overlooked. The orientational order showed many resemblance to the hexatic phase

know from liquid crystals, which is well reported in lipid monolayers.[11] It is characterized as a phase between the liquid and solid phase possible for some two dimensional system, it has a short-range positional order, and a long-range bond-orientational order.[12] Kuhl et al. have recently demonstrated that grazing incidence x-ray diffraction (GIXD) measurements on supported bilayers, made by the Langmuir-Blodgett-Schaeffer technique, showed a short range positional order, that suggest an orientational order.[13, 14] In a seperated studie they showed the binding of cholera toxins B subunit induced a very complex oritentaion texture, that allowed effects of the binding of the protein to transfer to the opposite leaflet of the membrane. [5]

In this letter we use bi-component supported lipid bilayers in the phase co-existing region to produce $L_{\beta'}$ domains, which we image using polarized 2-photon fluorescence microscopy to investigate the orientational texture. By changing the tail length of the lipids we are able to manipulate the hydrophobic mismatch, while keeping other parameters and forces constant. The hydrophobic mismatch have been reported to affect many aspect of phase separation and formation, like line tension[15], domain nucleation[16] domain size, and demixing temperature[17]. In here we report how it affects the formation and the orientational texture of the domains. We have used those observation to gain insight into what control and induces the orientational texture of the $L_{\beta'}$ phase.

We fabricate bi-component supported lipid bilayers by spin coating using Muscovite mica as support.[18, 19] The lipids used in this work were: 1,2-dimyristoyl-sn-glycero-3-phosphocoline (DMPC), 1,2-dipalmitoyl-sn-glycero-3-phosphocholine (DPPC)for the lipids with high melting temperature lipids and 1,2-dioleoyl-sn-glycero-3-phosphocholine (DOPC), 1-palmitoyl-2-oleoyl-sn-glycero-3-phosphocholine (POPC) for the low melting temperature lipids. The samples were heated in HEPES buffer at ph 7 above the transition temperature, followed by a cooling at a controlled rate into the phase coexisting region, $0.8^{\circ}Cmin^{-1}$ for the DOPC,DPPC and POPC,DMPC mixture and $0.1^{\circ}Cmin^{-1}$ for DOPC,DMPC and POPC,DMPC mixtures. The samples were investigated in a custom build polarized two-photon fluorescence microscope, and by using Laurdan (0,5 molar%) as the fluorescence probe, we are able to measure the lipid tail orientation, which is described in detail in our previous work. [9, 10]. The orientation recorded are converted into a color using the scheme in Fig. 2A insert.

We used an AFM (jpk nanowizard, Germany) to measure the height difference between

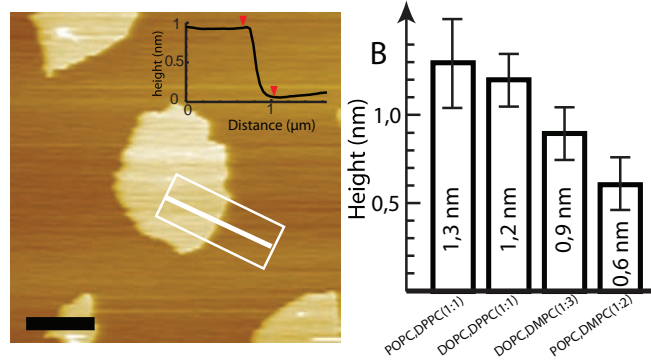


FIG. 1. AFM image of the DOPC,DMPC mixture (A). To measure an accurate height an average of the lines within the white box were taken and plotted as a graph (insert), from which the height were measured as the difference between the red markers. Several images and domains were recorded for each sample and the result is shown in B. The error bars represent the noise level of our AFM under these experimental conditions. The scale bar is $1 \mu m$

the two phases, $L_{\beta'}$ and L_{α} , and thereby the hydrophobic mismatch region, as illustrated with a 'h' in Fig. 2F. AFM images were recorded using contact mode in water of samples with both phases present. The results are shown Fig. 1. The samples were imaged with an identical and small force to ensure the measured height difference corresponded to one leaflet. The method for measuring the height difference is illustrated in Fig. 1A, the lines within the white box is average to give the line scan (insert), the hydrophobic mismatch is then measured as the height between the two markers on the line scan. This procedure were done for several domains, and the result is presented in Fig. 1B. The error bars represent either the noise level of the AFM ($\pm 0.15 \text{ nm}$) or the standard deviation of the measurements, which ever is greatest. A comparison to the literature gives values of $1.1 \pm 0.2 \text{ nm}$ for the DOPC,DPPC mixture[20] and 1.2-1.5 nm for the POPC,DPPC mixture[18], both values match the results presented here. As expected the DMPC domains have a smaller hydrophobic mismatch than the DPPC domains, due to the shorter fatty acid chain. The exchange of DOPC to POPC further decreases the hydrophobic mismatch for the DMPC, whereas the effect on the DPPC is below our resolution limits.

The texture of the 4 different compositions can be seen in Fig. 2, namely DOPC,DPPC 1:1 molar ratio (A), POPC,DPPC 1:1 (B), DOPC,DMPC 1:3 (C), and POPC,DMPC 1:2(D). The color (A,insert) and the lines represent the orientation of the lipid acyl chain. For the

DOPC,DPPC domains, as seen in figure 2A we see a clear pattern of the texture. In the center of the domain where it original nucleated, there is a continuous changes of angle. Further away from the center the domain is split into 6 subdomains within each there is a preferred orientation of the lipids. Neighboring subdomains are confined from each other by defect lines. All those observations are described in details in our previous paper. [9] The texture exhibited by the POPC,DPPC mixtures is virtually indistinguishable from the DOPC,DPPC mixture. However some of the mixtures show an remarkably different texture. For the DOPC,DMPC mixture we see a few domains with a uniform texture (ex. the big green domain), however most of the domains have a large uniform part, and smaller subparts with different orientation. The POPC,DMPC mixture shows an overall uniform texture with no change of orientation across the domain. Several domains are observed in the image, each with a different uniform orientation, thus indicating that the texture direction is not highly influenced by the mica substrate. The domains shape of the two DMPC containing mixtures are roughly circular, which are in contrast to the flower-shaped domains observed for the DPPC containing mixtures.

The domain growth in a bi-component bilayer does not happen isothermally. As the sample is cooled from the fluid region of the phase diagram and into the phase co-existing region, the domains will nucleate at the phase boundary. As the sample is further cooled the domains will grow in size, but the number of domains remain constant.[19] This is illustrated in Fig. 2E where two points are marked for the DOPC,DPPC 1:1 mixture in the phase diagram. At point a, which is just below the nucleation temperature, the molar fraction in $L_{\beta'}$ phase is 0.08 while at point b, which is at a lower temperature has a molar fraction of 0.26 in the $L_{\beta'}$ phase. We use a constant cooling rate through the nucleation temperature to grow the domains instead of a under-cooling of the sample.[22]. We have found that under cooling is not possible using our current setup.

Since the domains are grown during a change of temperature the physical parameters, e.g. line tension etc., can change during domain growth. In Fig. 3 the texture have been measured for two domains during the growth, with a mixture of DOPC,DPPC Fig. 3A-C and POPC,DMPC Fig. 3D-F, respectively. The image with the highest temperature for each series(A+D) have been taken as close to the nucleation as possible. The images within each series are taken of the same area. The texture observed in the initial domains, Fig. 3A+D, remains unchanged during the further cooling and growth of the domain. Lipids that

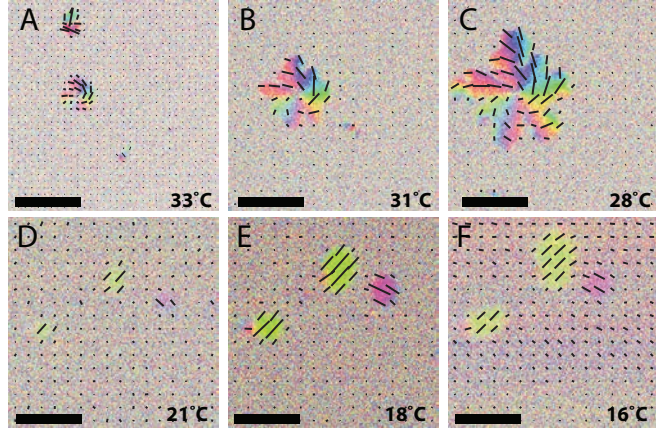


FIG. 3. Image of the texture recorded during domain growth, across a temperature gradient. A-C, DOPC,DPPC 1:1. D-F, POPC,DMPC 1:2. The images, for each mixture, are of the same area. All scale bars are $5 \mu m$

the texture and the domain, which could potentially lead to a change in the orientational texture during the growth. A closer look at the DOPC,DPPC growth experiment, Fig. 3A-C, reveals that the part of the domain that is formed in (A) remains the same in the later image (B+C). This means that either the energy of the texture is not changed significantly or the relaxation of the texture happens on a time scale not accessible in this experiment. Relaxation of the domains after the growth periods for several hours show no effect on the shape or texture of the domain. Longo et al. recently described how branched cerebroside domains were reshaped to more compact domains over a period of several hours through edge diffusion.[22, 23]

We will now discuss the possible origin of the textures observed. The three major difference between the samples are: 1. the cooling rate of the sample, 2. The temperature of nucleation, 3. The lipid acyl chain length, which affect the hydrophobic mismatch. The cooling rate only has an effect if the texture would reorganise during the domain formation, but one the timescales used in this letter it is not observed. The intrinsic tilt of the lipids, DPPC and DMPC, are very similarly, and about 30° [14, 24, 25] when measured with GIXD or x-ray diffraction/scattering. However Sun et al. showed that for PC-lipids the greater the chain length the greater the tilt, meaning that the DPPC is more tilted than the DMPC.[26] But the difference is small and probably without significance in the further discussion. This leaves us with the hydrophobic mismatch and the nucleation temperature.

We will therefore discuss the energy of the domains. The equilibrium texture for a domain can be split into the energy of the bulk of the domain, and the energy of the border of the domain.[7]. According to Fisher et al. the minimum energy for the bulk of the domain is uniform texture since it does not involve any defects or bend/splay in the hexatic grid. They further prove that for a monolayer the uniform texture is only allowed for domains larger than a certain size, which is related to the magnitude of the energy gain by having a certain orientation of the lipids regarding the normal to the boundary, the energy cost of deforming the hexatic grid and the energy cost of the point defect in the center. In short; for monolayers the uniform texture is favored by large domain.[7]. However monolayer systems rarely/never show uniform texture, indicating that the energy gained by ordering the tails in the circumference towards the border of the domain, is higher than the energy cost of creating defect lines and/or point defects. Thus the domain texture in monolayers are govern by boundary conditions. A closer look at the DOPC,DPPC or POPC,DPPC mixture, as seen in Fig. 2, reveals no preferred angle between the orientation and the normal to the boundary. Which indicates that the texture, at least in the large domain, is not controlled by the boundary conditions.

An investigation of the center of the DPPC containing domains, around the nucleation center, show good agreement with a continuously changes of angle.[9] This leads to the hypothesis that the texture at the nucleation site act as a template for the texture of the remaining domain, as was seen during the growth in Fig. 3A-C. As new lipids condensate onto the formed domain the orientation will be govern by the existing texture. A round domain with the vortex-like texture exhibited by DOPC,DPPC would have a preferred orientation towards the boundary, meaning the texture is coupled to the boundary during the early domain growth.

There is a striking difference between the shape of the DPPC containing domains and the two mixtures containing DMPC. Three different mechanisms can be thought of that govern the shape of the domains: 1. line tension, minimizing the perimeter to area ratio (round domain), 2. The texture (roundish hexagonal or six-leafed flowers[7]) or 3. A fractal growth (snow flake/icecrystal). Therefore it seems that the DMPC domains are govern by line tension, whereas the DPPC domains are a mixture of more than one phenomena. The line tension is highly dependent on the hydrophobic mismatch[15, 17], as measured in Fig 1. Where a high hydrophobic mismatch would result in a high line tension, however the

trend we observe regarding the shape, shows the opposite effect. The samples with high hydrophobic mismatch have flower like shapes, whereas the samples with a low hydrophobic mismatch have round domains. Therefore the line tension is not solely depended on the hydrophobic mismatch. One way to solve this problem is to include the orientations of the lipids at the boundary to the line tension.

To investigate this we examine the energy of the domains shortly after nucleation, where the domain shapes are round. It is indisputable, that there is an energy cost associated with the point defect in the center of the DOPC, DPPC domains. Therefore the system need regain some energy from the non-uniform texture, otherwise the texture would be uniform. This could be done by ordering the texture towards the boundary, thus effectively reducing the line tension.[7] However the energy of the interface still need to positive, which affect the amount of energy that can be gain at the interface. This means the isotropic line tension, which does not include the orientation and is controlled by the hydrophobic mismatch, sets a threshold for the energy that can be gain by ordering the tail. For the POPC, DMPC domains the isotropic line tension is smaller, due to a low hydrophobic mismatch, therefore the amount of energy gain by ordering the texture at the boundary is smaller, and insufficient to pay for the point defect in the center. Whereas the opposite is the case for the DPPC domains. This theory matches well with the observations for the texture of the domains and can also explain the differences in the shapes, since DPPC domains have a reduced line tension due to the ordering of the lipids at the interface. Resulting in a lower line tension than the DMPC domains. How this persist in the final large DPPC domains, where the ordering of the orientation at the interface is lost, is at the moment not clear.

The observations and discussion presented in this letter have increased the knowledge of the complex behavior of domain and texture formation in a lipid bilayer. An important lesson to get from these studies is that the effect that govern the nucleation of the domains, is persistent in the much larger domains at a later time point and lower temperature. This effectively means the large macroscopic domains are a window into the parameter and behavior that govern nanoscopic domains as well. This effectively proves the essentiality of studies of model membrane system with respect to understanding domain formation, inhomogeneity, and phase separation in biological membranes and living cells.

-
- [1] O. G. Mouritsen, *Life - As a matter of fat*, 1st ed. (Springer, 2005).
- [2] S. SJ and N. GL, *Science* **175**, 720 (1972).
- [3] M. Koynoca and Y. Caffrey, *Biochim. biophys. Acta* **1376**, 91 (1998).
- [4] U. Bernchou, H. Midtiby, J. H. Ipsen, and A. C. Simonsen, *Biochim. biophys. Acta Biomembr.* **1808**, 2849 (2011).
- [5] E. B. Watkins, C. E. Miller, J. Majewski, and T. L. Kuhl, *Proc. Natl. Acad. Sci. USA* **108**, 6975 (2011).
- [6] I. Levental, M. Grzybek, and K. Simons, *Proc. Natl. Acad. Sci. USA* **108**, 11411 (2011).
- [7] T. M. Fischer, R. F. Bruinsma, and C. M. Knobler, *Phys. rev. E* **50**, 413 (1994).
- [8] W. de Jeu, B. Ostrovskii, and A. Shalaginov, *Rev. Mod. Phys.* **75**, 181 (2003).
- [9] J. Dreier, J. Brewer, and A. C. Simonsen, *Soft Matter* **8**, 4894 (2012).
- [10] U. Bernchou, J. Brewer, H. S. Midtiby, J. H. Ipsen, L. A. Bagatolli, and A. C. Simonsen, *J. Am. Chem. Soc.* **131**, 14130+ (2009).
- [11] R. Kenn, K. Kjaer, and H. Mohwald, *Coll. Surf. A* **117**, 171 (1996).
- [12] S. Chandrasekhar, *Liquid Crystals*, 2nd ed. (Cambridge University Press, 1992).
- [13] C. E. Miller, J. Majewski, E. B. Watkins, D. J. Mulder, T. Gog, and T. L. Kuhl, *Phys. Rev. Lett.* **100** (2008).
- [14] E. B. Watkins, C. E. Miller, D. J. Mulder, T. L. Kuhl, and J. Majewski, *Phys. Rev. Lett.* **102** (2009).
- [15] P. Kuzmin, S. Akimov, Y. Chizmadzhev, J. Zimmerberg, and F. Cohen, *Biophys. J.* **88**, 1120 (2005).
- [16] C. Blanchette, W. Lin, O. CA, R. TV, and L. ML, *Langmuir* **23**, 5875 (2007).
- [17] A. J. Garcia-Saez, S. Chiantia, and P. Schwille, *J. Bio. Chem.* **282** (2007).
- [18] A. C. Simonsen and L. A. Bagatolli, *Langmuir* **20**, 9720 (2004).
- [19] U. Bernchou, J. H. Ipsen, and A. C. Simonsen, *J. Phys. Chem. B* **113**, 7170 (2009).

- [20] A. Burns, *Langmuir* **19**, 8358 (2003).
- [21] K. Furuya and T. Mitsui, *J. Phys. Soc. Jpn.* **46**, 611 (1979).
- [22] C. D. Blanchette, C. A. Orme, T. V. Ratto, and M. L. Longo, *Langmuir* **24**, 1219 (2008).
- [23] M. L. Longo and C. D. Blanchette, *Biochim. Biophys. Acta Biomembr.* **1798**, 1357 (2010).
- [24] S. Tristram-Nagle, Y. Liu, J. Legleiter, and J. Nagle, *Biophys. J.* **83**, 3324 (2002).
- [25] J. Katsaras, D. Yang, and R. Epand, *Biophys. J.* **63**, 1170 (1992).
- [26] W. Sun, S. Tristram-Nagle, R. Suter, and J. Nagle, *Biophys. J.* **71**, 885 (1996).